QATAR UNIVERSITY

COLLEGE OF ENGINEERING

IMPACT OF FINES ON GAS RELATIVE PERMEABILITY THROUGH SAND USING PORE NETWORKS FROM 3D SYNCHROTRON MICRO-COMPUTED TOMOGRAPHY

BY

JAMAL ADEL IBRAHIM HANNUN

A Thesis Submitted to

the Faculty of the College of Engineering

in Partial Fulfillment of the Requirements for the Degree of

Masters of Science in Civil Engineering

June 2019

COMMITTEE PAGE

The members of the Committee approve the Thesis of
JAMAL ADEL IBRAHIM HANNUN defended on 21/04/2019.

Dr. Riyadh Al-Raoush
Thesis/Dissertation Supervisor

Prof. Fadhil N. Sadooni
Committee Member

Dr. Thomas Seers
Committee Member

Approved:

Abdel Magid Hamouda , Dean, College of Engineering

ABSTRACT

HANNUN, JAMAL, A., Masters : June : [2019], Masters of Science in Civil Engineering

Title: Impact of Fines on Gas Relative Permeability through Sand using Pore Networks from 3D Synchrotron Micro-Computed Tomography

Supervisor ofThesis: Dr. Riyadh, I, Al-Raoush.

Fines migration and transport in sand systems have huge influence on vital applications, including the storage and recovery of water and energy resources from the subsurface. Multi-phase flow of gas through saturated unconsolidated media takes place between the pores of sediments, physical phenomenon at the pore-scale control the flow properties. Given a sandy sediment media, gas permeability is highly affected by fine particles due to migration, clogging and bridging reducing gas flow or causing sand particles to displace creating fractures. There is a knowledge gap of fines effects on gas production from sandy sediments, especially at the pore-scale. Therefore, there is a need to model and quantify effects of fines in multi-phase flow using pore networks to better understand gas recovery systems.

Three-dimensional, synchrotron micro-computed tomography images of sand sediments were obtained at Argonne National Laboratory at a resolution of 3.89 micron per voxel. Kaolinite and Montmorillonite fine particles were added in varied concentrations in six soil specimens, each system was scanned at four stages with varied saturations of brine and CO_2, resulting in 20 systems. Micro-computed tomography images were processed for 3D visualization, quantification and pore network modeling. Pore Network Models were generated, and relative permeability properties were then

computed for each system.

Findings revealed that fines accumulate at sand-brine and brine-gas interfaces. As fines concentration increased, gas percolation decreased. Further increase in fines concentrations resulted in blocking local gas flow causing pressure variations enough to create fractures that allows gas to escape and permeability to increase back. Pore Networks and Computer-Based Two-Phase Flow Simulations can effectively be used to characterize flow in porous media. In unconsolidated media the pore space geometry will change due to sand grains movements. At high concentrations, different fines type produces altered gas flow regimes, Kaolinite resulted in fractures while montmorillonite resulted in detached gas ganglia. Generally, increasing fines reduces gas percolation and further injection of gas reduced permeability. The finds herein are critical in understanding the impact of fines migration during gas flow in sand, they can be applied to characterizing and predicting two phase properties of unconsolidated sediments.

DEDICATION

To my family, it is because of them this work saw the light. To all researchers in this vital field.

ACKNOWLEDGMENTS

Thanks to Allah whom by his blessings good deeds are achieved. Many thanks to my supervisor, inspirer and best model Dr.Riyadh Al-Raoush for offering me his precious time, knowledge and full support during my masters studies, thanks to him I was able to achieve in such an advance and noble field. I am grateful for all my research colleagues in Dr.Riyadh group in Qatar University and beyond, many thanks to Eng.Zaher Jarrar for his help in many ways in my thesis work.

Huge gratitude to my Civil Engineering Department at Qatar University for their great collaboration and support, I like also to acknowledge the support of Qatar National Research Fund (QNRF) National Priorities Research Projects (NPRP) for providing great platform for national human capital at Qatar and investing in young talents. Also, I would like to express my gratitude to the Advance Photon Source (APS) at Argonne National Laboratory (ANL), precisely to Dr.Marks Rivers and his group for helping us in obtaining state of the art 3D images for this work.

Many thanks to Prof. Fadhil Sadooni and Dr. Thomas Seers for the outstanding effort and the remarkable notes, their expertise helped me in crafting my thesis.

This research was made possible by the National Priorities Research Program (NPRP) grant # NPRP8-594-2-244 from Qatar National Research Fund (a member of Qatar Foundation). The findings achieved herein are solely the responsibility of the authors.

TABLE OF CONTENTS

LIST OF TABLES

LIST OF FIGURES

CHAPTER 1. INTRODUCTION

1.1. Overview of Unconsolidated Porous Media

Unconsolidated porous media is any sediment in which the solids are packed loosely. Sand and sandstones are considered as porous media that is unconsolidated with high porosity and permeability, thus it has the ability to store fluids and pass them efficiently. Unconsolidated sand is considered a good reservoir sediment, such reservoirs are common, and usually have a great potential in storing and passing vital substances including water, oil and gas. It is important for civilized societies to be able to recover such reserves from water aquifers or oil and gas reservoirs, it is also critical to understand the flow phenomenon of these valuable materials as they percolate through deep earth beds. In unconsolidated pores media including sand, the fluids whether gases or liquids, flow between the solids in the void space (pore space) as seen in figure 1.1.1 (Yu and Cheng, 2002), the connectivity of the pore space is of a huge significance to the permeability of the sediment, also the geometry of the pore (the small voids) and their throats (the connecting bodies of pores) is a major point of control on the flow properties of sediments. Many approaches were developed to uncover the geometry of different unconsolidated porous media, the best of which is Micro-Computed Tomography. This technology uncovers the details of the 3D space of soil at the microscopic scale.

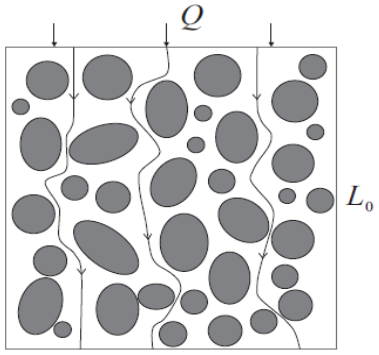

Figure 1.1.1: flow in porous media between the sand grains (Yu and Cheng, 2002)

1.2. Overview of Fine Migration and Two-Phase Flow

Fines are small grains that are originated from the porous media in the subsurface or that are carried by fluids passing it. As they migrate, smaller fines flow through the pore's throats, while bigger ones get entrapped between the sediments grains. This blockage alters the flow patterns of a specific media. It is of a special importance to predict such change in flow regimes. With the recent advances in science more work is carried on in this field with the aim of characterizing the fines effects on multi-phase flow of liquids and gases in unconsolidated porous media, especially sand.

The geometry of voids in an unconsolidated pores media is considered the most complex issue when compared to other sediments. These complex geometries can be revealed from 3D X-Ray images. In order to characterize flow patterns and predict them, a number of spatial properties must be calculated. It is inefficient to carry such studies on complex geometrics, therefore it was shown that simplifying the pore space to simpler spheres and cylinders can result in accurate prediction of flow regimes in unconsolidated porous media.

Two-phase flow experiments are conducted by displacing a fluid that is occupying the void space with another fluid that is being injected. As the fluids flow in and out of the sediment system, the relative permeability of each fluid is measured. Additionally when simulating such experiments using a pore network generated from a 3D image, the two-phase flow simulation are proven to show similar results for the relative permeability and the capillary pressures of pores. This helps in studying and predicting the flow in unconsolidated porous media, which will improve the capabilities in predicting the flow properties of sediments. Figure 1.2 shows how that geometrical parameters can affect entrapment and flow of fluids in the void space (Lake, 1989).

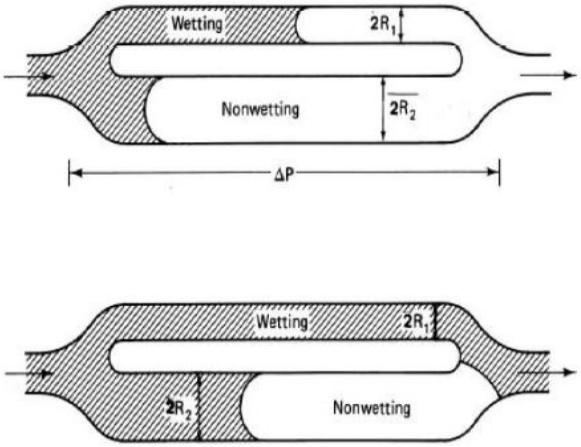

Figure 1.2.1: two-phase flow altering wettability by pore geometry (Lake, 1989)

1.3. Thesis Organization

This thesis is organized as follows: raw data for fines impact on two-phase flow was acquired using a synchrotron facility, the images were filtered then segmented, and next pore networks were generated from the post-processed images. Computer simulations of two-phase flow experiments were conducted using the generated pore networks, the result and the most important conclusions were summarized at the end.

1.4. Objectives

- Obtain 3D images to visualize the impact of fines on gas flow in 3D.
- Visually identify the effect of different fines on the movement of sand as the CO_2 gas is injected with time.
- Quantifying the fines and gas flow induced change on pore space.
- Characterizing the change in permeability due to fines and gas injection during sand movement.

CHAPTER 2. BACKGROUND AND LITERATURE REVIEW

2.1. Background

Migration of fine particles in a fluid is affecting wide range of activities. As fluids move through porous media in the subsurface they tend to carry or mobilize solid particles due to fluid drag. These particles can be derived in the subsurface from rock formations (Gruesbeck & Collins, 1982) or they can be transported from a source. Fine particles can be introduced to the porous media naturally or synthetically; they can be natural clays, quartz, minerals or contaminants as illustrated in Figure 2.1.1 (a) by (Muecke, 1979), in (b) montmorillonite and kaolinite are showed to be present in significant portions. ISO 14688-1:2002 classified fine particles as clays and silts with dimensions less than 2 μm and 63 μm respectively. (Hasan et al., 2017) defined the process of size exclusion as when fines bigger than the pore space are transported in the pores media and get entrapped, (Sakthivadivel, 1966) proposed that this process results in deposits that are responsible on plugging the pore throats (openings that connects the pore space), which reduces the ability of the passage in the subsurface pore space, this ultimately reduces permeability of the sediment.

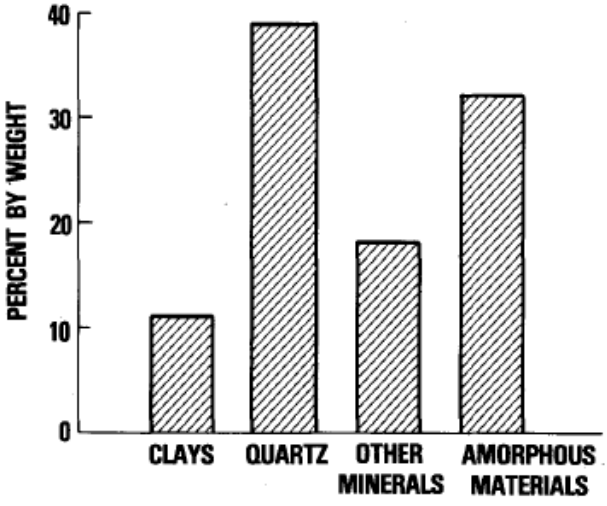

(a)

	Well A	Well B	Well C	Well D
Clays				
Montmorillonite	5.5	13.4	2.2	1.4
Illite	6.2	9.1	3.0	1.7
Kaolinite	0.8	4.2	1.3	0.7
Chlorite	3.9	—	—	—
Quartz	36.7	24.0	47.3	17.0
Other Minerals				
Feldspar	8.6	5.7	9.1	5.4
Muscovite	1.6	—	1.6	1.0
Sodium chloride	1.1	1.3	7.8	5.0
Calcite	—	1.6	—	—
Dolomite	—	—	1.8	2.8
Barite	—	—	—	22.1
Amorphous Materials	35.6	40.7	25.9	42.9
Total	100.0	100.0	100.0	100.0

*Passed 400 mesh screen.

(b)

Figure 2.1.1: proportion of fines from real subsurface samples (Muecke, 1979).

For example, in the petroleum industry, transport of fines in natural rocks is considered as one of the main challenges of production. As fluids are extracted or injected, fines from rock formations are migrated inducing bridging and blocking of the passages in the pore space, this may cause formation damage. The formation damage can reduce the productivity and is responsible of loses of $140 billion/year according to (Byrne, 2012). The reduction of porous media permeability and porosity due to solids invading the pores of sediments are considered from the main issue in production as outlined by (Bennion & Thomas, 1994; Bennion et al., 1999). These phenomenon are dependent on colloids physics at the pore scale, a micromodels study by (Jung et al., 2018a) concluded in Figure 2.1.2, to represent the previous studies of (Khilar & Fogler, 1987; Bigno te al., 1994; Khilar& Fogler, 1998; Oyeneyin et al., 1995); the fine migrations, bridging and clogging are linked to two important geometrical parameters; size of grain(host) to fine particle (D/d) and throat to fine particle size(o/d).

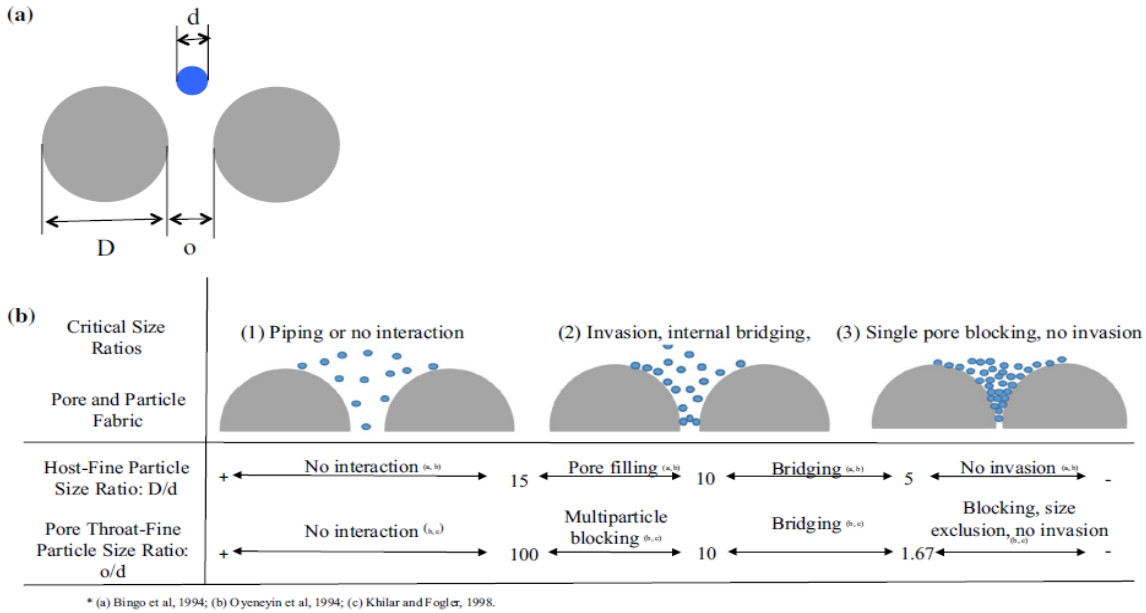

Figure 2.1.2: critical size of gains, throats and fines (Jung et al., 2018a)

These conclusions were reached through utilizing micro-models inspected using microscopes. That was a great leap in characterizing such phenomenon. However there is an increasing need to understand fines influence beyond two dimensions. Those three-dimensional studies are in need to represent the real void space of sediments. Micro-computed tomography (μCT) is an effective tool to inspect sediments samples at microscopic level in 3D.

Previously, access to advanced μCT for sediments study applications was limited, nowadays there is an ongoing improvement in technology that allow such studies. Utilizing high brilliance X-Ray sources is considered as the most advance approach in studying sediments samples, as they are capable of penetrating thick sample and uncovering the spatial details in a level exponentially better than other X-Ray sources such as X-Ray tubes, lasers and cyclotrons. Table 2.1.1 shows a selection of Synchrotron facilities that provide access to high brilliance X-Ray which is used to reconstruct the samples volume at microscopic level, an advantage over Scanning electron microscope which cannot penetrate the sample.

Table 2.1.1: A Selection of Synchrotron Facilities Around The World, APS was used for The Experiments in this Work

Facility name	Location	Country	Energy (GeV)	Circumference (m)	Commissioned for synchrotron radiation studies
SPring-8	RIKEN	Japan	8	1,436	1997
Advanced Photon Source (APS)	Argonne National Laboratory	US	7.0	1,104	1995
PETRA III	DESY	Germany	6.0	2,304	2009
European Synchrotron Radiation Facility(ESRF)	Grenoble	France	6	844	1992
Shanghai Synchrotron Radiation Facility(SSRF)	Shanghai	China	3.5	432	2007
Australian Synchrotron	Melbourne	Australia	3	216	2006
Diamond Light Source	Oxfordshire	UK	3	561.6	2006
Synchrotron-Light for Experimental Science and Applications in the Middle East (SESAME)	Al Balqa	Jordan	2.5	133	2016

2.2. **Studies in the Literature**

Two-phase fluid flow takes place in the voids between the sand grains. These spaces are usually in the microscopic scale and flow is affected by properties of fluids such as the viscosity and interfacial tension. Another factor that impact the flow in sand sediment is the presence of fine particles that can clog or bridge throats, thus blocking the flow. In order to understand and simulate such complex multi-phase flow behaviors, researchers developed different approaches each with strengths and compromises. Among these is pore networks approach which have the advantage of lower computational cost compared to other methods at enough representative elementary volume (REV) samples to represent reservoir size, which makes it the major link between pore and reservoir scale simulations (Xiong, Baychev, & Jivkov, 2016).

Gas production from subsurface reservoirs requires the consideration of both pore-scale and reservoir-scale properties. Studies on two phase flow of gas and brine using pore network models had started in the mid-20th century. (Fatt, 1956) proposed the network of tubes method to simplify the representation of porous media, while (Gruesbeck & Collins, 1982)converted the porous media to parallel plugging and non-plugging pathways. This model was able to represent the effect of flow of fines on the system and showed drop in permeability near wellbore regions. Pore-scale networks are constructed to simplify the complex geometry, while saving computational time compared to particle passed methods like lattes Boltzmann, in exchange of compensable accuracy differences. (Maroudas & Eisenklam, 1965a, 1965b) derived from Kozeny equation a theoretical relation of pressure drops to fine concentration in pores. (Jerauld et al., 1984a, 1984b) used Monte Carlo simulation to show that using spherical pore network yield similar connectivity and accessible volume fraction to using 3d Veroni network to represent the pore space as 3d planes. This approach is not common as micro-scale flow depends on interfacial radius

and interfacial fluid body. Therefore, it is better represented by using the inscribed radius. (Sahimi et al., 1990) showed that pore network is sensitive to change of fines concentration as the presence of fine changes the void space. (Imdakm & Sahimi, 1991) Developed Monte Carlo computer simulation model to study fines migration using 3d pore network models. In this model, the path of fines was traced as it flowed in the pore network. Percolation threshold is represented as the minimum fraction of open pores at which medium connectivity is lost due to fines accumulation in the pores. (Bigno et al., 1994) identified five pore blocking mechanisms due to fine particle and linked them to production drop models for flow prediction. The main shortcoming of previous works is that they do not give priority for spatial properties of the pore space when studying the pore networks, rather statistical methods were used from 3D reconstruction. Although (Hilfer, 1991) used local porosity as a descriptor to increase the accuracy of statistical method, such approach does not properly reflect the pore geometry. Later, (Bryant et al., 1993a) used a grain passed approach, to generate from a pack of spheres, a pore network by expanding spheres in the pores until they overlap. Although the method resulted in more accurate pore networks compared to previous work, the limitation was that it can be only applied on spheres of the same size. (Bakke & Øren, 1997; Bakke & Øren, 2002) overcame this issue, by successfully using μCT images to produce pore network that are representative of sand and sandstone; they also were able to generate two-phase flow simulations results that were representative of the actual experiments.

c linked micro computed tomography images to flooding experiments of fines retention in glass beads, utilizing pore networks and water flooding experiments to quantify the impact of fines and predict permeability. More recently (Han et al., 2018) used CT scans at 107 μm resolution to study fines migration due to depressurizing hydrates in sandy sediments.

Given that fluids are controlled by transport phenomenon at pore-scale, there is a shortage in literature of studies of fines impact at 3D microscale in sand especially with gas flow (Two-Phase Flow). This work arguably for the first time, study the effect of different fines types and contents on real sand packs imaged using μCT from synchrotron radiation, imaging the gas flow as it progresses through sediments. High brilliance synchrotron X-ray micro-computed tomography was used allowing fast reconstruction of the spatial information which is an advancement over other scanning methods. This technique was used to image live experiments of CO_2 gas flow in unconsolidated fully saturated sand columns with different fine particles content and types (Jarrar et al., 2018). This work will be useful in many areas and applications, including but not limited to production of conventional and unconventional fossil fuels, filtration, contaminant transport, and underground water storage.

CHAPTER 3. METHODOLOGY

3.1 Experimental Setup

The experiment consists of six small acrylic columns packed with a saturated mixture of sand and fine particles. Two different types of fines were used, hydrophobic (kaolinite) and hydrophilic (montmorillonite). At the start, the columns are fully saturated with brine, then CO_2 gas is injected to replace the brine to cause a flow that induces fines migration (Jarrar et al., 2018; Jarrar et al., 2019).

The design aims to study the behavior of gas flow through unconsolidated porous media of sand; to understand the impact of different types and concentrations of fine particles on the pore morphology and how that will affect the two-phase flow of gas and brine in a saturated medium. Methane hydrates are commonly found in sediments beds that are primarily formed of loose sand. These sediments are in oceanic environments that are fully saturated under the deep sea (Hyodo et al., 2014). In a typical gas well, the concentration of fines in the sediments increases radially with the flow direction toward the well (Yamamoto *et al.*, 2014). In order to replicate such conditions, sand was mixed with fines, then the loose dry sand-fines mixture was packed in deposition layers in the acrylic tubes. During packing the brine was added gradually to replicate a fully saturated marine environment.

3.1.1 Sand and Fine Particles (Kaolinite/ Montmorillonite)

The properties and types of sand and fines are selected to reflect the sediments found in similar environments where methane hydrates were discovered in (Boswell et al., 2012; Cook & Malinverno, 2013; Dai et al., 2004; Mrozewski et al., 2011). The selected sand is F75 Ottawa silica sand. A fraction of the grains size was selected by using US sieves #70 and #60, resulting in grains dimensions between 250 micrometers and 210 micrometers respectively. The sand was sourced from US Silica Company,

with a specific gravity of solids (G_s) of 2.65. Two types of fine particles were used, hydrophobic and hydrophilic. This allows the study of the different flow phenomena caused by migration due to gas flow of different fines. Kaolinite fine particles are more hydrophobic compared to the montmorillonite fine particles which are considered hydrophilic. The used kaolinite fine particles are commercially named Dixie Clay Kaolin and they were sourced from the Vanderbilt Minerals Company, TN, USA. The average fine particle size is 0.6 μm while the specific gravity of solids (G_s) is 2.62, which is very close to that of sand compared to the rest of the system.

3.1.2 Mixture Ratio

In realistic reservoirs conditions, fine particles are present in a mixture with the existing sediments. To simulate this condition, the silica sand is mixed with fines before placing it in the test columns, fine particles are added as a percentage of the sand weight, and six different sand fines mixtures were prepared. In Table 3.1.1, each type of fine is in the same row with 3 different fines mixtures, the ratios are increased incrementally for both kaolinite and montmorillonite.

Table 3.1.1: Types and Quantity of Fines Added to Columns as Ratio of Sand Weight

Fines Type	**Percentage of Sand Weight**		
Kaolinites	2%	4%	6%
Montmorillonites	2%	3%	5%

In addition to replicating different fine concentrations, the mixture must also represent a sand dominant sediment in its behavior. In this setup the mixture proportions must not recreate a clay dominant sediments with a relative high fraction of fine particles, as this will alter the behavior of sediments. In a clay dominant sediment with high fines fraction, the effective stress have a major impact on the sediments behavior. At low effective stress the sediments behave as clay dominant sediments, while at higher effective stress this behavior is altered due to consolidation of clay, resulting in a behavior similar to sand dominant sediment (Han et al., 2018.). The aim of this experiment is to simulate unconsolidated sand sediment were fine particles do not carry loads in the system. To do so Equation 3.1.2.1 is utilized; the equation uses the concept of (J. W. Jung et al., 2012), that the critical fine particles content in a sediment is reached when all the voids between the sand are filled with fines. The critical fines content (FC) is directly related to the ratio of mass of sand and mass of fine particles. Later an analysis on coarse sand mixture was carried out using gravimetric-volumetric analysis by (Park & Santamarina, 2017). This showed that the FC can be formulated as in Equation 3.1.2.1 below.

$$FC = \frac{e_s}{1+e_s+e_f}$$ Equation 3.1.2.1

Where void ratio of sand is e_s and void ratio of fines is e_f. The targeted porosity for this experiment was 40% to simulate loss packing of unconsolidated sand sediments in saturated marine environment. Void ratio e_s is the volume of void over the volume of sand, at 40% porosity e_s = 0.67, for this setup FC was estimated to be equal to 21% where e_f is 1.5. Given that the highest fine particles concentration used in this experiment is 6% of kaolinite, the critical fines content can be estimated after

calculating the void ratio of fines e_f, in order to compare e_f with e_s the difference in specific gravity of solid is calculated, where 6% of fines in weight of sand is equivalent to 6.07% volume of sand, as the specific gravity of solids G_s for sand is 2.65 while G_s of fines is 2.62. Such difference is small that it can be neglected, those calculating FC at 6% kaolinite results in FC = 8.04%, which is far less than the estimated critical FC = 21%; those due to the low fraction of fines it is assumed that the setup design will not result in fines that carry the loading. This means that when studying fines migration, the effective stress in these systems will have no to minimal effect, therefore the only confining stress that was applied is due to the self-weight of particles of the silica sand.

3.1.3 Columns Size

The size of the sample is one of the most important aspects in every fluid simulation experiment. The dimensions should be large enough to be a representative volume of whatever medium under the study, while it should be also small to the degree that it allows the study of flow phenomena at the microscale with the current laboratory capabilities. Given these assumptions, the fluid movement occurs at the pore-scale and is affected by the capillary forces, the sample dimensions are chosen to be representative for that scale. The internal size of the used acrylic cylindrical column cells is 9.52 mm in diameter and 50.80 mm in height (standard 3/8 in diameter by 2 in height cylinders).

3.1.4 Packing

The approach in which the sediments are placed into the column is of a special importance. The packing method of the sand fines mixture should be consistent for all the specimens and it must also reflect the way natural in which sand sediments would be packed in saturated environments. In nature, sand is formed by deposition of

sequential sediments beds on top of each other due to depositional and climatic conditions. To replicate this natural occurrence the sand-fine mixture is packed in five vertical layers in the cylindrical cells. Initially brine is added to the empty cell, the amount added is only enough to cover the first layer of sand-fine mixture, then the first fifth of the cylinder height is filled with the sediment's mixture. Next more brine is added in an amount that is enough to cover the next layer and so forth until all the five equal sediments layers are packed. To finish packing, each column had two filters installed from the top and bottom sides.

3.2 CO_2 Injection

Since the aim of the experiment is to study how different fines concentration will alter gas flow in a porous media of sand, gas must be precisely injected in a systematic manner in each cell to allow the comparison of the resulting different gas flow patterns. In order to capture the gas volume during the experiments run, the acrylic cylinders are placed vertically between two ports.

The lower port is used to inject gas, a hosepipe connects the inlet of the bottom port to a pressure regulator, and this regulator is connected to a CO_2 gas source. Carbon dioxide gas was selected for this experiment; because it is safe to handle in small volumes, and it relatively have similar fluids properties to air and natural gases found in subsurface reservoirs (Cao, Dai, & Jung, 2016); specifically, when compared to the properties of the other fluid in the system which is water-based brine. It is also of increasing interest for CO_2 sequestration applications.

The top port is connected by another hosepipe to a flow pump (DigiFlow) pressure-volume actuator. It is designed to pump water out of the sediments specimen column at a controlled steady rate. Both the upper and lower ports consist of perforated plates, glass beads and fine mesh filter. The perforated plates and the glass beads help

in the transition of the flow from the upper or lower port to the sediments in the cylindrical column by making the stream lines distributed in a parallel manner when entering then exiting the sediment system. The fine mesh filter prevents the fine particles from entering the flow pump or the pressure regulator.

Each of the six different columns had four different saturation stages. Initially the columns are fully saturated with brine, then CO_2 gas was injected through the regulator at a constant pressure of 27.6 kPa (4 psi), while the flow pump pulls out 0.4 ml of the brine solution. At the third stage, the DigiFlow pump pulls out a total of 1.0 ml of the brine solution, while the CO_2 is continuously injected at a constant pressure of 27.6 kPa (4 psi). At the fourth stage, gas pressure was increased through the pressure regulator to reach 41.4 kPa (6 psi) without ejecting any additional volume of brine; the motive of increasing pressure without flowing out any brine is to observe the changes in the flow of gas internally between the sand grains. As the pressure increases the radius of curvature of the interfaces between gas and brine changes inducing altered permeability. (Mining, 1939). Table 3.2.1 show all the stages captured for this experiment, for the 2% montmorillonite column only stages 1 and 2 were captured while the 3r and 4^{th} stages were skipped. This was done to take zoomed scans with higher resolution for another study. The total of the scanned soil systems is 22. In Figure 3.2.1 the effect of increased fines concentration can be observed, at 6% of kaolinite the fines clogged the throats, when the gas was injected, it caused enough pressure to mobilize the sand grains inducing a fracture. Gas steps injection are shown from the full saturated stage one to stage 4 from left to right where the fracture was first observed at (b) when the first volume of CO_2 was injected.

Table 3.2.1: Injection Stages of Gas in Each Soil System for a Given Fines Content

Fine Type	Fines%	Injected CO_2 (ml)			
		0	0.4	1.5	1.5
Kaolinite	2	☑	☑	☑	☑
	4	☑	☑	☑	☑
	6	☑	☑	☑	☑
Montmorillonite	2	☑	☑	☒	☒
	3	☑	☑	☑	☑
	5	☑	☑	☑	☑
CO_2 Pressure (kPa gauge)		27.6	27.6	27.6	41.4

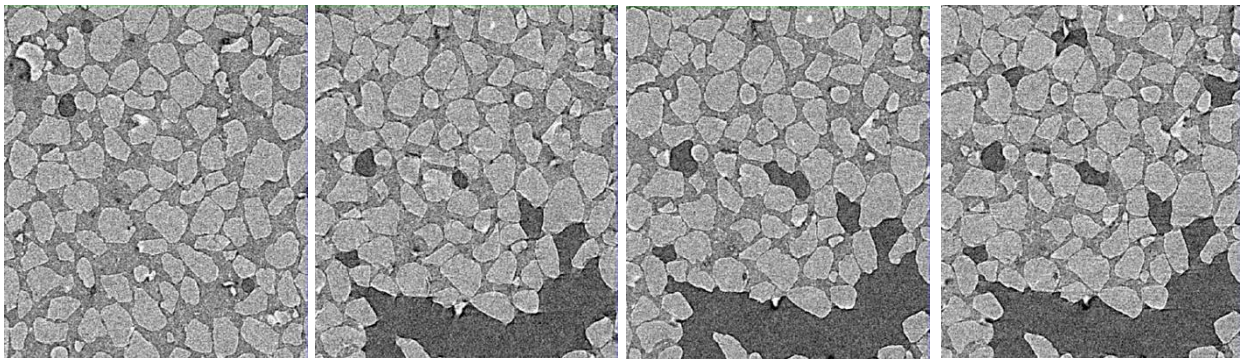

(a) (b) (c) (d)

Figure 3.2.1: top view slices of the obtained 3d images showing stage 1 to 4 from (a) to (d) and gas fracture for 6% kaolinite, gas is observed mobilizesing sand grains.

3.3 Scanning

The preparation and scanning of the soil samples was carried out at Argonne National Laboratory (ANL) Synchrotron, Beamline 13D of the Advanced Photon Source (APS), USA; it was used to acquire the X-Ray Synchrotron Micro-Computed Tomography (SMT) scans (Jarrar et al., 2018). Each of the 22 soil systems were

scanned four times, the scanned volume represents 11.24% of the total volume of the sample. The synchrotron source X-Ray radiation have the advantage of being able to control the beam energy level (Sokolov et al., 1966), this advantage was used to take two scans for each region, one with high energy level and another with lower energy level. This was used to increase the contrast of the phases in the image; a special brine was utilized to get these results.

3.3.1 Micro-Computed Tomography and Synchrotron Source Radiation

In many fields, X-Ray imaging is a well proven examination technology that do not cause damage to the subject, since the first successful demonstration in 1895 (Röntgen, 1896), many new emerging methodologies pushed the boundaries of this technique. For imaging applications that require non-destructive examination of samples at the micro-scale or smaller, X-Rays have the advantage of penetrating thick samples, something that Electron Microscopy (SEM) cannot do as it reflects of the surface (Goldstein et al., 2017). This ability allows imaging of full-sized core samples, where the shade of the X-ray can be captured. Another issue is the reconstruction of the X-ray shades from 3D scan of a sample. This was solved through inverse radon transform for back projections. The inverse of radon transforms allows reconstruction of 3D gray-scale intensity image from several X-Ray shades projections. These powerful techniques allow researchers to look inside of materials. (Ambrose, 1973; G.N, 1973; Perry & Bridges, 1973) were the first to successfully demonstrate a 3D reconstruction of human brain, and to characterize materials based on sensed X-Ray intensity using Hounsfield number (or CT Number). A major challenge was the intensity of the X-Ray and the sensitivity of the detectors (were shades are casted). When the energy and intensity of the image is not high enough, very few photons will

pass through the sample to the detectors resulting in noisy low contrast images (electronics, 1961). This challenge required scientists to construct big powerful light source machines to produce high intensities X-Ray. The most successful of which is Synchrotrons (Blewett, 1988; Blewett, 1998). In this work, high brilliance Synchrotron source radiation is utilized to scan the samples and reconstruct 3D grayscale intensity images, showing with high accuracy the internal features of the columns. Electromagnetic accelerators that are laid in a ring shape were used to accelerate the particles and keep their speed up in the storage ring. Subatomic particles are accelerated in the synchrotron rings, resulting in X-Rays ejected in a direction tangent to the ring toward a beam line. In the beam line, the X-Ray penetrate the sample as it rotates, the X-Ray passes through the sample and the data are collected on the detector (Krane & Halliday, 1987; Whrele & Nielsen, 1988). For each sample the scan is done 4 times to capture the gas flow and its effect on the sand grains distribution.

3.3.2 Period of Scan and Speed

The scan of the sample is done by rotating it along its height and taking multiple projections as it rotates, 180 projections are taken for each scan, the scan period is 30 minutes. In order to capture fluid and sand grains movement at this scanning speed, scans were achieved in a multi-step technique. The pump is operated to extract specific amount of water, therefore letting gas enters the system, then the image is taken at quasi-static conditions capturing the spatial details. This is done 4 times for each step of gas injection for each system as detailed in Table 3.2.1.

3.3.3 Field of View

Although the full column dimensions can be captured in theory at lower resolution, the selected approach was to capture the middle of the columns for the following reasons:

- Narrowing the field of view increases the image resolution, lowering the voxel size. This is especially beneficial when the goal is to binarize the image for fluid simulation at the pore scale. Higher resolution will provide details of the pore morphology in a refined way, and will limit the effect of the building blocks shape, which are cubic voxels especially on curved surfaces (Fernandez-Carreiras et al., 2005; Stampanoni et al., 2002; Tonner & Harp, 1988).
- Horizontally when the regions near to the walls of the column are ignored, this will eliminate the effect of the boundary on the pore morphology and fluids movement, resulting in continues behaviors similar to the circumstances encountered in large aquifers (Alshibli et al., 2014).
- The current capability at the testing facility in Beamline 13D in APS ANL, is to reconstruct a stack of 1920x1920x1200 voxels. Thus a suitable size that's large enough but with a high resolution must be selected.

Two stakes are vertically captured and merged resulting in image size of 1920x1920x2356 voxels. Voxel size is 3.89 micrometers, meaning that the image size is 7.469 mm in diameter and 9.165 mm in height. This is captured out of original column dimensions of 9.520 mm and 50.200 mm for diameter and height respectively, which is equivalent to 11.24% of the total internal volume of the cylindrical acrylic column. In Figure 3.3.1, elevation projection is showing the dimensions of the image's stakes in (a) while in (b) the measurement for the overlapping are drafted.

Physical Dimensions and Location of Stacks:

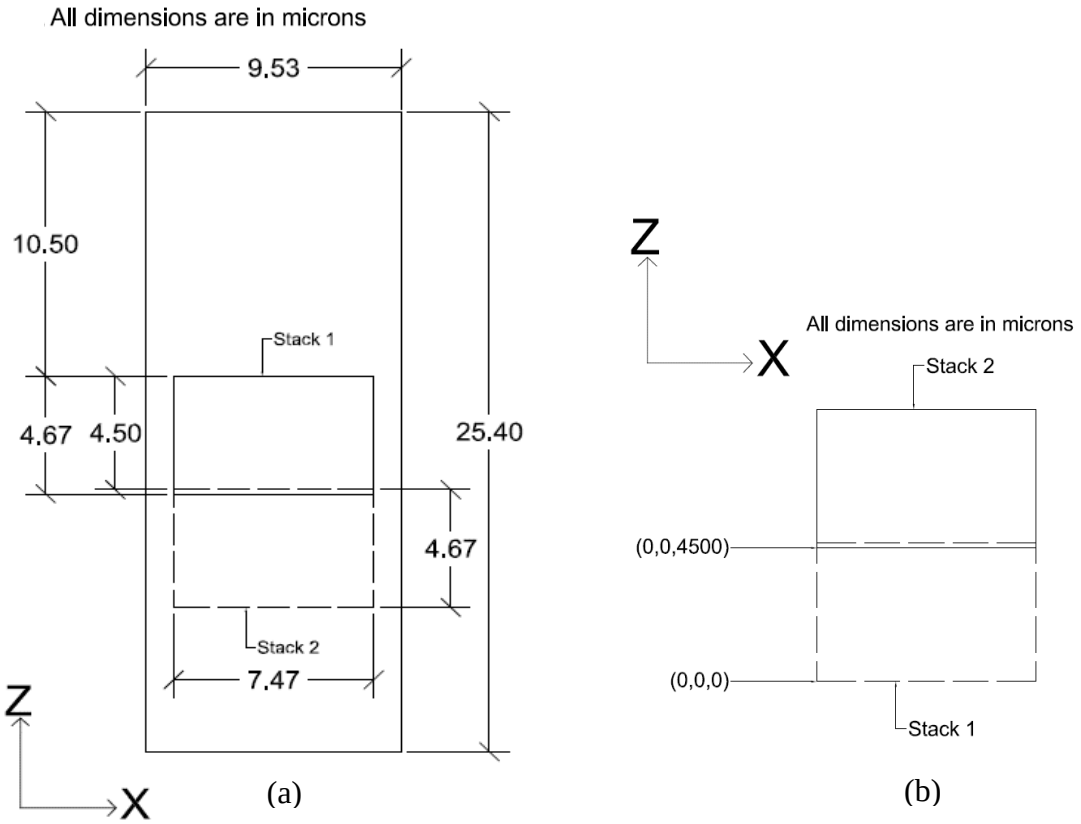

Figure 3.3.1: (a) elevation view of the cylindrical cells showing the location of the images, (b) overlapping of the imaged stacks, (Zaher, 2019).

3.3.4 KI Brine for Enhanced Contrast

For each of the 22 systems representing all the columns and the injection cases, two different images were captured using doping agent; one highlighting the gas body and the other one highlighting the morphology of the sand grains, this is achieved with the assumption that during the scan, the fluid and grains are static. This technique is effective in increasing the image contrast, which will result in better features detection when binarizing the image, and it will also limit the effect of noise in post processing. To do so, a salt is added to the deionized water to form the brine, the resulting mix would have a useful property which is when imaged at X-Ray with energy level higher

than a specific value (radiation edge) it will appear brighter in the image with higher intensity value (CT Number), while if the energy level of the X-Ray is below that edge it, will have water like intensity, hence the addition of the two images will result in enhanced contrast. For this experiment 2% of potassium Iodide (KI) (by weight of water), was dissolved in the water. Increasing the concentration of KI can lead to changes in water properties, the value used is well within the limits as other studies used higher concentrations with minimal effect (Andrew et al., 2014; Iglauer et al., 2013).

3.3.4.1 Energy levels of synchrotron

One advantage of the synchrotron source radiation is the ability to adjust the X-Ray energy level with wide ranges that other X-Ray sources cannot produce (Brunke et al., 2008). APS can store beam energy up to 7.7 GeV (Whrele & Nielsen, 1988), this advantage is used to produce two energy levels; one above the potassium Iodine edge and the other below. At first X-ray is used with energy level of 33.069 keV which is below the edge of KI, two stakes are imaged. Then for the same system another tomography for the same two stakes with 33.269 keV X-Ray is taken. From inspecting the results, the KI amount of 2% by weight of water resulted in brine with good contrast when the images are combined by the addition of the gray-scale image's CT number.

Figure 3.3.2 shows the DigiFlow pump (pressure-volume actuator) and pressure gauge. Figure 3.3.3 shows the setup, the X-Ray radiation is directed toward the beamline and released to penetrate the sample on left. The sample is connected to the top port to extract water and the bottom port to inject CO_2, through the green hosepipes, the sample is rotated around its height and the X-Ray is reflected by the mirror and its projection is casted on the camera sensor (Jarrar et al., 2018; Jarrar et al., 2019).

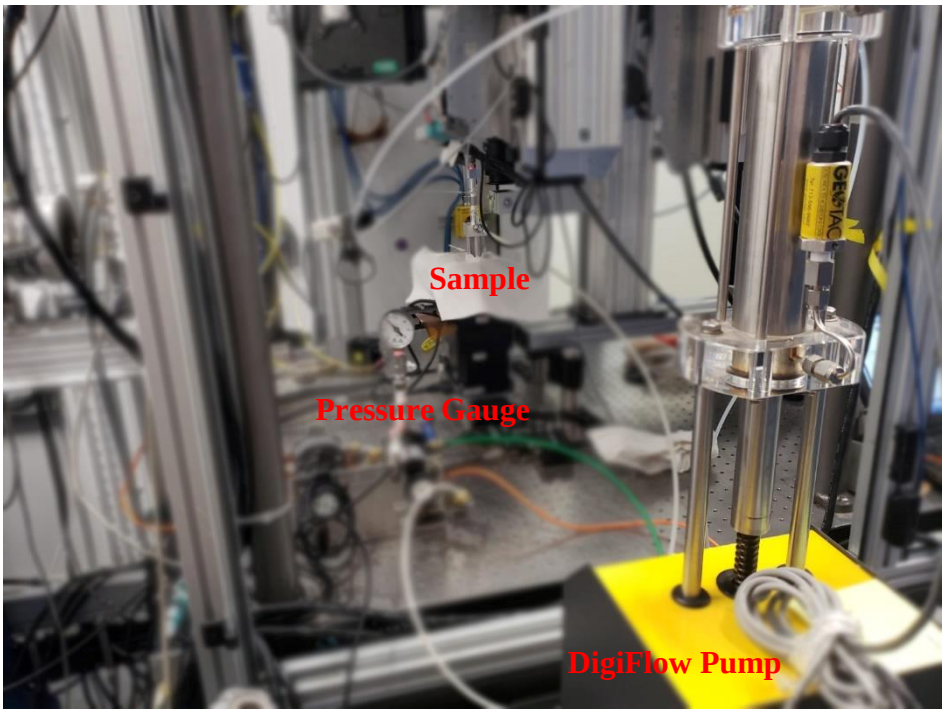

Figure 3.3.2: DigiFlow pump and pressure gauge connected to sample

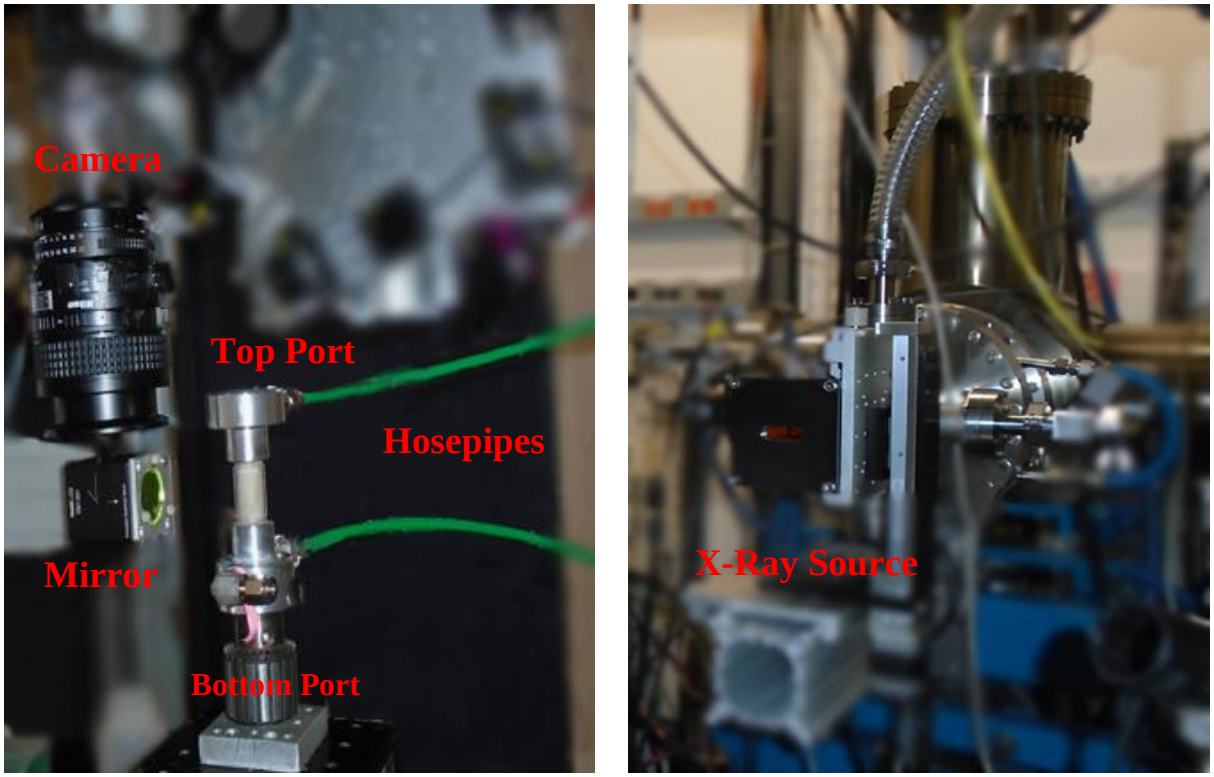

Figure 3.3.3: experiment at beamline 13D at APS ANL. (Jarrar et al., 2018, 2019)

CHAPTER 4. ANALYSIS

4.1 Image Reconstruction

The reconstruction is the process of using two-dimensional X-Ray projections for a sample taken at different angles. The intensities for each projection will reflect the sum of what the X-Ray beam passed through the sample at a given angle, brighter regions mean that more dense material was penetrated and vice versa. Using projections that represent the sample from different angles as it rotates, specifically 180 projections; the three-dimensional volume of the sample can be reconstructed using reverse radon transform. Figure 4.1.1 shows an example of the reconstruction of a single slice from 180 projections. It is evident that the resulting reconstructed image can accurately describe the original sample, even with the resulting artifices. Using the same methodology, the scanned specimens are reconstructed slice by slice and combined to give 3D grey-scale intensity image.

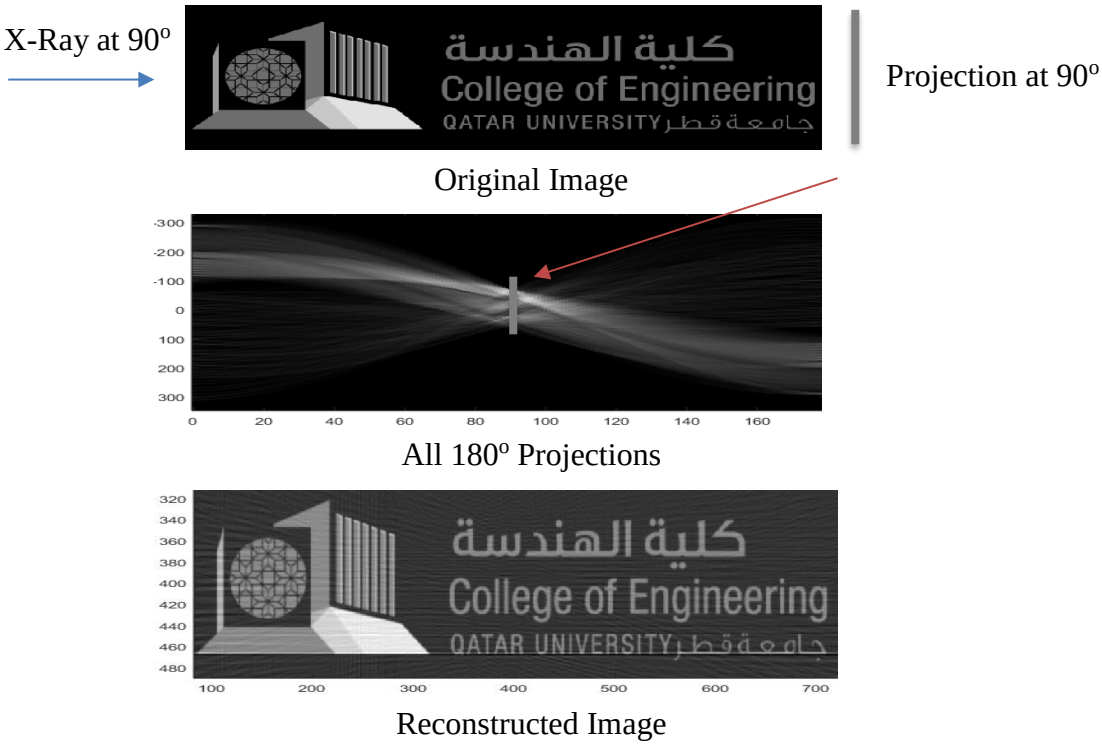

Figure 4.1.1: reconstrction of orginal image using 90 projection at 180° degrees

4.2 Image Merging and Cropping

As discussed in section 3.3, in order to scan a bigger, more representative volume of the cylindrical column, two stacks for each system were imaged. While imaging the stacks, their positions were designed with a specific overlap to ease the process of merging them in one image. As showed in figure 3.3.1 the second stack is always transformed by 4500 microns in the positive z direction (height). Sequentially each two stacks representing the same system are then merged. This is done for images with the high and low X-Ray energy levels resulting in 44 images for the 22 system (from originally 88 scans). The region overlapped is of a height of approximately 168 microns, which is considered as proper height to note any problem (variation in topographies) when merging. All the images where merged flawlessly without any artifacts. Figure 4.2.1 show, the size of a single stack before merging on the left, while the final size after merging is displayed on the right.

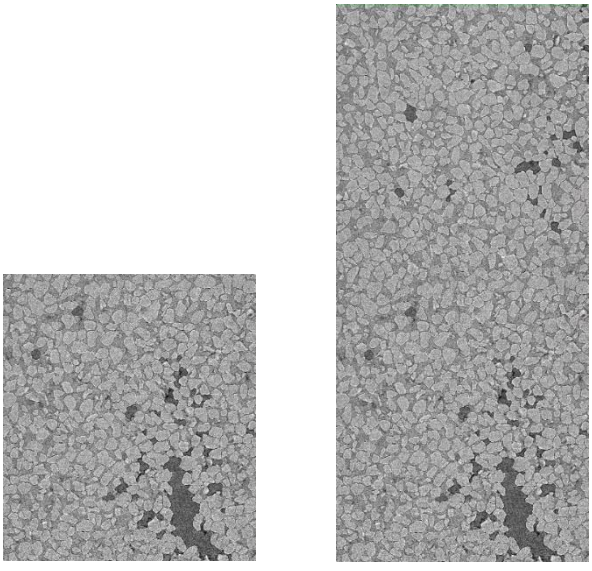

Figure 4.2.1: single stack of 1200 voxels height (left) while merged stacks with 2356 voxels height (right)

After merging was complete, for each system the two images with X-Ray energy levels above and below KI edge were combined. This was done using scaler addition of the values or intensities of each voxel. Given that the images above KI edge have very dark gas phase (low CT Number), while the ones below KI edge have sand with brighter intensity relative to the reset of the image (higher CT Number), the resulting gray-scale image would have increased range for the values between the dark and bright voxels. This gives more contrast and helps with the later steps of analysis. All images were cropped to reduce beam hardening effect and produce the best consistent results. The cropped images size is 1080x1080 voxels which was originally 1920x1920 voxels as seen in Figure 4.2.2.

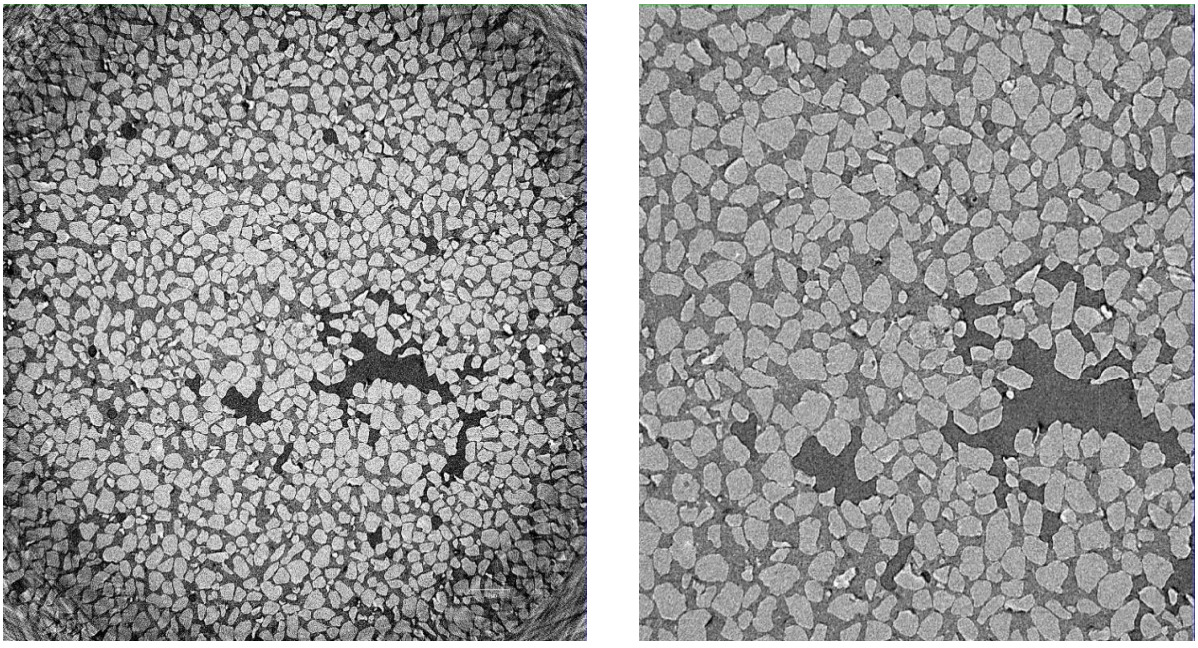

Figure 4.2.2: top view slices, before crop (on left), and after crop to eliminate beam hardening (on right)

4.3. Image Filtering

The first step in image post-processing is to filter the raw data. The filtration allows enhancing the details of the image and corrects the artifacts or noise that might be induced from low exposures. The raw data in this work are three-dimensional intensity images reconstructed from multiple exposures of X-Ray images. This process of creating the image results in a group of artifacts that require filtering. Another issue is that each X-Ray exposure results in a projection with noise that need to be filtered. In order to obtain the best results, a group of filters and filter combinations were tried on multiple small samples, Table 4.3.1 shows the relative the strengths and weaknesses of the best filtering methods for the used data. Since the aim of filtering is to prepare the image for segmentation (binarization) through the selection of threshold values, the best filter must preserve the phase interfaces (edges) while blur or unify the intensity values inside the phases. A combination of Anisotropic Filtering followed by Median filtering was found to yield the best results considering computation time, while the non-local mean required more computational time to yield similar results.

Table 4.3.1: Relative Comparison Between Different Image Filters

Filter	Anisotropic Diffusion	Median	Non-Local Mean	Gaussian	Curvature-Driven Diffusion
Computation	Fast	Fast	Slow	Average	Average
Edge Enhancement	Effective	Average	Effective	Poor	Average
White Noise	Effective	Effective	Effective	Effective	Average
Black Noise	Effective	Effective	Poor	Effective	Average

4.4. Anisotropic Diffusion

Anisotropic Diffusion is a non-linear space variant transformation. It is an image filter that uses a generalized diffusion process that utilizes the original image and a two-dimensional isotropic Gaussian filter. The filter is also known by its creators name, Perona–Malik diffusion (Malik & Perona, 1990; Perona & Malik, 1987). The filter works on reducing the noise in the image while preserving the contrast of the edges, thus conserving the features and details. The filter works as follows: it uses features from the original image scaler values on regions with high contrast (phases' edges), while for the internal part of the phases (with low contrast), it generates convolutions of increasingly blurred scaler values and assign them to these regions with low contrast. The result is an image with conserved edges and details while the noise inside of the phases is blurred. Hence the name is anisotropic diffusion, because the filtering is not done isotopically without considering the edges.

The filter will continue smoothing until a given criteria is met, (Bernard et al., 2011). In order for the algorithm to determine the new value of specific voxel, it compares the value of that voxels with its six neighboring voxels on the faces of the cube; if the difference between the new value and old value is more than the limit it stops. In this way, the edges are preserved while the internal parts of the image inside of the same material are blurred.

The following formula Equation 4.4.1 controls the algorithm:

$$\frac{dImg^t}{dt} = \nabla(D(Img^t, t)\nabla I^t) \qquad \text{Equation 4.4.1}$$

Where: Img^t is the image at time; while D is the diffusion function.

The discretization with respect to time is represented in Equation 4.4.2:

$$Img^{t+1} = Img^{t} + \frac{dt}{c}\sum_{m=1}^{6}(D_m \nabla\, Img^{t}) \cdot n_m \qquad \text{Equation 4.4.2}$$

Where: c is a voxel side; D_m is diffusion function for the m face of the voxel's; n_m is the face m normal vector;

Equation 4.4.3 represents the 3D spatial values as follows:

$$Img_{i,j,k}^{t+1} = Img^{t}(1 - \gamma \sum_{m=1}^{6} G_m) + \gamma\big(G_1 Img_{i-1,j,k}^{t} + G_2 Img_{i+1,j,k}^{t} + G_3 Img_{i,j-1,k}^{t} + G_4 Img_{i,j+1,k}^{t} + G_5 Img_{i,j,k-1}^{t} + G_5 Img_{i,j,k+1}^{t}\big) \qquad \text{Equation 4.4.3}$$

Where:

$Img_{i,j,k}^{t}$ is voxel value at (i,j,k) coordinates for time t;

$G_m = D_m/D_o$ is a diffusion function with values between 0 and 1;

$\gamma = \frac{dt\, D_0}{c^2}$ is time evolution and is fixed to 1/6 for system's stability;

Noting that G is a function of the difference between present voxel and its neighbor's m. G is defined as:

$$G(\alpha) = \begin{cases} 1, & \alpha \leq \beta \\ 0, & \alpha > \beta \end{cases};$$

where β is the diffusion stop threshold;

Figure 4.4.1 shows an example of the filter stop condition; when the diffusion stop threshold is set to 5, if the difference between the present and the neighboring voxels is less than the limit, the values of the neighboring voxels will be used in the next cycle of the algorithm.

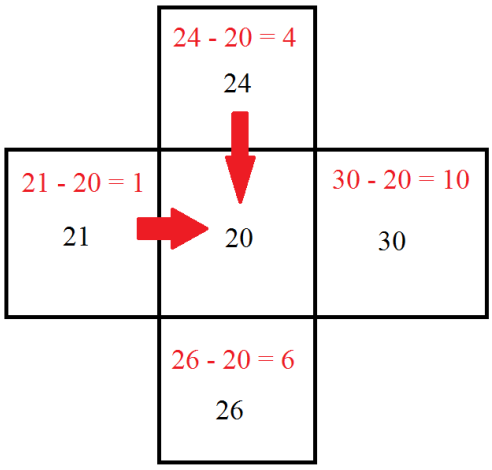

Figure 4.4.1: anistropic diffusion threshold stop criteria

The anisotropic diffusion filter have the advantage of filtering both black and white noise voxels, this is something that powerful algorithms like non-local means do not do as it is only effective on white noise (Buades et al., 2005), additionally the filter can run on multiple graphic cards, exponentially decreasing the computer processing time. The threshold limit was set to 600 CT Number, while the filter was made to run for 5 iterations.

4.5. Median Filter

The median filter works by taking the scaler values of a specific voxel and its neighbors, it then reorders the values from small to large; finally it takes the median number and assigns it to that original voxel. The algorithm runs on three-dimensional basis taking the mean value for the 26 voxels neighboring the targeted voxel.

Given the following example in Figure 4.5.1 for a 2D image with 8 neighboring voxels with values:

9	1	8
2	7	3
6	4	5

Figure 4.5.1: pixels vaules of a 9 pixels 2D image, median filter changes 7 to 5

When reordering the values as {1,2,3,4,**5**,6,7,8,9], the median value is 5 and it will replace the old value of 7 for this iteration. Figure 4.5.2 (c) shows how the median filter is effective in removing speckle impulsive noise (both seen as black and white dots) while not wiping away the edges.

The filter reduces the contrast using a low pass filter that attenuates high frequencies, making each phase more distinct than the previous image (Bernstein, 1987; Brownrigg, 2002; Kundu et al., 2004; Pratt, 2013; Sun & Neuvo, 1994) This is evident in Figure 4.5.2 that shows the frequency relative to grayscale values for an image of 5% montmorillonite, (a') shows a raw image distribution, (b') show the distribution after the anisotropic diffusion, while (c') show the final image after passing through a median filter. Having these distinguished ranges of CT Numbers with higher frequencies for each phase will ease the process of segmentation as follows. The filter was executed with 3 iterations each considering the 26 neighboring voxels in the 3D space. Figure 4.5.2 (a) shows the raw image before and (b) after passing it to 3D Anisotropic Diffusion Filter, while (c) after the Median filter. In (c') the highest peak represents sand, the middle is for brine and the shortest is for gas phase.

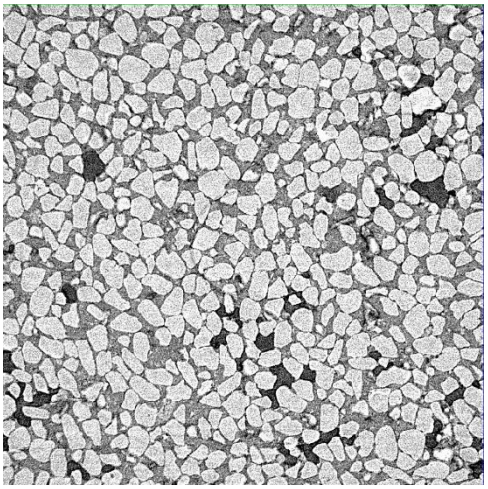

(a)

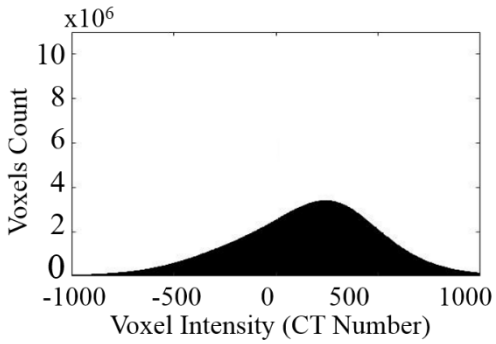

(a')

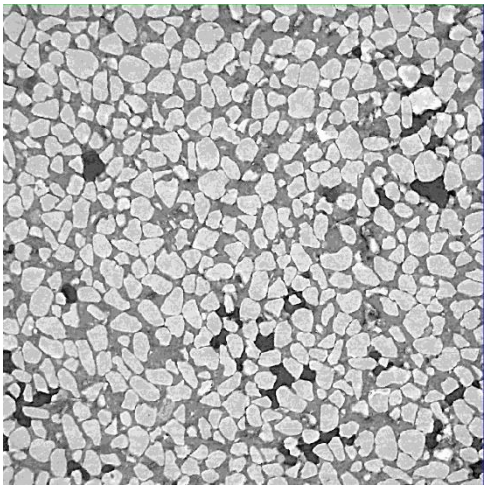

(b)

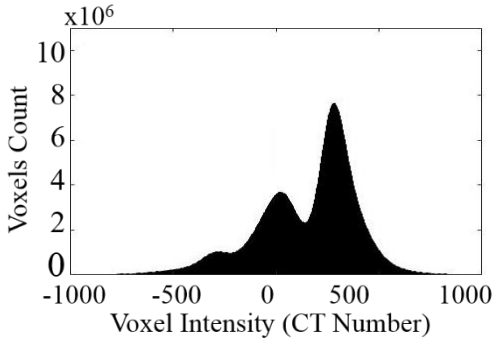

(b')

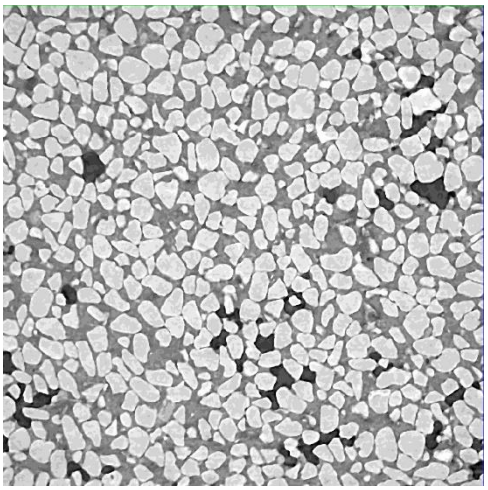

(c)

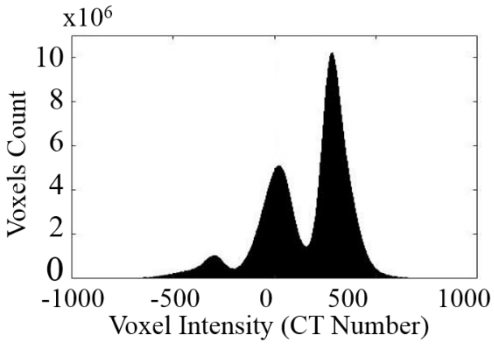

(c')

Figure 4.5.2: filtration sample showing image and the corresponding histogram, (a) raw image, (b) after using anisotropic diffusion, (c) median filter

4.6. Segmentation

Segmentation is the process of dividing certain regions of an image and assigning meaningful values to it. Many approaches to segmentation can be used from manual to automatic thresholding, also feature detection and artificial intelligent computer vision can be applied. To insure the best results, manual segmentation approach was utilized. The image greyscale range was manually segmented by entering CT Number values, the range with high CT Number values resulting from the images of below the KI edge was used to select sand, then the range with low CT Number resulting mainly from the scan above KI edge was used to select the gas, while the resulting unselected range was assigned to brine. Additionally, the fine particles were allocated by selecting a narrow range between brine and sand. After the selection, morphological operations were employed to ensure the best possible segmentation outcomes. As with rest of the analysis, Pergeos software and its algorithms from vsg3d.com Group was used.

4.6.1. Gas Segmentation

The interactive overly thresholding tool was used to select voxels with specific values for each system, for all the kaolinite columns, values less than -150 CT Number were binarized as gas, while values less than -200 CT Number for all the montmorillonite columns were segmented as the gas phase. The selected voxels were given the value of 1 representing the first phase.

4.6.1.1.Gas Morphological Operations

Knowing that there is an overlap in the CT Number range for each phase as shown in green in Figure 4.6.1, and that this experiment imaged immiscible fluid movement through sand; this means that the different phases do not mix. From visually

inspecting the images, small artifacts were present even after filtering and segmentation, something common for tomography images, (Van Gompel et al., 2011). Morphological operations were used to give consistent phases in the image, representing what can be observed visually. For the gas phase, the fill holes then the opening tools were applied, followed by removing small spots.

Fill Holes: when an artifact inside a gas bulb is present and is fully within the body of the bulb, the Fill Holes tool identifies it and assigns it to gas with value of 1, changing the material at that voxel cluster.

Opening: artifacts from X-Ray shadowing effect, resulting from passing materials with higher to lower refractive index instantly, these are removed using the opening tool, the tool removes thin regions that do not represent a gas blub and delete the value of 1 from the selected voxels.

Removing Small Spots: when imaging at 3.89 voxels resolution even microbubbles appear as big spheres, anything smaller than a certain value can be safely considered as artifact, gas blubs with diameter smaller than 2 voxels (7.78 micron where removed).

The outcome of these operations was relatively an accurate representation of the gas phase, with no to minimal artifacts. In one image, 6% kaolinite at stage 2, about 20% of the gas bulbs were found to be artifacts and were cleared using the morphological operations.

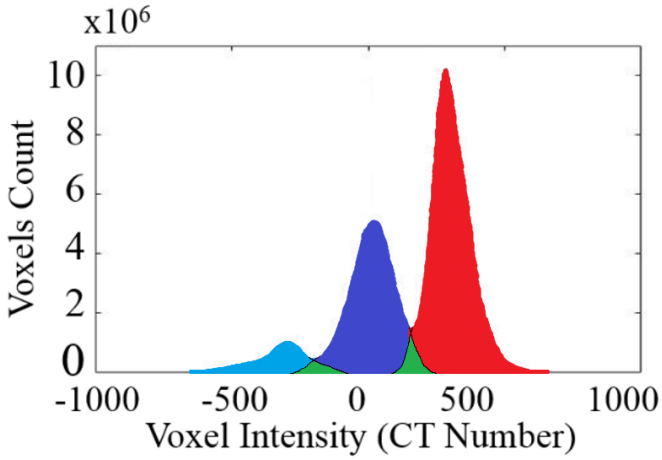

Figure 4.6.1: overlap in CT numbers for phases represed in green, which is an artifcat from tomography

4.6.2. Solids Segmentation

Interactive overly threshold tool was used also to select voxels with CT Number in the range that represented sand. For all the kaolinite columns, voxels with values more than 185 CT Number was segmented as sand with a value of 3. Similarly, for fine particles partitioning (binarization), the range of 120 to 185 CT Number was assigned a value of 4. The remaining volume which represent void occupied by brine was given the value of 2. Water required no morphological operation as all the other phases was processed for artifacts.

4.6.2.1 Solids Morphological Operations

Voxels representing the segmented sand phase were treated with two morphological operations, fill holes and removing small spots;

Fill Holes: help in eliminating any artifact that passed filtering to the segmentation, any individual sand grain is assumed to have solid interior (filled with only sand), the algorithm finds other phases that are present inside and fully surrounded by the sand

phase (inside a sand grain), and change voxels values to be a sand phase with binarized value of 3.

Remove Small Spots: Knowing that the sand grains were sieved and have dimensions between 210 and 250 microns, any individual voxels cluster (sand grain) with dimensions less than 20 voxels (78 micron) is removed. This is evident as the possibility of a single sand grain to break into smaller shatters is weak, given that no high stresses are applied on the sand, nor enough stress from gas movement could be generated.

The study aims at understanding fine particles effect on pore networks, thus fines that are attached to sand and reducing the throat and pore sizes are considered. On the other hand, fines that are suspended in the brine phase are removed, as those will result in inaccurate divided pores when generating a pore network. Hence for fines, the "remove spots morphological operation" was used to remove spots (clusters) in the brine, the removed parts were considered as brine were given the value of 2. While the remaining voxels which represent fines attached to sand are kept with a value of 4. Figure 4.6.2 shows segmentation process for kaolinite cells in (a-c) Column and montmorillonite cells in (d-f) Column, the first row represents raw images, while the second shows filtered counterparts, finally the last row illustrates the segmented corresponding images; Column (g-i) display corresponding histograms.

Although it was demonstrated that fine agglomerate can be segmented, the results will be discussed for only systems with three phases of Sand, Brine and Gas. This is because fines are assumed to be dispersed in the brine; and given that the micro-CT imaging resolution is less that of individual fine particles diameter, in addition to that the brine content of agglomerate cannot be defined without SEM imagery; it is therefore better to assume that fines are dispersed in the brine and focus on studying the effect of sand movements and change in pore morphology due to fines.

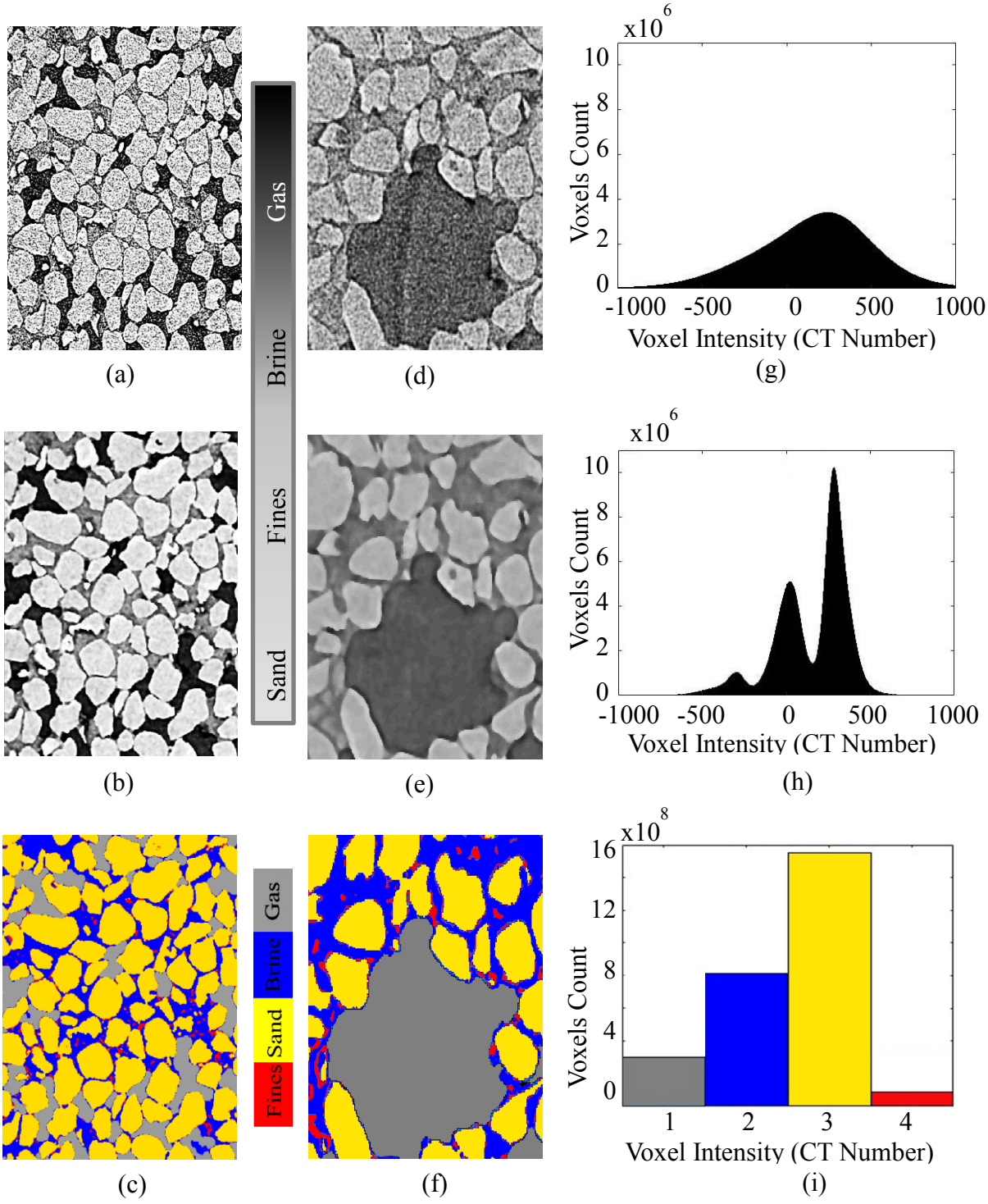

Figure 4.6.2: summery of segmentation for kaolinite cells in (a-c) column and montmorillonite cells in (d-f) column, while corresponding histograms change is in (g-i) column

4.7. Pore Network

The void space is where fluid movement takes place, it has a very complex geometry; pore networks are used to fill this irregular space with simple spheres (pore) and connecting cylinders (throats). This approach simplifies efficiently the complex geometry while keeping important geometrical and spatial information of the void space. Knowing that fluid movement between sand grains is at the capillary level and is governed by capillary pressure expressed in Equation 4.7.1, the geometrical parameter that governs the flow is the radius of the space in which fluids flow into. Thus, spheres and cylinders are the simplest geometrical shapes that can be used to simplify the void space (one radius). This is also evident for the importance of pore networks as they are the most efficient way to describe the connectivity of the void space. A pore network was generated for each segmented image of the 22 systems; sand was considered as solid, while gas and brine were considered as void space. This was done with the aim to study the change in the pore morphology due to gas flow at different fines concentration, thus only sand grains where assigned as non-void, to see how their transformation will affect the pore space and will alter the flow regimes in unconsolidated media. The generated pore networks provide statistics that gives insights to the pore morphology, additionally the networks are used in the two-phase flow experiments.

$$P_c = \frac{2\sigma \cos\theta}{R} \qquad \text{Equation 4.7.1}$$

4.7.1. Algorithm (Grain-Based)

Many different approaches were developed for pore scale modeling using 3d images. These include statistical modeling (Adler et al., 2002); medial axis (Al-Raoush & Willson, 2005), maximal ball (Al-Kharusi & Blunt, 2007). The most effective models

in predicting the properties of sand and sandstones are those that use grain-based approaches(Bakke & Øren, 1997; Bakke & Øren, 2002). The used algorithm starts by creating a skeleton (tree) of the connected void space, lines passing at the center of void regions are generated using slices from the bottom to the top of a binarized 3d image. The junctions at which these lines meet are considered seeds for pores, while a line connecting two pores is a throat. The seeds for each pore are expanded individually until the surface of the sphere touches a sand grain (or an edge of the void space) hence the name grain-based. The generated sphere is an inscribed sphere (by the sand grains) and its radius is used in Equation 4.7.1 for flow simulations. Similarly, the line connecting the two pores pass through a void space; in the region where the line pass, the smallest radius is considered the throat radius and is assigned over the full length of the line, creating inscribed throat body. The radius of the throats is also used in the flow simulations governed by Equation 4.7.1, for capillary pressure calculations.

4.7.2. Verification

To verify that the used model generates inscribed spheres in precise manner without overlapping with the sand grains, samples of sections from a test image were inspected, Figure 4.7.1 displays how the spheres generated from the grain-based algorithm are centered in the void without overlapping the glass beads. Further the statistics for all pores were examined against overlapping with the sand, the result is an overlap less than 7% for majority of pore volumes, Figure 4.7.2 illustrates the statistics for all the pores for system 5% montmorillonite stage 3, the majority of pores have an overlap with sand less than 6% of the pore volume.

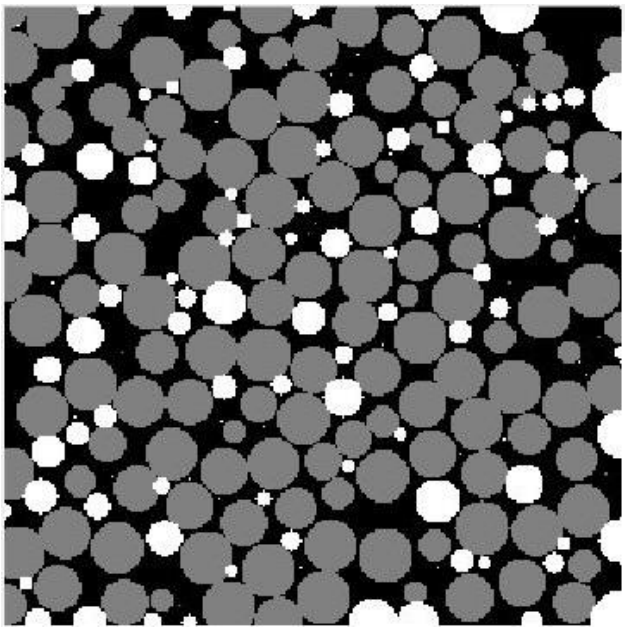

Figure 4.7.1: pores (in white), filling the void space (represented by black), without intersecting the glass beads (in gray)

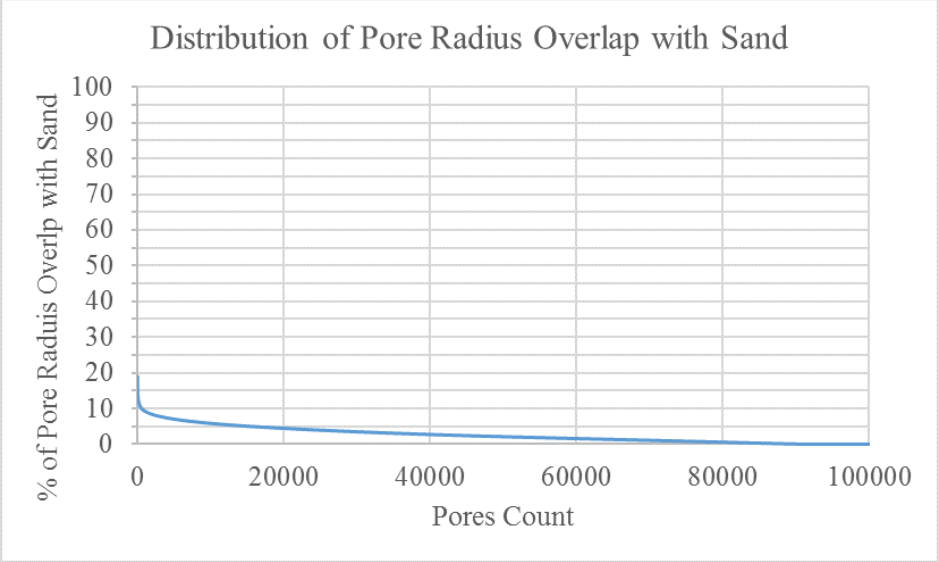

Figure 4.7.2: disterbution of overlap of genrated pores with existing sand

Additionally, throats were inspected visually to assure that they precisely fill the pore space, in Figure 4.7.3 a critical case can be seen in which the throat have a radius similar to its pores, this is an accurate simplification for a fractured region, showing the capability of the grain passed algorithm in sand medium, (a) represents the sand, (b) the void space, (c) the corresponding pore network and in (d) an accurate fit between the sand and the pore network is demonstrated.

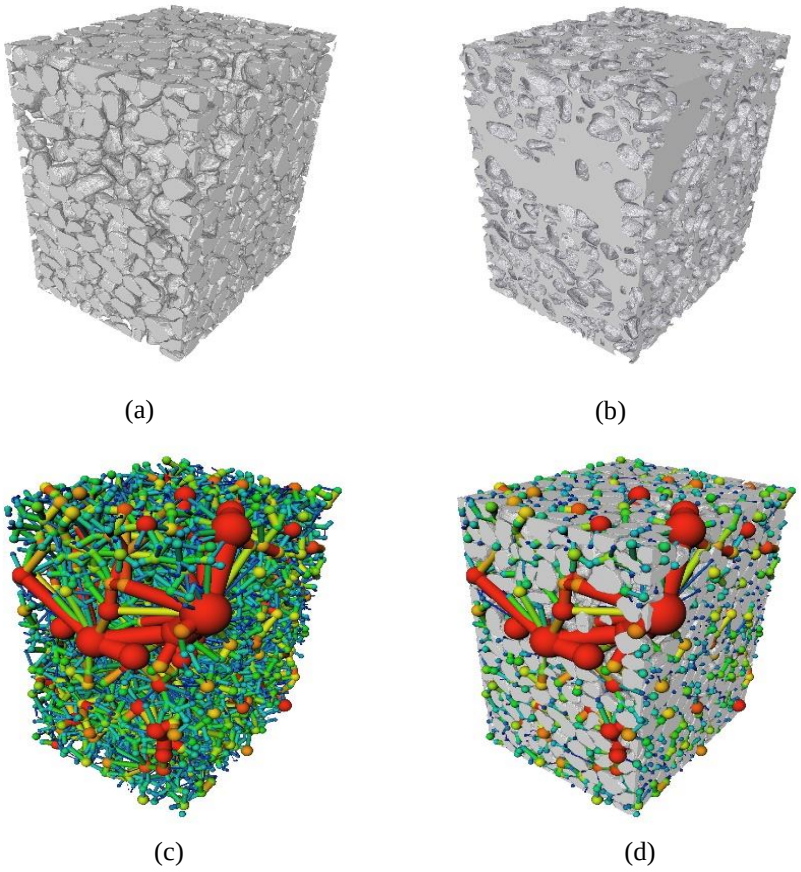

Figure 4.7.3: a cut from kaolinite 6% stage 4, (a) sand grains, (b) pore space, (c) pore network, (d) sand grain and pore network.

4.8. Two-Phase Fluids Flow

The permeability of a medium whether sand or sandstone, is the single most important parameter in predicting the fluids ability to flow through it. Porosity, connectivity and geometry of the pores are strongly associated with permeability (Al-Raoush & Willson, 2005); thus the use of pore networks to calculate the permeability is a very effective flow prediction approach, especially when such a flow is dependent on capillary properties of the void space. Absolut permeability describes a specific fluid ability to cross certain medium, driven by a given pressure difference. Equation 4.8.1 expresses the absolute permeability k, in terms of fluid viscosity μ, the average velocity of the fluid ν, the displacement distance Δx and pressure difference Δp.

$$k = \nu \frac{\mu \Delta x}{\Delta p} \qquad \text{Equation 4.8.1}$$

The study aims at understanding the two-phase flow properties, accordingly relative permeability experiments are studied. A flow of two immiscible fluids in a porous media can be accurately represented using pore networks and simulations of two-phase flow experiments. This was first demonstrated by (Bryant et al., 1993a; Bryant et al., 1993b; Bryant & Blunt, 1992), and by using grain-based pore networks (Bakke & Øren, 1997; Bakke & Øren, 2002).

- The simulations use the geometry of the void space and pore-throats,
- The medium wettability and the contact angle with the sand phase,
- Also, the saturations of the different fluids in the medium.

The relative permeability for a specific phase is defined as the ratio of effective permeability of specific fluid with given saturation divided by the absolute permeability

of the fluid at a theoretical full saturation as in Equation 4.8.1. The definition is formulated in Equation 4.8.2, where k_{ri} is the relative permeability for phase i.

$$k_{ri} = \frac{k_i}{k}; \qquad \text{Equation 4.8.2}$$

$$\text{Where } k_i = v_i \frac{\mu_i \Delta x_i}{\Delta p_i} \qquad \text{Equation 4.8.3}$$

The resulting outcome are relative permeability curves where Equation 4.8.3 is calculated at different saturations of the phase i, whether i is gas or brine. This is done by coupling the effect of capillary pressure from Equation 4.7.1 where the radius of the pores and throats come to affect, also the wettability characterized in the contact angle is implied; the contact angle is assumed to be as quasi-static as the flow in the experiment was slow to the degree that interfaces can be assumed at equilibrium.

4.8.1. Algorithm

A commercial algorithm developed by (Ruspini et al., 2017), was used to compute the relative permeability curves. They consist of relative permeability measurements of both gas and brine versus changing water saturation, about 40 point of measurement was generated for each curve. The algorithm calculates the capillary pressure at entry for pores and throats; accounting for topology of each fluid and uses the spatial information from the representative pore network; The entry pressure is expressed in Equation 4.8.1.1:

$$P_{n\,c} = \frac{2\sigma}{R_n}$$ Equation 4.8.1.1

Where σ is the interfacial tension, while R_n is the radius of curvature which is a function of the angle between the throats, pore and throat radii, and contact angle of fluids.

The algorithm divides any pore-throats coordination into three cases:

- Symmetric pore-throat
- Non-symmetric throat sizes
- Non-symmetric contact angles

Then in order for the algorithm to solve Equation 4.8.1.1 for each pore, the second and third cases are geometrically mapped to equivalent symmetric case and represented by the radius of curvature R_n, the result is a simulation for imbibition and drainage with accurate measurements for relative permeability and capillary pressure, that is done using a pore network that accurately represent the void space of the unconsolidated porous media.

4.8.2. Model Sensitivity to Contact Angle

The used algorithm is very responsive to changes in fluids density, interfacial tension, wettability and the geometry of the pore network. However, there is a lack of sensitivity for changes in the input of the contact angle, this is evident in the sensitivity analysis done for contact angle. Figure 4.8.1 shows no reasonable changes upon dramatically changing the value of the contact angle. Anyhow, given the aim of this work is to study the effect of fine on the morphology of the pore space, this algorithm can accurately serve this purpose as it is sensitive to geometry changes of the pore network.

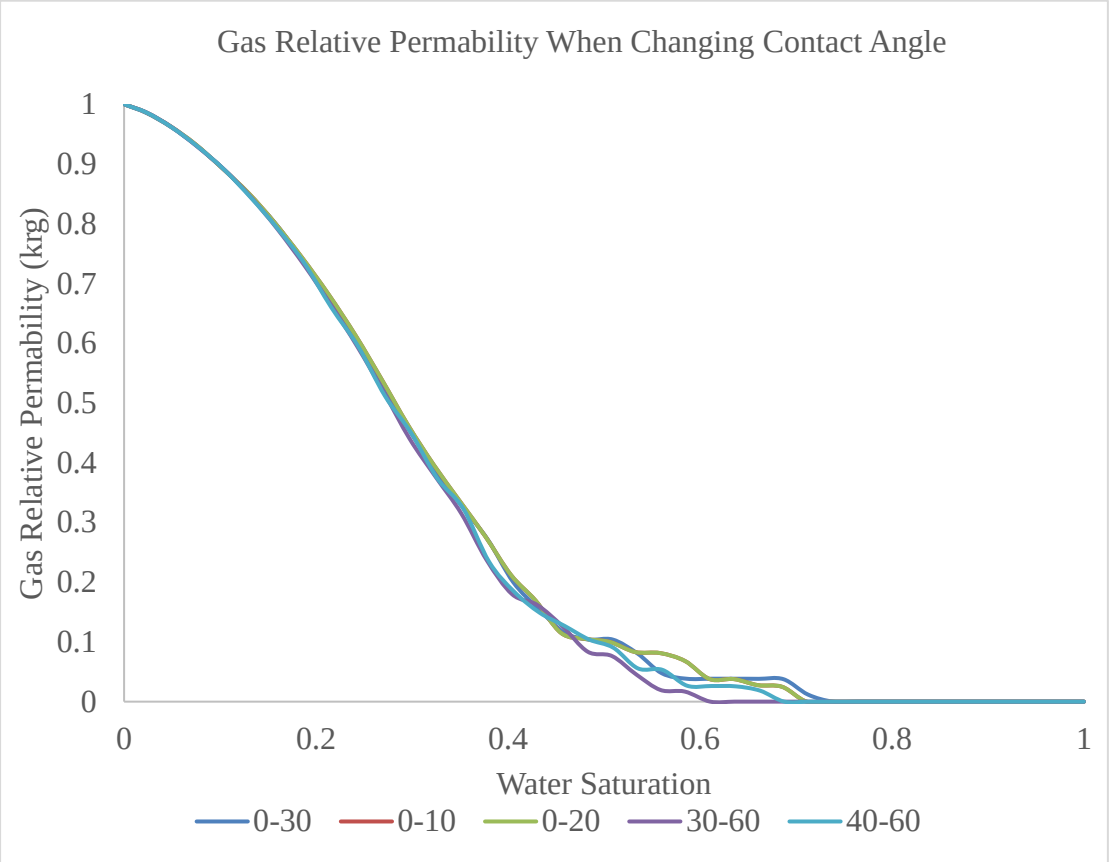

Figure 4.8.1: change in gas relative permability krg, when changing contact angle

4.8.3. Experiments for Primary Drainage

When the gas flows through unconsolidated porous medium, it can change the geometry of the pore space by moving sand grains. This change also depends on the fine concentration in the medium; therefore two phase flow experiments are done for each system of the 20 cases where gas flow in 5 different columns, to understand how changing the morphology of the pore space will impact two phase flow.

The simulation is firstly carried on the sample when it is fully saturated with brine $S_w = 1$, then the pore network is fully drained reaching to the residual saturation of the water (entrapped water fraction). In the simulation, the sample was setup at 90^o vertically and the flow is from bottom to top to simulate the actual experiment and eliminate any small effect from gravity. The interfacial tension between water and gas

is 0.05 N/m from (Saraji et al., 2013), while the density of gas and brine are entered from Table 4.8.1., (Span & Wagner, 1996), brine density was assumed as water given the low concentration of KI salt.

Table 4.8.1: CO_2 and Brine Density at Given Tempreture and Pressure

Phase	Pressure (psi)	Temperature (C^o)	Density(kg/m^3)
Water	4	23.560	997.373
	6	23.560	997.380
CO_2	4	23.560	0.493
	6	23.560	0.740

4.8.4. Experiments for Water Flooding (Imbibition)

Due to the limitation of the pore network generation algorithm, the location of gas and brine in the pores was distributed randomly, however the fraction of gas and brine was accurately represented in the distributed volumes. After each pore and throat had their initial saturation the relative permeability experiment was executed to give the curves for capillary pressure and relative permeability measurements. The other parameters are the same as for the primary drainage.

CHAPTER 5. RESULTS

In this chapter the results from every step of the analysis are shown, raw images are compared with the filtered then the segmented counterparts. The volume fraction measurements are shown for each system, and a 3D visualization for the gas flow patterns in the full volume of the samples are displayed. Representative results of the pore networks statistics, and the two-phase flow experiment are shown. Results for the 2% montmorillonite column are not presented as the third and fourth stages of gas injection were not captured. Nevertheless, the trends for the 3% and 5% montmorillonite fines concertation show comparable trends to that of the kaolinite columns, so it is of great scientific value to discuss them.

Although clusters of fine particles are visible using the micro-computed tomography, knowing that an individual fine particle has a diameter of 0.6 micron, which is less than the voxel resolution of 3.89 micron; the results hereafter are only for systems with three phases of sand, brine and gas. Since fines are suspended in the brine, all the fines were assigned to the brine phase. (Jarrar et al., 2018) demonstrated that when this approach is used, how increasing fines concentration in different columns can be detected using the average CT number of the brine phase. This indicates the capacity to accurately predict the phases from the image data CT Numbers.

Pore networks and the two phases flow experiments are as well discussed for systems with three phases of sand, brine and fines.

5.1. Filtration and Segmentation

A representative set of 2D sections are selected, the sections show the full height of the sample and the different phases from sand, brine and gas. All the sections show the xz axes and are at the center of the sample's y-axis, being at 540 voxel (out of 1080) or 2100 microns from the side. All sections are 1080 voxels in width (4201 microns)

by 2356 voxels in height (9165 microns). Figure 5.1.1 represents the column for 2% of kaolinite at the initial (fully saturated) and final stages of gas injection, at top and bottom respectively. From left to right, first the reconstructed raw image is displayed followed by the filtered image and finally the segmented counterpart; the images show how the gas is able to cause small movements of the sand grains in order to create pathways for its flow, it is evident in the image how the gas is able to create many small pathways that are distributed all over the section. This case is representative to the scenarios for the 3% montmorillonite and 4% kaolinite columns, with the only difference being that in the two aforementioned columns more movement of sand grains occurred, and more gas penetrated the sample. At the highest concentration of kaolinite for the column with 6% fines in Figure 5.1.2, a gas driven fracture developed; at increased fines concentration, phenomena like throat clogging causes gas pressure to increase locally mobilizing the grains, the figure shows a noticeable dislocation of the grains opening a main path for the gas to flow. It is noted that because of throat clogging due to fines, there is no percolation of the gas other than the main branch of fracture. Similarly, for Figure 5.1.3 representing the 5% montmorillonite cylinder, fines possibly caused throats to be clogged as gas was not noted to evenly percolate the sample, a major displacement of sand grains after gas injection is noted, opening a main branch for the gas to move.

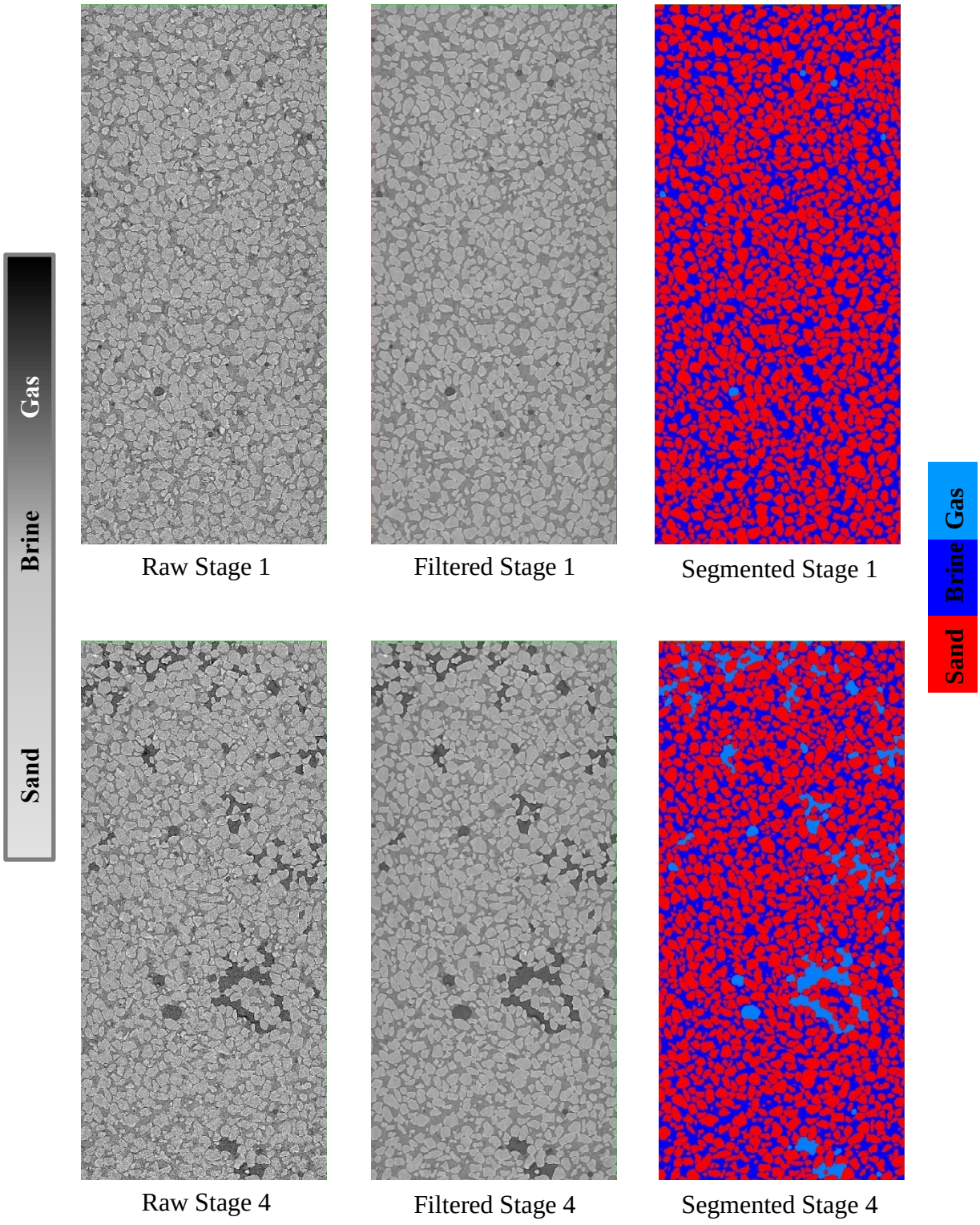

Figure 5.1.1: image analysis for initial and final stages of 2% kaolinite column

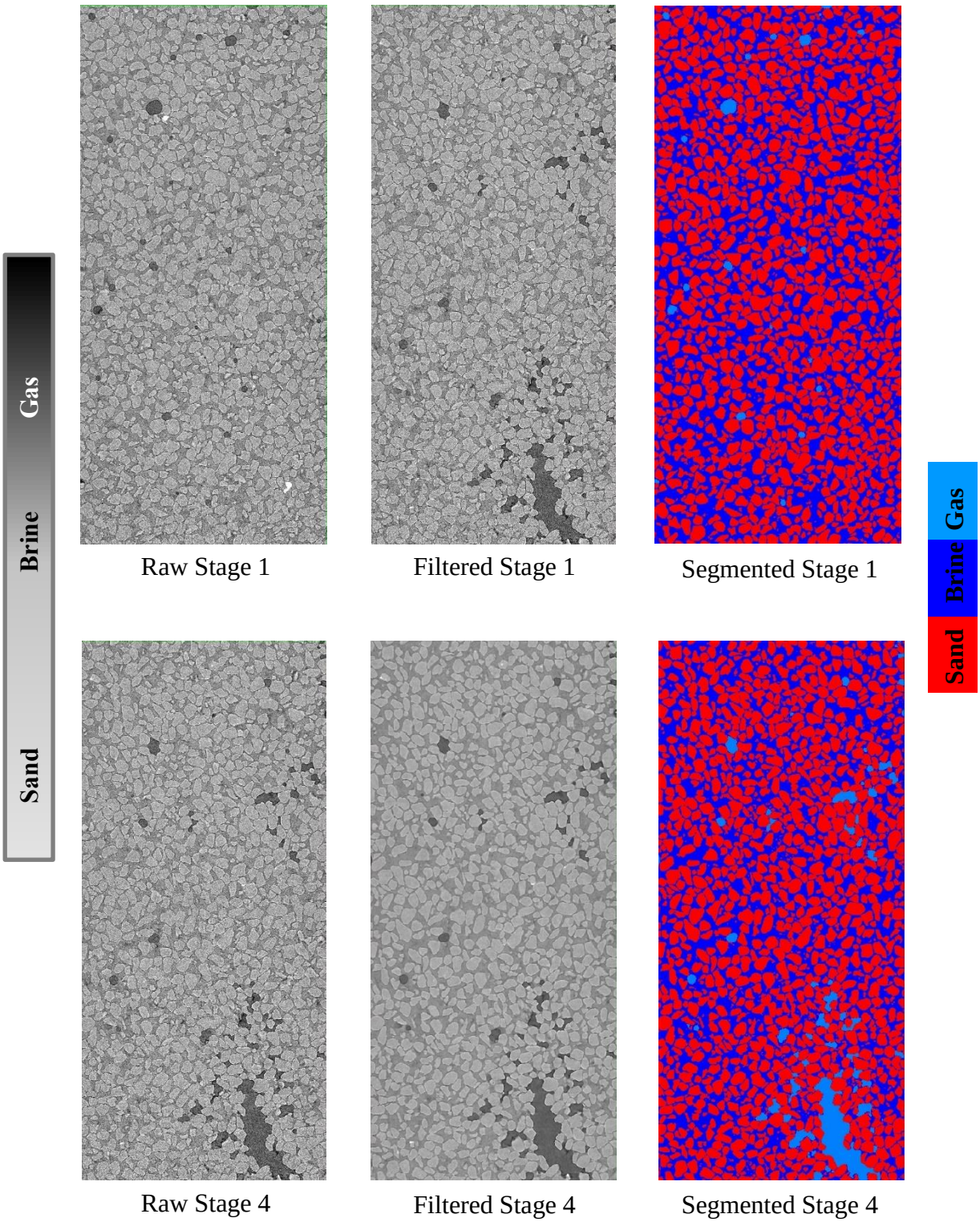

Figure 5.1.2: image analysis for initial and final stages of 6% kaolinite column

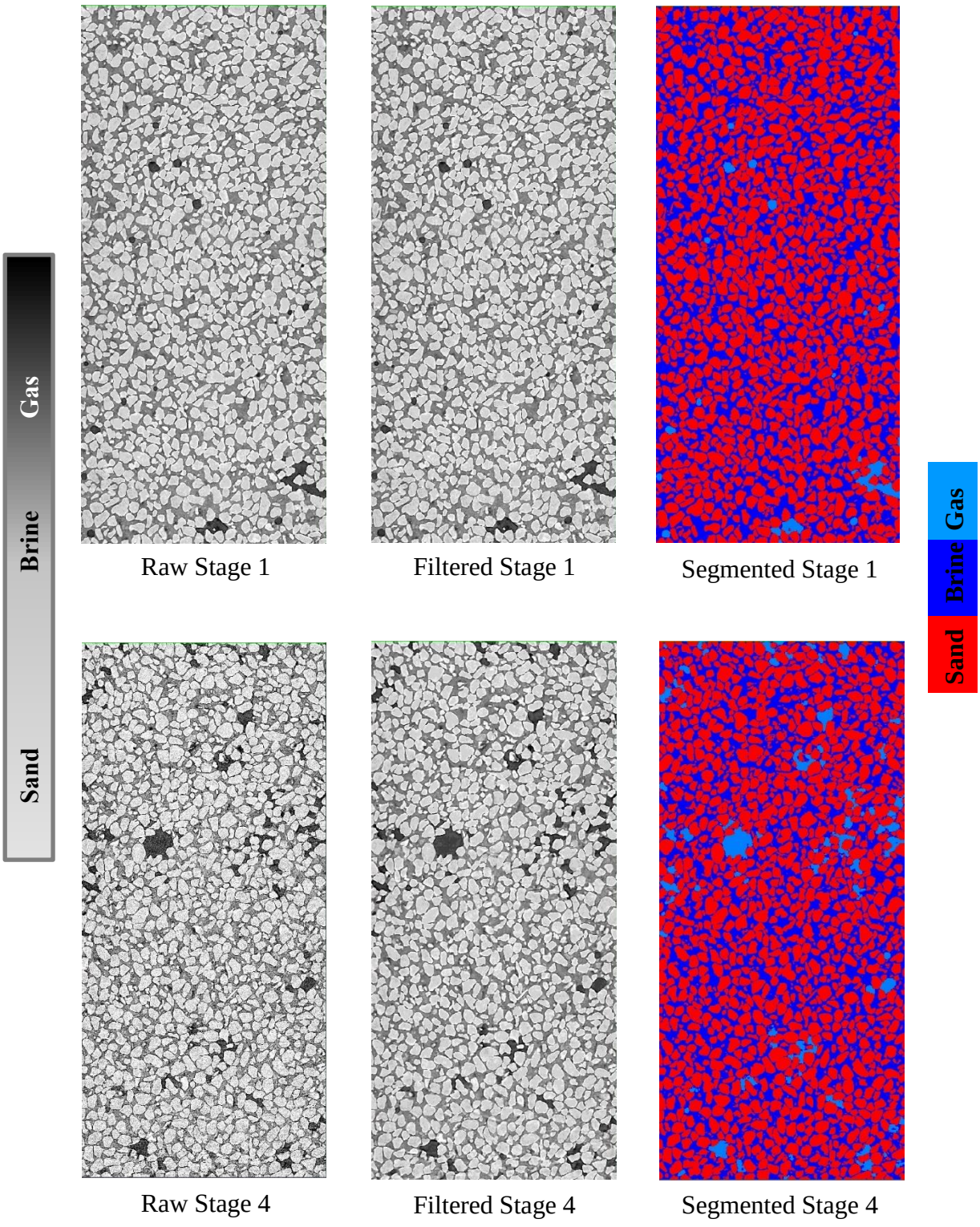

Figure 5.1.3: image analysis for initial and final stages of 5% montmorillonite column

5.2.Volume Fraction

Using the segmented images, the voxels of each binarized phase can be counted and divided over the total size, this gives the volume fraction of a certain phase in the image. The experiment targeted a porosity of 40% (sand fraction of 60%). Table 5.2.1 shows that the targeted porosity was achieved with a margin of ± 3%. The table show the fraction of each phase for all the scanned systems representing the stages of gas injection from 1 to 4 for each percentage of fines. Similarly, Figure 5.2.1 is a visual representation of the volume fractions, showing the water and gas ratios as they change with each step of gas injection.

Table 5.2.1: All Systems Volume Fractions, (K) Kaolinite, (M) Montmorillonite

	Volume Fractions				Volume Fractions		
System	Brine	CO_2	Sand	System	Brine	CO_2	Sand
K2%1	0.400	0.001	0.599	K6%1	0.422	0.006	0.572
K2%2	0.375	0.024	0.601	K6%2	0.393	0.032	0.575
K2%3	0.373	0.026	0.601	K6%3	0.385	0.041	0.574
K2%4	0.363	0.039	0.598	K6%4	0.359	0.064	0.577
K4%1	0.379	0.001	0.620				
K4%2	0.371	0.008	0.621				
K4%3	0.266	0.105	0.629				
K4%4	0.209	0.158	0.633				
M3%1	0.322	0.086	0.592	M5%1	0.394	0.015	0.591
M3%2	0.307	0.100	0.593	M5%2	0.408	0.020	0.572
M3%3	0.279	0.126	0.595	M5%3	0.370	0.036	0.594
M3%4	0.234	0.168	0.598	M5%4	0.360	0.045	0.595

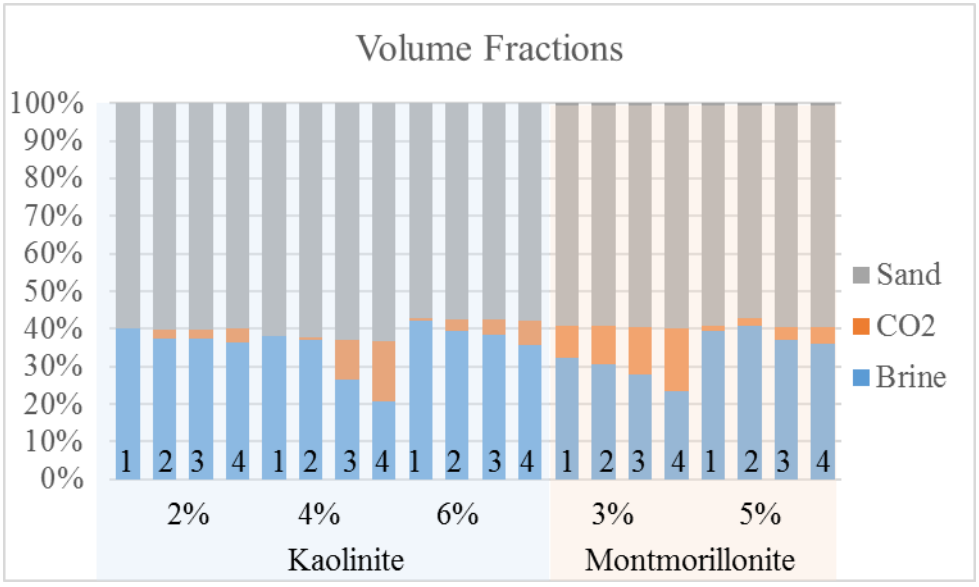

Figure 5.2.1: volume fraction for all cylinders showing gas injection stages

The figure illustrates the increased gas volume for all gas injection stages for each cylinder. It is not the quantity but rather the pattern of gas fraction increase is what gives indications of the phenomenon that happened at varying fines contents. For instance, the 3% montmorillonite column have high fraction of gas that increases gradually with each step, but no major displacement of sand grains developed in the sample, yet for the 5% montmorillonite the first and second stages showed little increase in gas fraction, while a jump is observed in the third stage. This indicated a rapid displacement of the sand grains due to high fines content. The patterns indicate that phenomenon is taking place rather than the quantities, as the scan represents only part of the sample volume.

5.3. Gas Flow Patterns Visualization

Using the segmented images from the 3D micro-computed tomography, each phase can be visualized by using the voxels' location and value. The visualization of gas flow patterns and their change with respect to fines concentrations can be done at a microscopic scale; allowing the observation of gas flow through individual throats of the permeable media. The ability to see gas in three dimensions gives deterministic information about the change in gas flow due to fine particles changing the void space morphology. Figure 5.3.1 shows that the 2% kaolinite column have the least fines concentration. Capillary fingering phenomena is observed at stage 2 in the figure, the CO_2 gas follows paths that percolate through bigger throat sizes with the least capillary resistance; as gas injection progresses in stages 3 and 4, more small paths are filled with gas. It is noted that an individual path is not observed to have major growth in diameter which indicates no major sand grains movement. A visualization of 4% kaolinite column appears in Figure 5.3.2 the second stage shows gas flowing in but with discontinuities in the gas bulbs in the last two stages, the gas filled the scanned section of the column, an evidence of the gas ability to further percolate in the sand without major movements in the sand grains. This was not the case for the column of 6% kaolinite with the highest concentration of fines visualized in Figure 5.3.3. Here CO_2 did not percolate, rather it mobilized the sand grains creating one main branch (fracture) as illustrated in stage 2. As the injection continues in stages 3 and 4, the body of the gas driven fracture increases in size, this is evident that the fines prevented CO_2 from percolating in the sample by blocking small throats.

For the montmorillonite columns, first the 3% cylinder in Figure 5.3.4 shows that the scanned part had more gas injected, nonetheless the aim is to study the pattern not the gas quantity. By viewing the second stage, gas is percolating in a manner similar to the 4% kaolinite, CO_2 is able to percolate without major movements of the sand

grains, forming many small channels as seen in the 3rd and 4th stages. In Figure 5.3.5 the 5% montmorillonite image is displayed for all the stages. Gas is observed to percolate through the pore space in stage 2. Yet upon injecting more gas in stage 3, a major snap off the gas body is observed, indicating a change in the pore space (grains displacement). The body of gas is shown to stay discontinued even when increasing the pressure at stage 4, the gas body increased in size visually indicating the movement of sand grain.

Both the columns with highest fines content 6% kaolinite and 5% montmorillonite showed high mobilization of sand, but with major differences in the flow patterns. The kaolinite had one major bath (a fracture) while the montmorillonite flooded few major paths which had wider diameters. This is expected as kaolinite is hydrophobic while montmorillonite is hydrophilic, where the last accumulate on the gas brine interface (Jung et al., 2018b). Having higher concentration of fine particles at the brine-gas interface may induce ganglia snap off, hence explaining the behavior at 5% Montmorillonite cylinder.

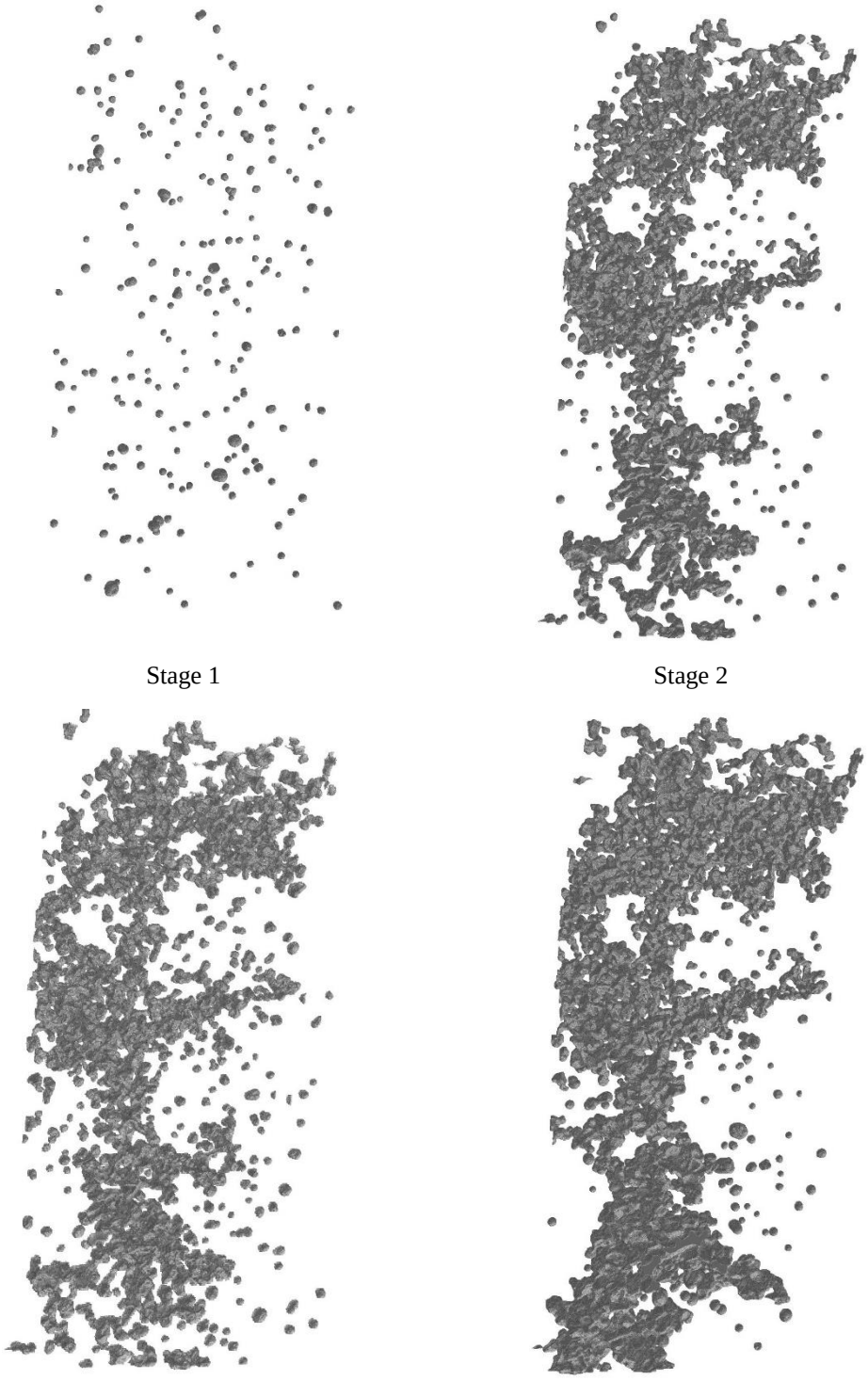

Figure 5.3.1: 3D visualization of segmented gas phase for all injection stages of 2% kaolinite column

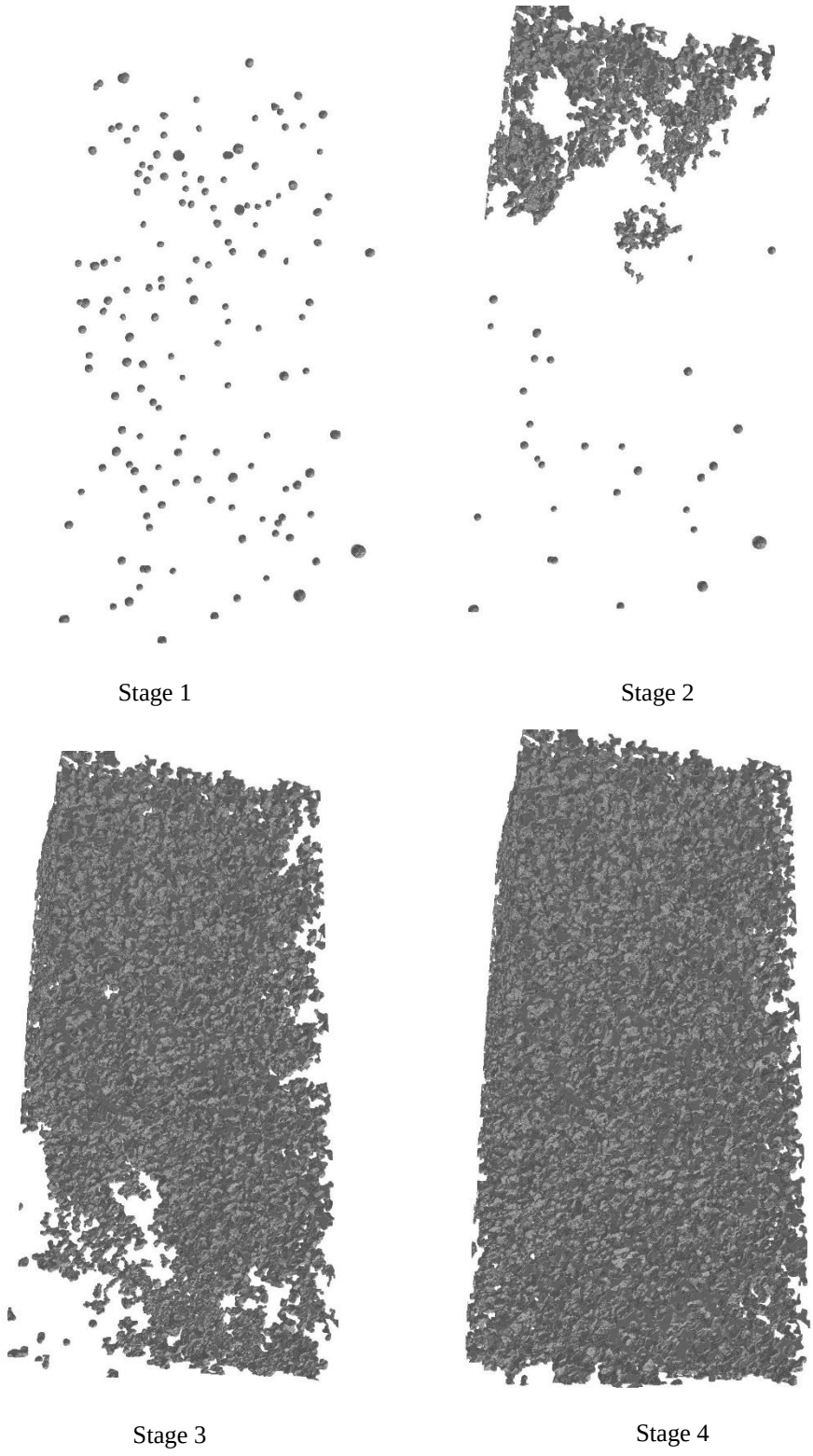

Figure 5.3.2: 3D visualization of segmented gas phase for all injection stages of 4% kaolinite column

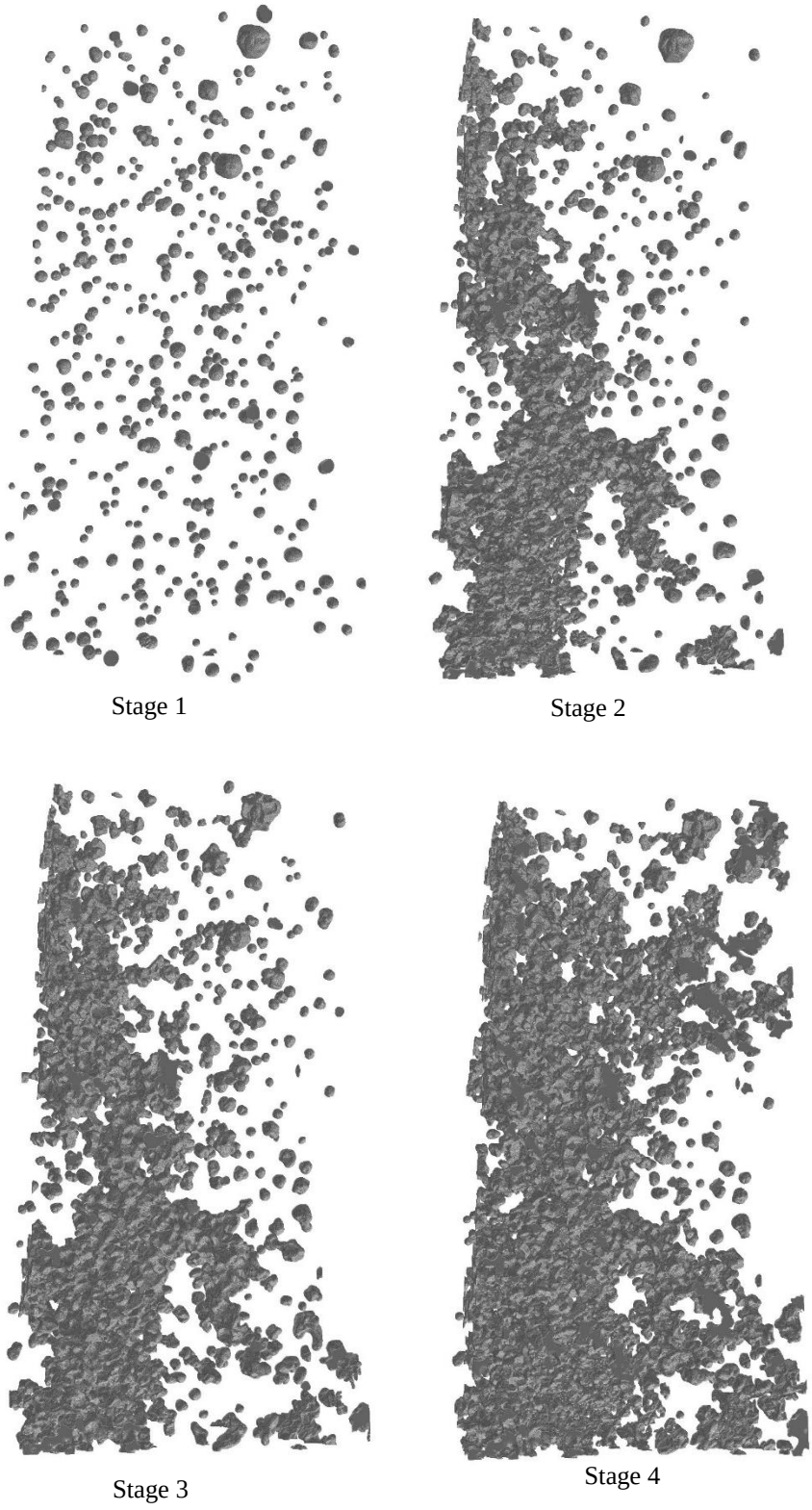

Figure 5.3.3: 3D Visualization of Segmented Gas Phase for All Injection Stages of 6% Kaolinite Column

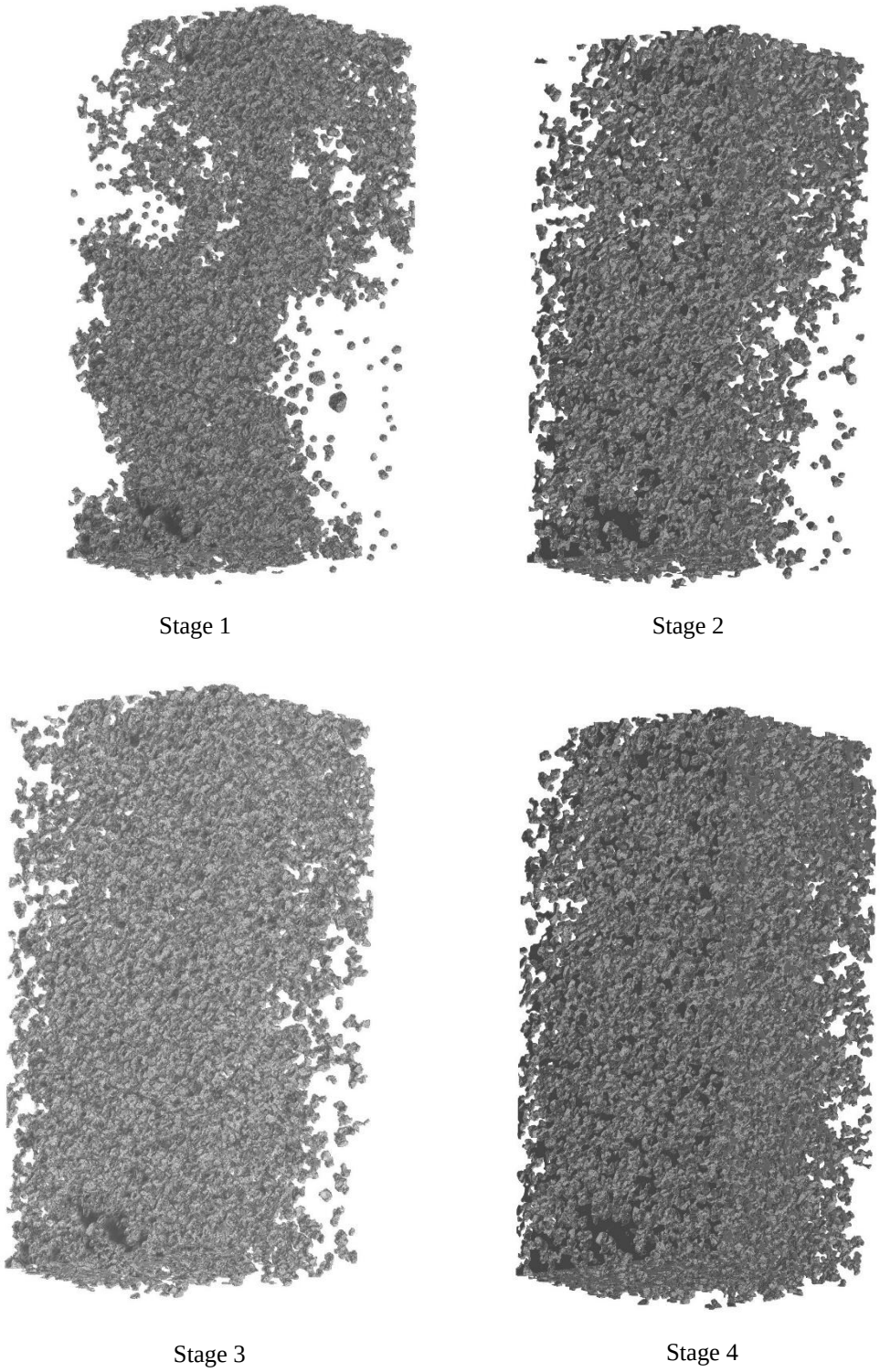

Figure 5.3.4: 3D visualization of segmented gas phase for all injection stages of 3% montmorillonite column

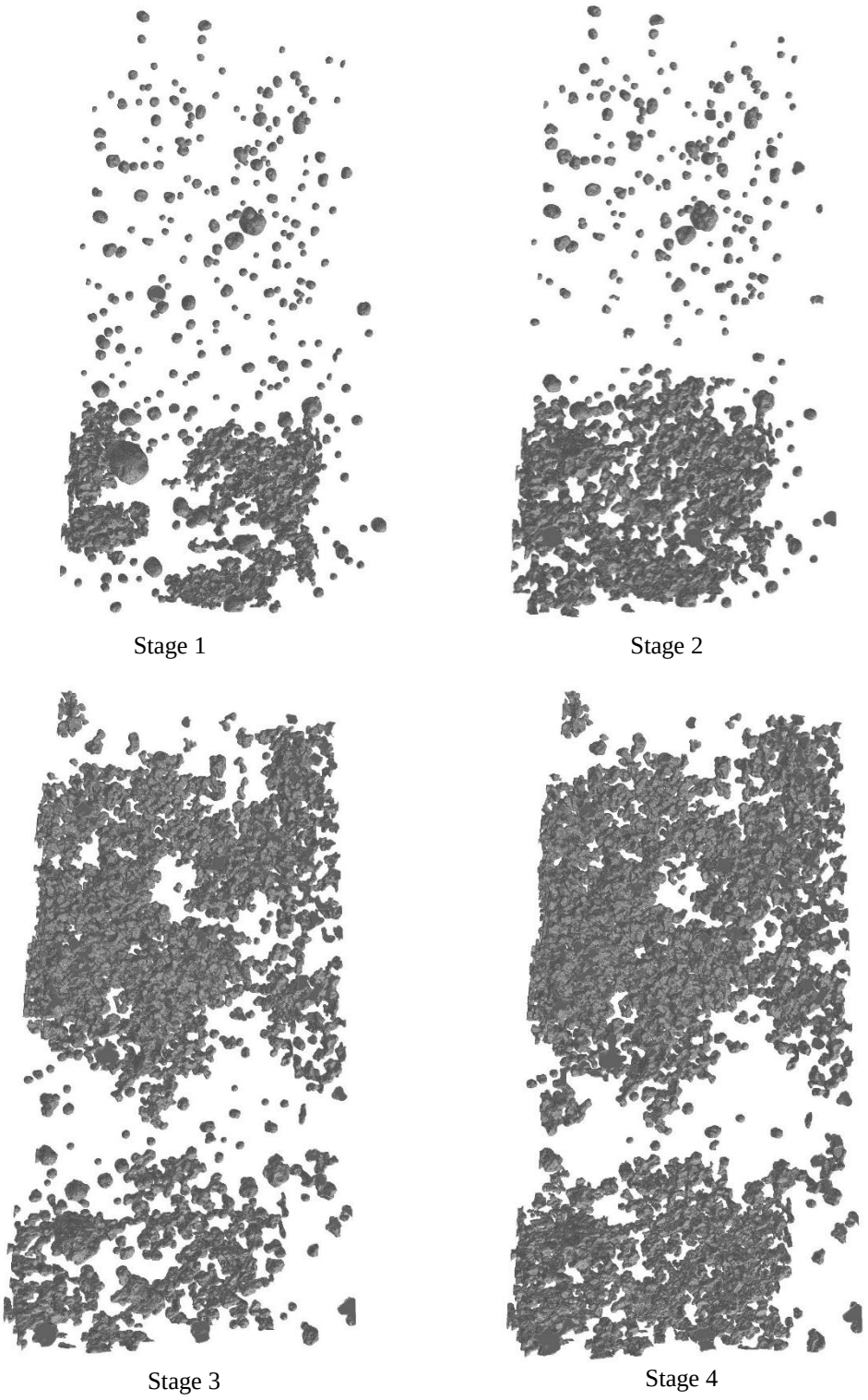

Figure 5.3.5: 3D visualization of segmented gas phase for all injection stages of 5% montmorillonite column

5.4. Pore Networks Statistics

For each of the segmented images a pore network was generated to simplify the geometrically complex pore space. The brine and gas are considered as pore spaces while the sand was not. Having a pore network generated for every column four times at each gas injection stage helps in quantifying the change that the gas flow caused to the unconsolidated pore space, at different fines concentrations. Twenty pore networks were generated at full image size of 1080x1080x2356 voxels (2748 Million voxels). The size of one scanned raw image is 32 GB, segmented results are 6 GB per image, using the pore network to simplify the pore space results in 50 MB per image (≈ 0.050 GB), at a scale 120 times smaller than a segmented image in file size. The generated pore network benefits from accelerating computation for the reminder of the analysis. Most importantly, the resulted statistics aid the understanding of the pore space, and the impact of fines on two-phase flow.

First a summary of the results showing averaged statistics of each system will illustrate the effect of fines on different columns as gas is injected, then representative full distributions of different pores and throats are displayed. Figure 5.4.1 displays in (a) the total number of generated pores to represent the void space of each system, hereafter the systems are organized by the gas injection stages from 1 to 4 and are ordered as K2%, K4% and K6% with (K) stands for kaolinite, while M3% and M5% with (M) for the montmorillonite columns, (b) Displays the total number of throats per system. In both of pores and throats counts, the behavior is similar, the K4% and M3% show a gradual increase in the count, while K6% and M5% show a rapid increase then a drop followed by gradual increase. This can be related to rapid movements of sand grains that divide the pore and throats, thus increasing their count. It is noted in most of the systems that as gas flows, it increases the number of both pores and throats.

Figure 5.4.2 displays a pattern for both throats radii and lengths, in (a) and (b) respectively; it is noted that at low to middle fines concentration the averaged dimensions of the throats gradually decrease. While in the columns with high fines concentration, a rapid drop in the throats dimensions is observed at the first gas injection in stage 2, then a rapid increase with more gas entering the system in stage 3. This is followed by a gradual drop when increasing the gas pressure at the last stage. This is compatible with the result for the averaged inscribed pore radii in (a) at Figure 5.4.3, which shows the exact patterns. Having multiple columns confirms this unique pattern due to fines, which is observed for the first time and of considerable scientific value. In the same figure at (b), the coordination number which describes the number of throats connected to a pore had an averaged value of about 6 over the 5 columns. There is no major relation observed for the change of averaged coordination number with injecting gas at different fines concentration, which may be due to the huge number of pores in the system.

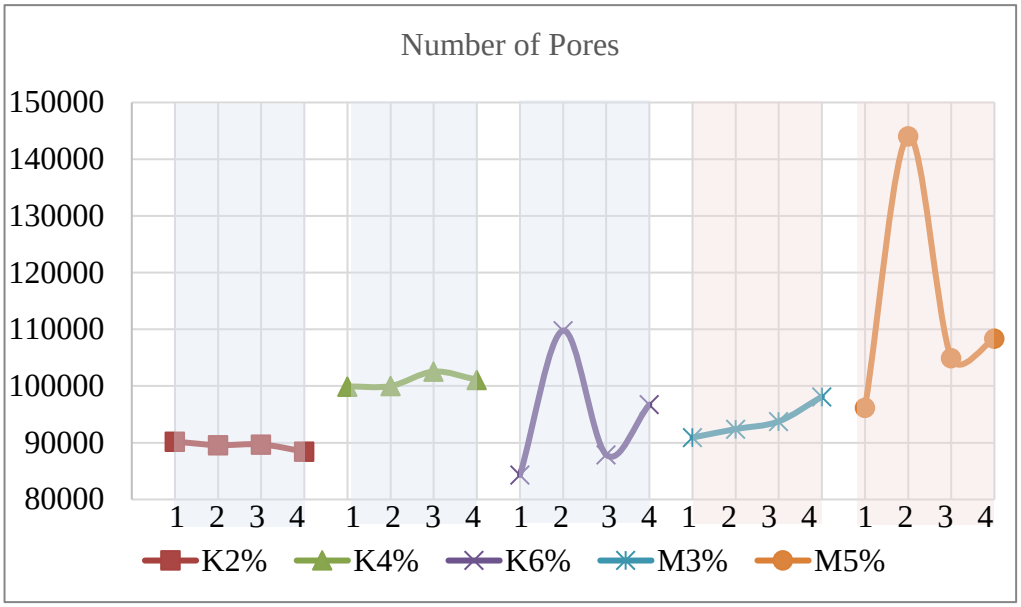

(a)

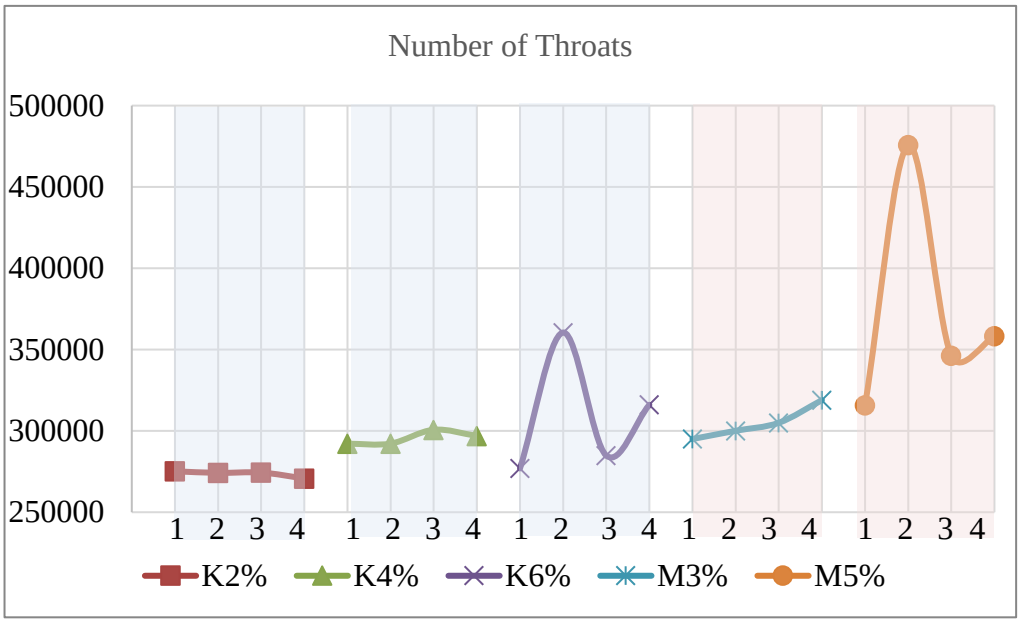

(b)

Figure 5.4.1: pores and throats numbers for every system

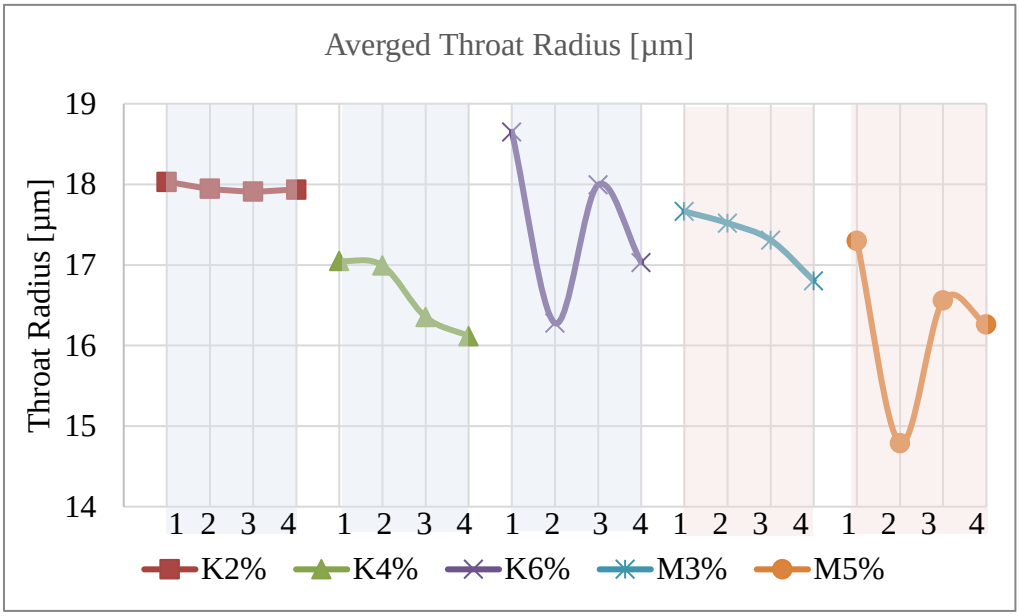

(a)

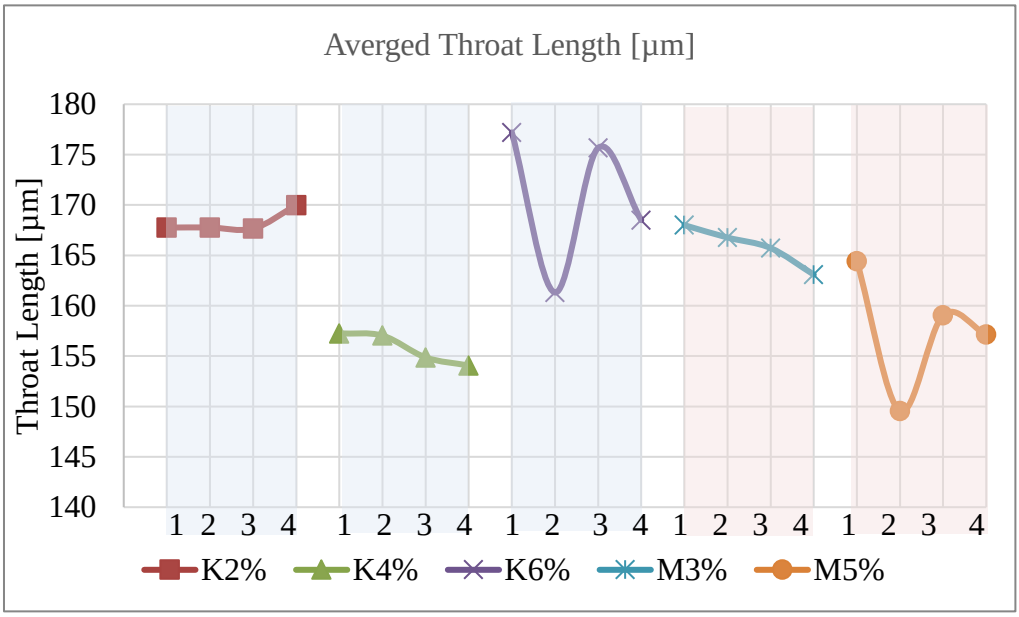

(b)

Figure 5.4.2: averaged throat radius (a) and length (b) for every system

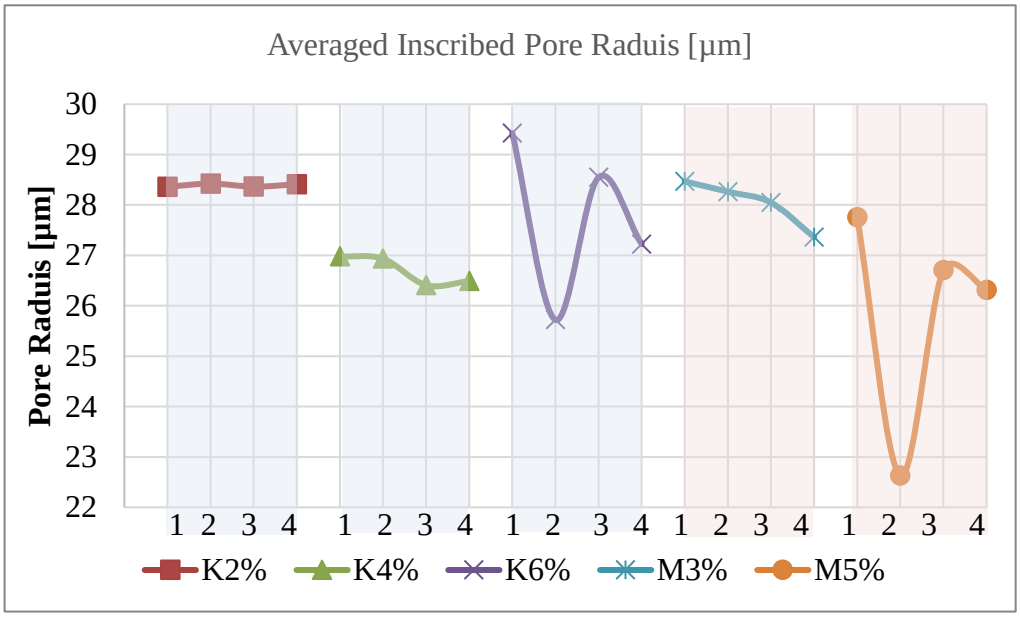

(a)

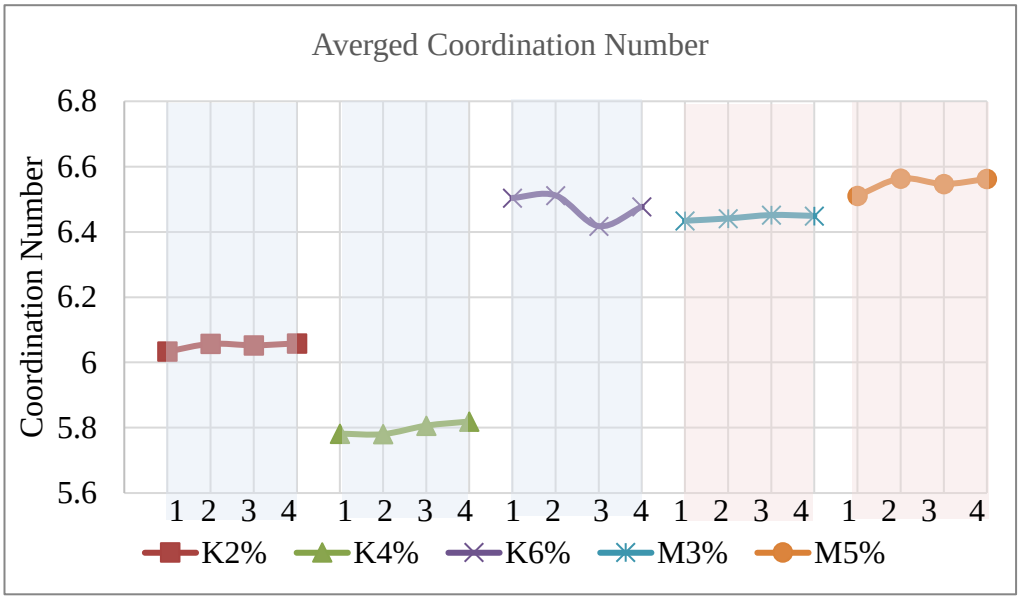

(b)

Figure 5.4.3: averaged pore radius (a) and coordination number (b) for every system

Understanding the distribution of the pore space statistics gives more insight about the pore space and the impact of other parameters on it. Previously it was documented that the averaged coordination number was around 6. Examining the distribution illustrated in Figure 5.4.4 proves that the most dominant coordination number is 4 and 5 for all the columns, it also shows how the pore count increases with the increase of fines in kaolinite 2%,4% and 6%, and likewise for montmorillonite 3% and 5%. This is an indication of the importance of the distributions of the pore space statistics. The aforementioned figure showed all columns at the final stage of gas injection.

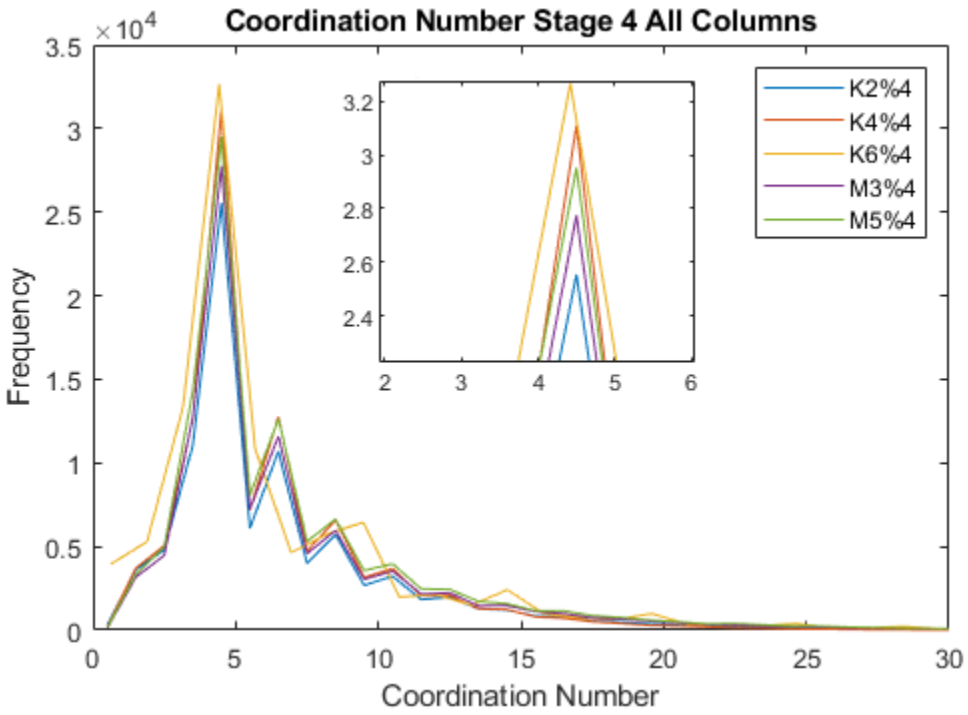

Figure 5.4.4: final stage coordination number for all columns

Figure 5.4.5 presents a zoomed part of the pores volume distribution for all the columns at stage 3, it is noted that increasing the fines content results in higher numbers of smaller pores, with the results being consistent for all the columns. This might be due to gas moving the grains, which produces few wide paths but results in smaller voids for the remainder of the system.

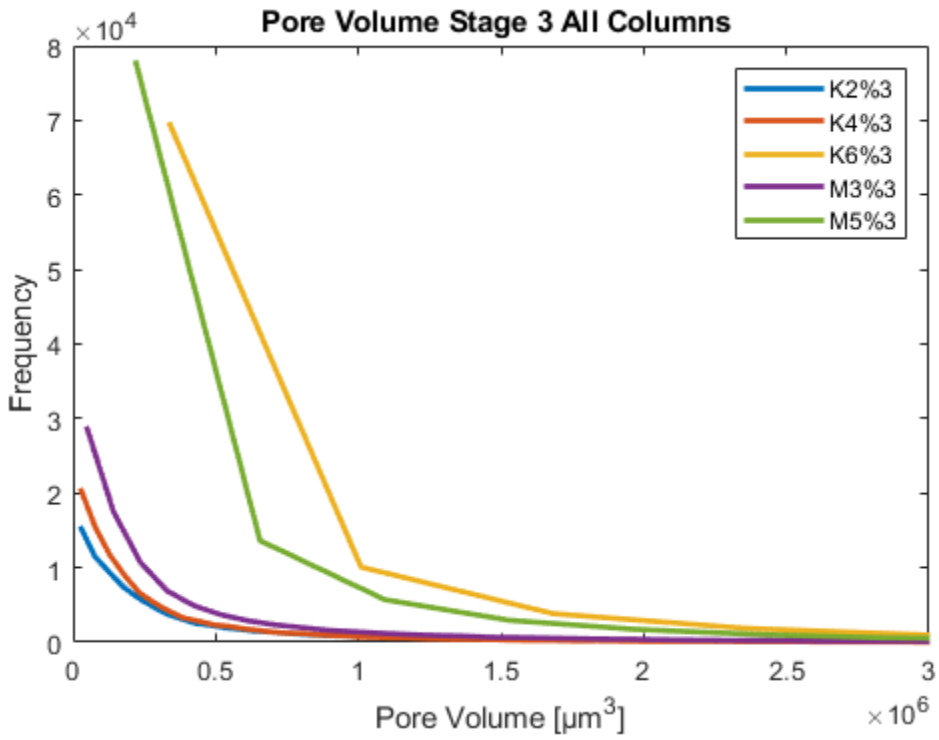

Figure 5.4.5: the distribution of pore volume for all fines concentrations at stage 3 of CO_2 injection

Figure 5.4.6 in (a) demonstrates a complex effect of fines and multi-phase flow on the pore morphology (sediment structure), it shows that at the column of 4% kaolinite, the inscribed pores radius and pores count decrease with the increased injection of CO_2. The added scientific value of using this distribution is embodied in the quantification of such pattern; on the 4% kaolinite, the mode of pore radius dropped

from 28 microns at the initial stage to 25 microns at the final step with the pore counts decreasing from 4000 to 3750 pores.

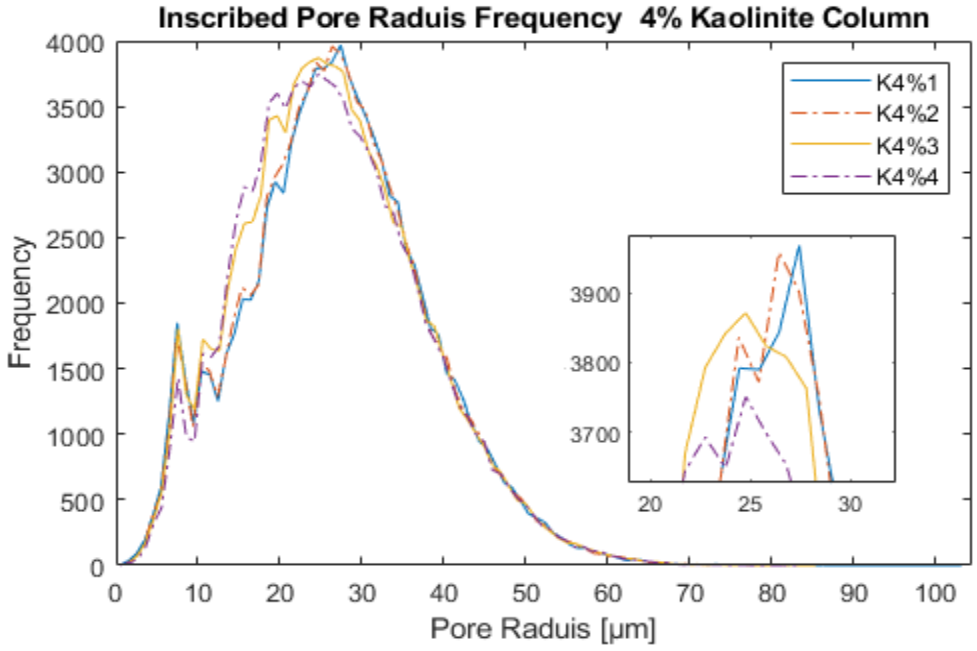

(a)

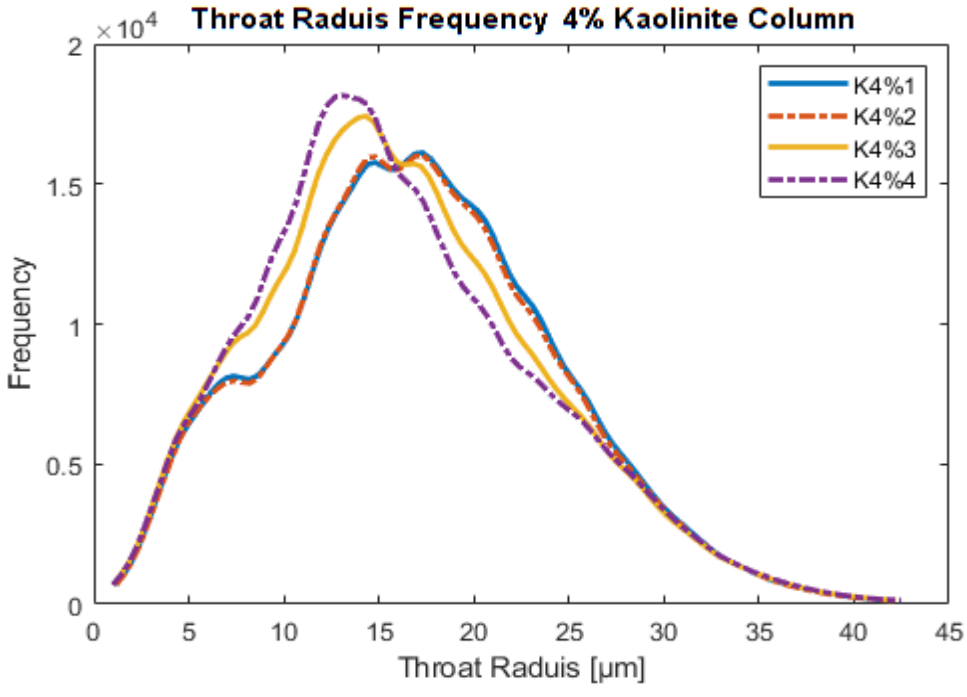

(b)

Figure 5.4.6: distributions of (a) pore radius, (b) throat raduis, for 4% kaolinite column at all CO_2 injection stages

Correspondingly, Figure 5.4.6 (b) shows the distribution of throats radii for the same column. As more gas is injected, the most frequent radius size dropped from 17 microns to 13 microns, with the count increasing from 16 thousand to 18 thousand throats. This indicates that throats contracted and were divided due to the change in the void's morphology from gas injection. Finally Figure 5.4.7 quantifies the change in throats length for all columns due to altering fines concentration. The results are displayed for the 3rd stage of gas injection; it is obvious that increasing the fines concentrations increased the throats count, reportedly increasing the fines decreased the throats lengths.

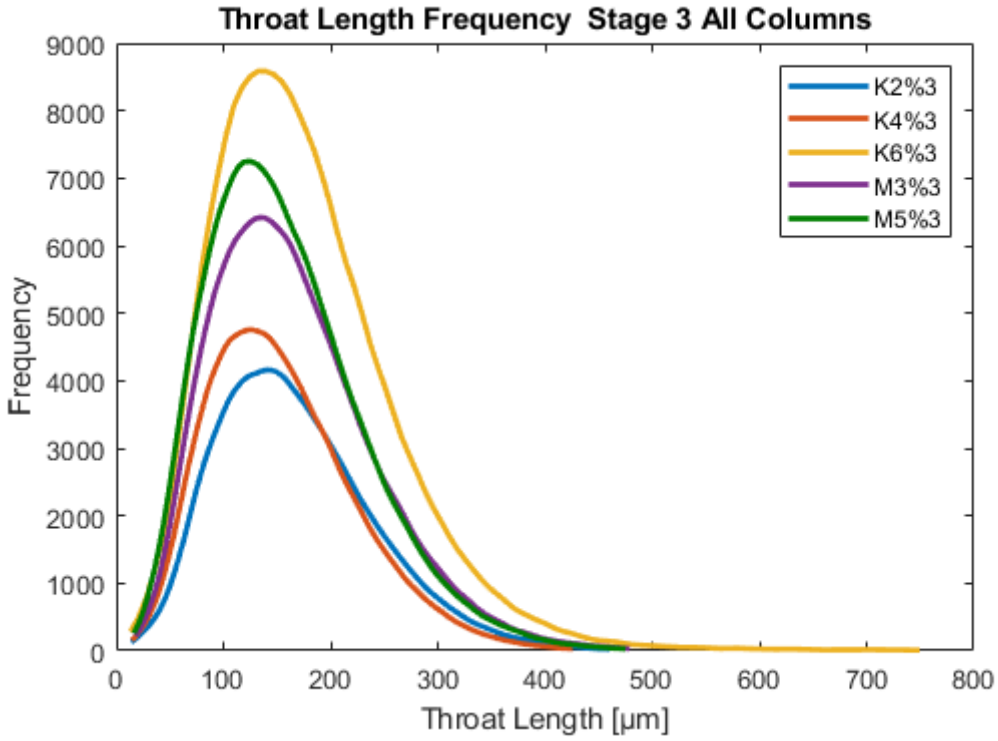

Figure 5.4.7: the distribution of throat lengths for all fines concentrations at stage 3 of CO_2 injection

5.5 Two Phase Fluids Flow

The simulations for the two-phase flow experiments utilized the generated pore networks. Primary drainage and water flooding experiments were used to generate relative permeability and capillary pressure curves for each of the 20 systems, resulting in 120 curves, each made of 40 simulation points. The results show in a quantitative manner, the impact of the different parameters on the two-phase flow through the unconsolidated porous media. Twenty curves for relative permeability of water krw; 20 curves for relative permeability of gas krg and 20 capillary pressure Pc curves were generated once for the primary drainage, then another time for water flooding. Moreover, porosity, permeability and maximum capillary pressure were calculated for each system.

Knowing that porosity and permeability are critical factors in determining two phase flows, their results are first shown along with the maximum capillary pressure in each system, then the results for the two-phase flow experiments are presented. Porosity for every system is displayed in Figure 5.5.1, the figure illustrates the porosity with respect to gas stages and fines content and type. With the exception of few cases, a trend is noted when CO_2 gas is injected, the porosity decreases. Consequently Figure 5.5.2, shows that permeability decreases as more gas enters the systems. This is excluding the 6% kaolinite (with the highest fines content), where a fracture developed, thus as more gas is injected, the fracture body grows, thus increasing the permeability. The values of permeability are an indication of the accuracy of the used algorithm as sand have a permeability ranging between 1 μD to 100D, (Bloomfield, 1995). Maximum capillary pressure of each system is showen in Figure 5.5.3, 2% and 4% kaolinite show a gradual increase with gas injection, while the rest of the systems show a common pattern of rapid increase in capillary pressure at stage 2 where gas is first injected, then a steady drop as the stages develop.

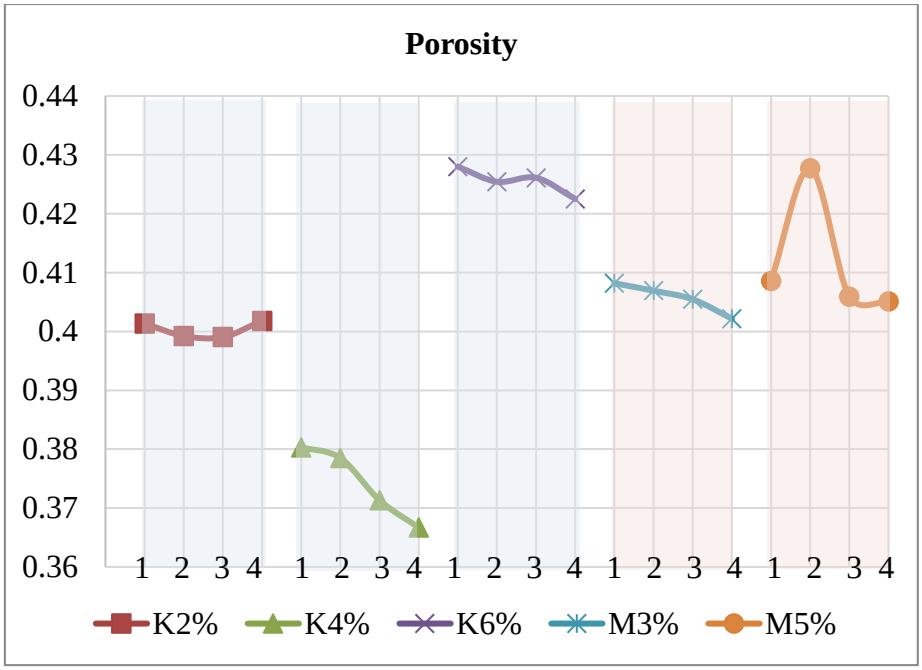

Figure 5.5.1: porosity for all systems showing effect of gas injection on pore morphology when changing fines type and quantity

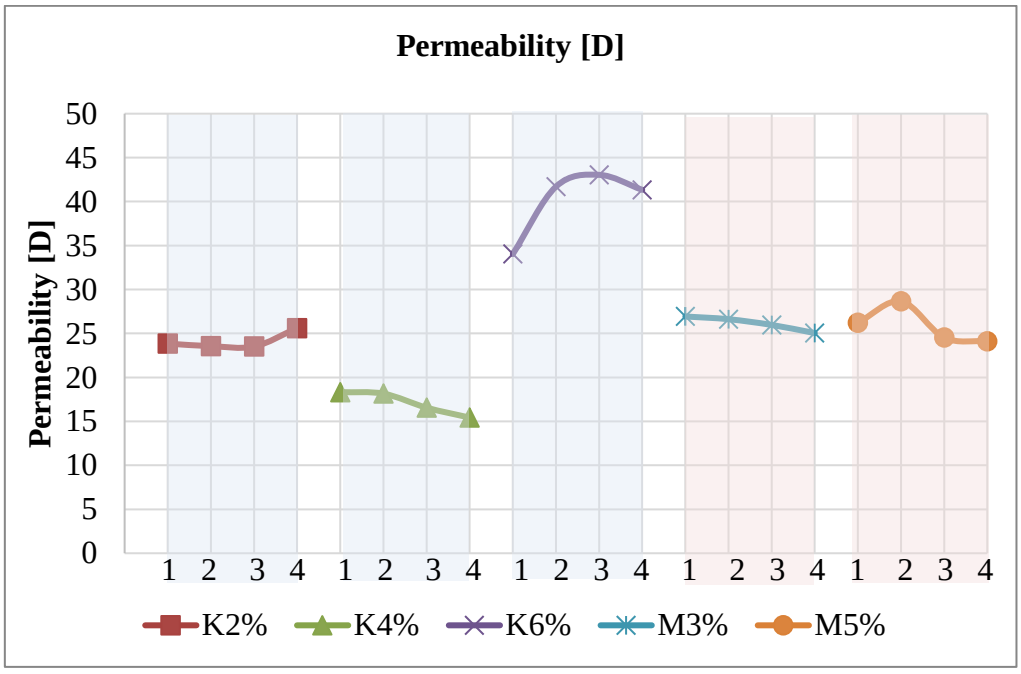

Figure 5.5.2: permability for all systems showing effect of gas injection on pore morphology when changing fines type and quantity

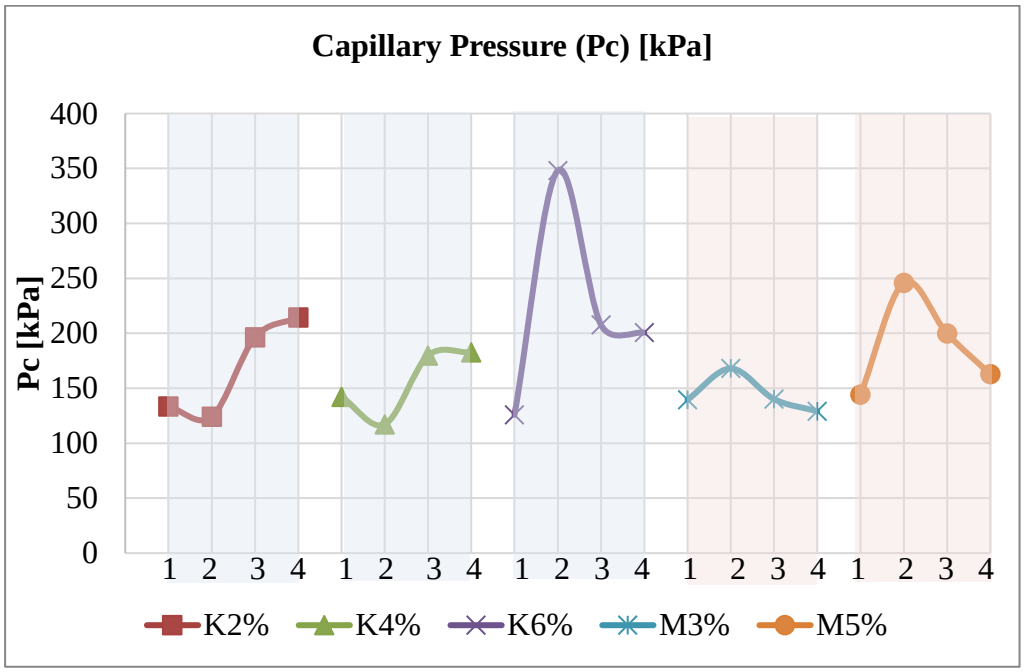

Figure 5.5.3: maximum capillary pressure for all systems showing the effect of gas injection on pore pressure when changing fines type and quantity

Representative results of selected graphs are illustrated, showing the impact of fines on two-phase flow. Figure 5.5.4 shows all the columns at the final state, considering the value of 0.8 water saturation (S_w) it can be seen that water relative permeability is higher by 10% when increasing kaolinite from 2% to 4% or 6%. Similarly for montmorillonite it is higher by 5% when increasing the fines content from 3% to 5%, this increase in water relative permeability (krw) may indicate a drop in gas relative permeability due to increased fines content. Figure 5.5.5 illustrates a single column for the 6% kaolinite with all its gas injection stages, considering 0.9 S_w the relative permeability of water dropped by 20% due to the developed fracture when gas was injected in the experiment at APS. This indicates an increased gas permeability caused by the fracture changing the morphology of the void space. Figure 5.5.6 shows the montmorillonite 5% column, at 0.9 S_w an increase is observed for krw by 25% from

the initial state to the first gas injection. This agrees with the increased relative permeability of gas (krg) at S_w,=0.1(correspond for S_w=0.9 for krw), additionally at 0.5 S_w the krg can be seen to increase as the stages develop from 1 to 4.

Figure 5.5.7 shows water flooding of all the columns at the stage where gas is firstly injected. Increasing the fines content resulted in increased krg as revealed in (a), while (b) compliments this result by showing that it reduces krw at water flooding for both the types of fines studied. Figure 5.5.8 shows capillary pressure curves at stage 3 for all the columns. The curves express how the content increase of any fines type resulted in increased capillary pressure for all the cases excluding the 6% kaolinite column due to the developed fracture. In Figure 5.5.9 for the 4% kaolinite column, as gas injection stages develop from 1 to 4, the krw increase by 5% while the krg decreased, indicating that as more gas flow in the unconsolidated media, the krg is reduced for water flooding experiments.

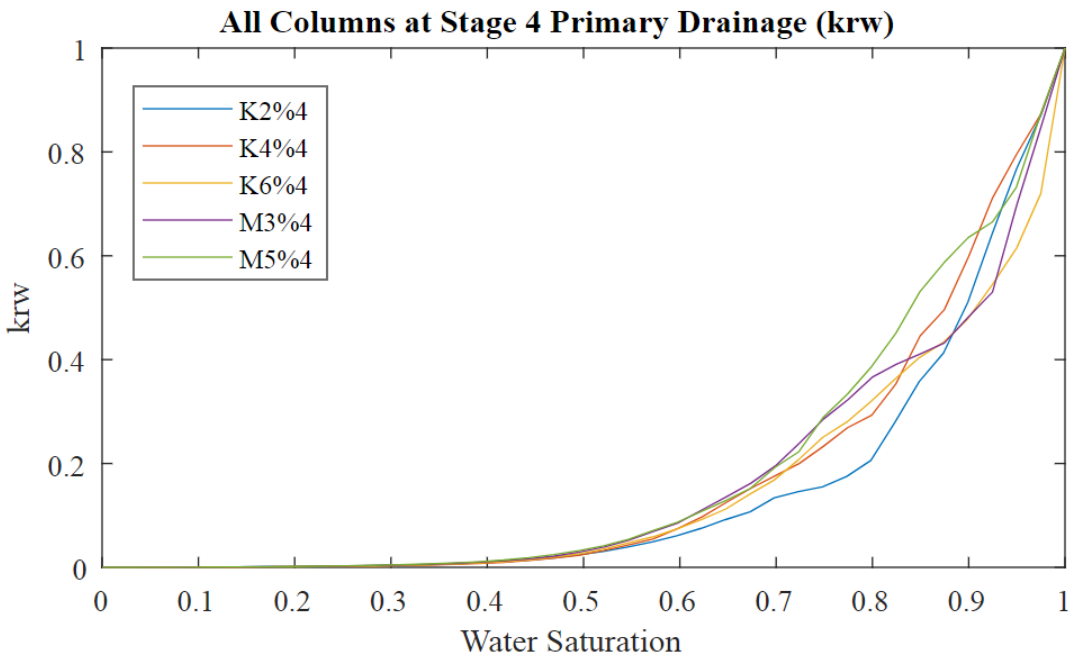

Figure 5.5.4: water relative permeability krw, all fines concentrations at final stage of CO_2 injection

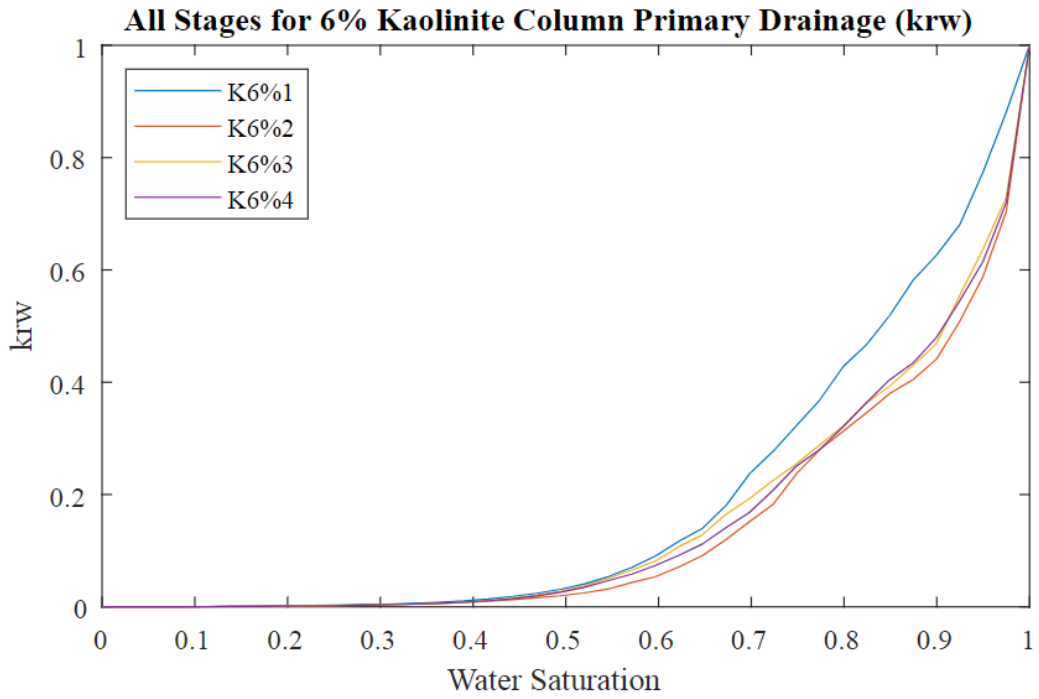

Figure 5.5.6: krw curves for all stages of CO_2 injection at 6% kaolinite column

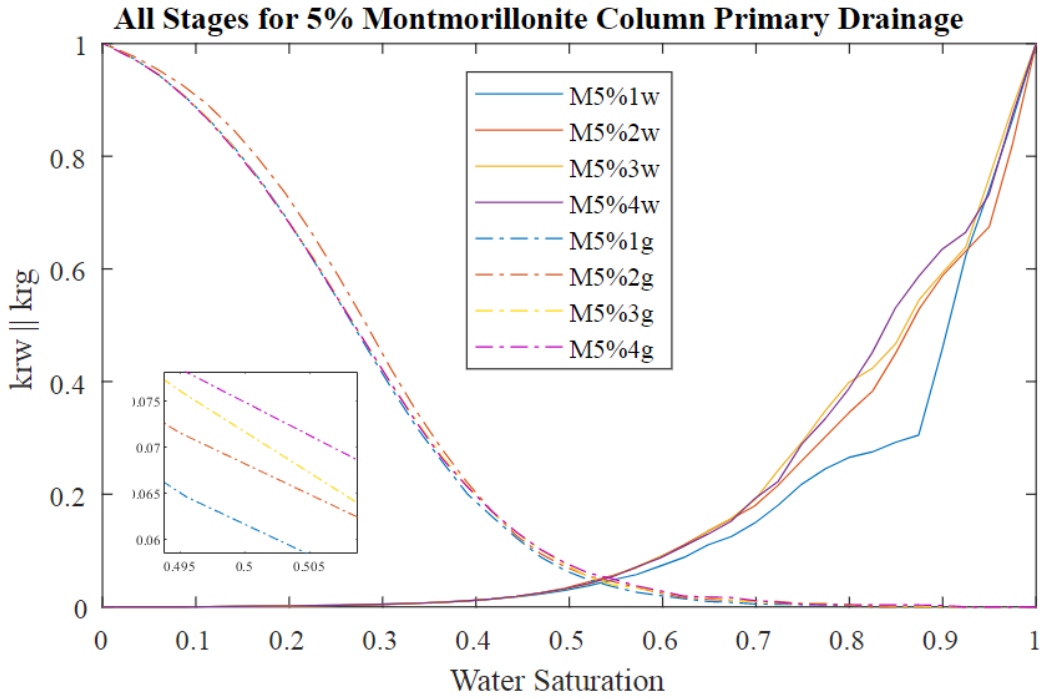

Figure 5.5.5: relative permeability of water krw and gas krg, for all CO_2 stages at 5% montmorillonite column

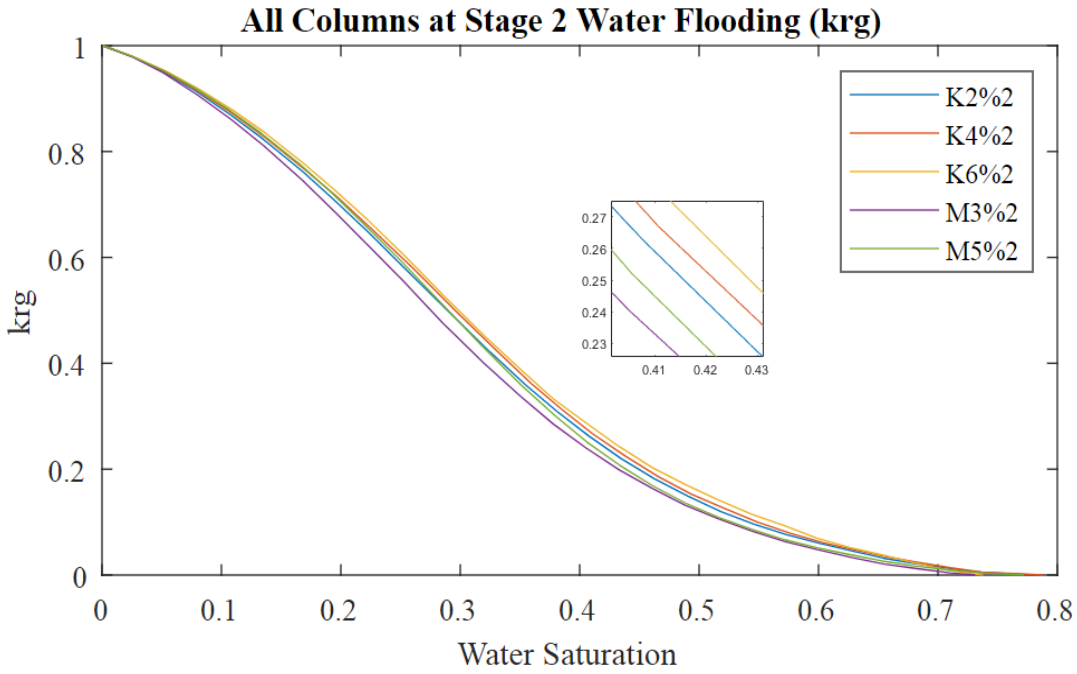

(a)

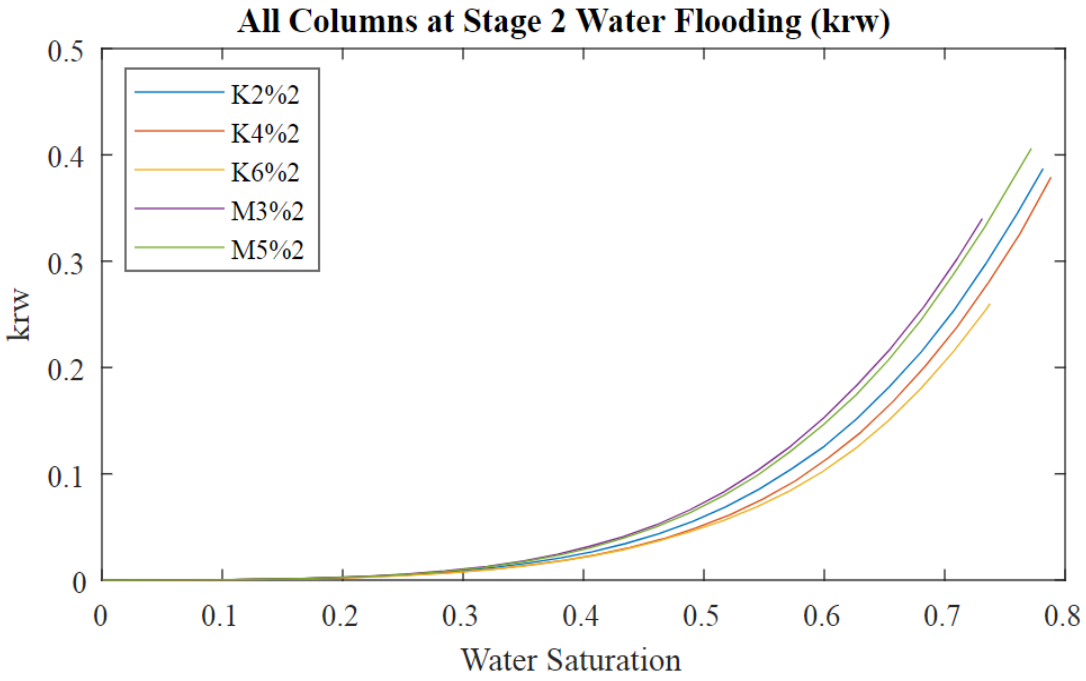

(b)

Figure 5.5.7: krg at (a) and krw at (b) for all columns at stage 2 of CO_2 injection

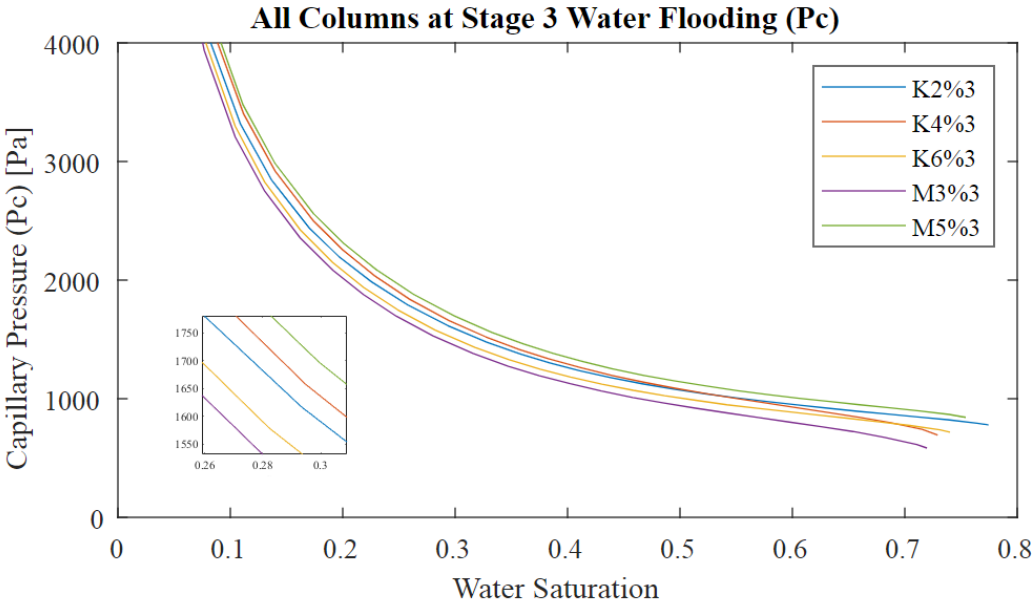

Figure 5.5.8: capillary pressure Pc curves for all columns at stage 3 of CO_2 injection

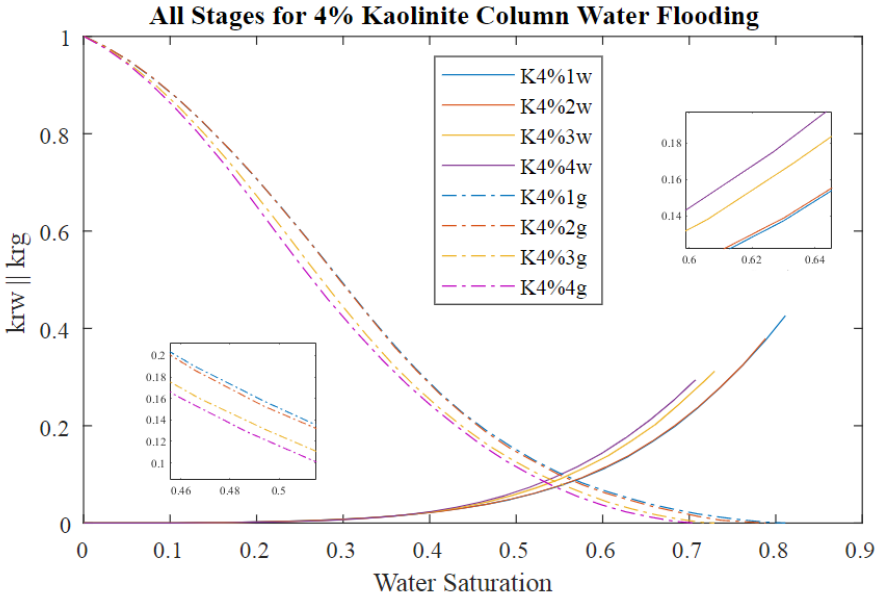

Figure 5.5.9: krw and krg curves for all co_2 stages at 4% kaolinite column

CHAPTER 6. Discussion and Conclusions

6.1. Review

Understanding the fluid physics of fines migration in porous media due to multiphase flow, is a complex longstanding problem in many applications including underground water storage, irrigation, oil and gas recovery, contaminates transport. (Rodriguez-Pin, 2010) studied flow and retention of both micro and nano fine particles in glass beads, followed by (Yu et al., 2015) who studied fines dispersion in 12 sedimentary rock cores. (Khan, 2016: Khan et al., 2017;) linked micro computed tomography images to flooding experiments of fines retention in glass beads. Utilizing pore networks and water flooding experiments to quantify the impact of fines and predict permeability. While recently (Gyeol Han et al., 2018) used CT scans at 107 μm resolution to study fines migration due to depressurizing hydrates in sandy sediments . Given that flow phenomenon are controlled by transport at pore-scale, this work arguably for the first time, study the effect of different fines types and contents on real sand packs imaged using μ-CT from synchrotron radiation, imaging the gas flow as it progresses through sediments. High brilliance synchrotron X-ray microcomputed tomography was used, allowing fast reconstruction of the spatial information which is an advancement over other scanning methods. This technique was used to image live experiments of CO_2 gas flow in unconsolidated fully saturated sand column with different fine particles content (Jarrar et al., 2018).

6.2. Experimental setup

Five columns of packed silica sand with 2%,4,6% of kaolinite and 3%,5% montmorillonite as weight of sand were fully saturated. The saturating brine is deionized water with 2% potassium iodide by weight of water. Acrylic cylinders 9.52

mm in internal diameter and 50.80 mm in height were filled with silica sand sieved between 250 μm and 210 μm. The sand was mixed with hydrophobic and hydrophilic fines, kaolinite and montmorillonite respectively, then packed in 5 layers while brine was added during packing. Each column is initial fully saturated, then CO_2 gas was injected from the bottom of the cylinders with 0.4 ml then another 0.6 ml both at a pressure of 27.6 kPa while ejecting water from the top. Finally, CO_2 injection pressure was increased to 41.4 kPa without ejecting water.

6.3. Scanning

The experiments were conducted while scanning the sample at Beamline 13D in APS ANL. High brilliance synchrotron X-Ray micro-computed tomography was used to capture the experiments as it progressed. Scans where taken 4 times for each column as CO_2 was injected. The injection stopes and the system is imaged at quasi-static state each time, imaging takes 30 min; 20 scans are used for analysis. The scanned sections are 1080x1080x2356 representing 4.2x4.2x9.2 mm^3 at a voxel resolution of 3.89 μm3. This eliminates the boundary condition and gives results that represent actual marine conditions.

6.4. Image Filtration and Segmentation

Images were reconstructed using reverse radon transformation creating 3D intensity images, then were filtered by Anisotropic Diffusion followed by a Median filter. Segmentation was done by manually, assigning intensity values to specific phases, then using morphological operations to remove any artifacts ensuring the best results. Sand, brine and gas were segmented while suspended fines were assigned as brine. The used method was successful in representing the finest details. Quantity and location information of each phase were used to show that increased fines content

reduces the porosity due to gas injection by dislocating sand grains as in Figure 6.4.1.

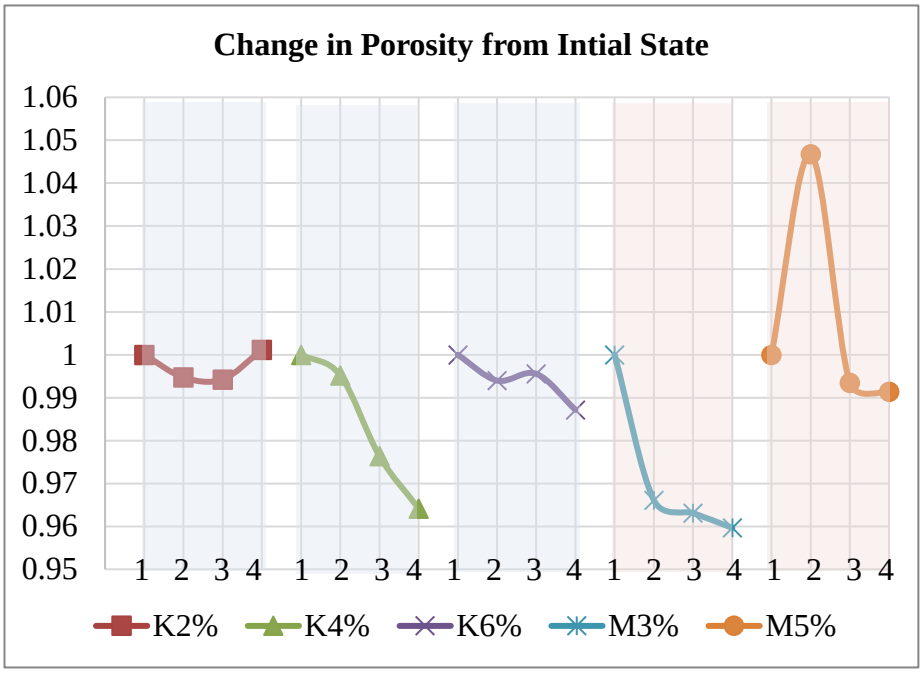

Figure 6.4.1: porosity change for each system based on initial state

Sequentially due to fines migration, gas driven fracture was observed at the highest fines content of 6% kaolinite; complemented with increased sand grains dislocations at increased fines content at 5% montmorillonite. This is due to fines clogging at throats of the permeable media, which when injecting gas results in stresses high to the degree it displaces the grains of an unconsolidated porous media. All the analysis was carried on using Pergeos software and its implemented algorithms.

6.5. Pore Networks

Grain passed pore network model was used, brine and gas were assigned as void space, results accuracy where validated visually and statistically. A pore network was generated for each system to simplify the geometry of the porous media as it changes during the experiment. The sand grains movement due to gas injection and fines clogging at throats, were quantified by comparing the generated pore networks

statistics. Because of fines, when gas flows it reduces pores and throats radii (a seen in (a) Figure 6.5.1) and throats lengths by dividing them; which increases the coordination number, pore and throats counts (as seen in (b) Figure 6.5.1). This effect was shown to be proportional with the fines content and is consistent with fractures formation.

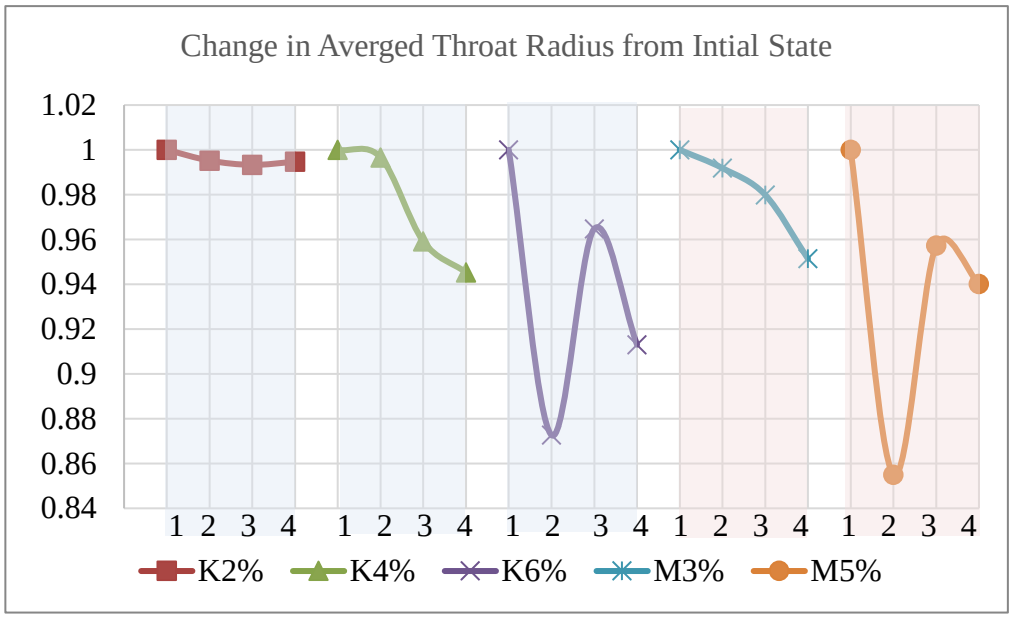

(a)

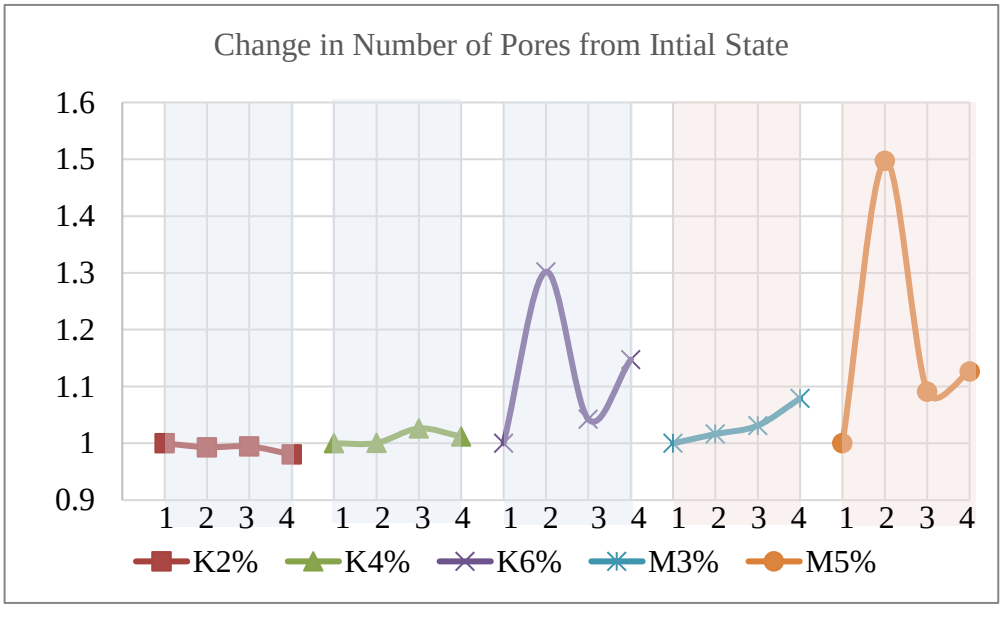

(b)

Figure 6.5.1: change in averaged throat radius (a) and pores number (b) for each system

6.6. Two Phase Flow

120 curves were generated from the primary drainage and secondary water flooding two-phase flow experiments simulations, in addition to the measurements of porosity, permeability and maximum capillary pressure for the full networks. Unless a fracture or rapid movement of sand occur, a general trend of decreased permeability was observed due to fines migration because of gas flow as seen in Figure 6.6.1.

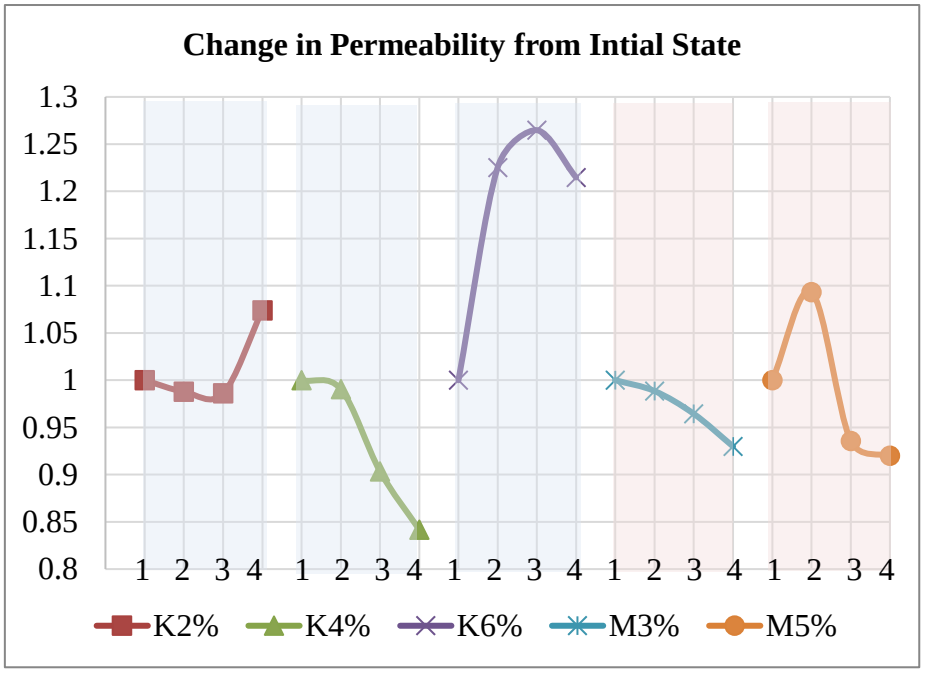

Figure 6.6.1: change in permeability for full pore networks, representing effects of sand dislocations

Primary drainage experiments were simulated using pore networks that are initially filled with water then fully drained. While during water flooding experiments, the real gas fraction of each system was obtained from the images, it was then used to wet the pores randomly, flooding was done by injecting water to the pore networks containing CO_2 gas, the simulation stops when no more gas can be recovered by injecting water, (unrecoverable) gas was quantified.

For primary drainage at kaolinite columns, increasing fines resulted in reduced gas relative permeability krg, but when a fracture form, gas permeability increases; for montmorillonite krg dropped when increasing fines, also as gas was injected the sediment moved in a manner that reduced krg.

In the water flooding, krg increased when increasing fines for all tested columns, while capillary pressure increased when increasing fines content. Most importantly it was shown that in unconsolidated media when more gas is injected in a system it reduces the recoverability by moving the sand grains. This was manifested in a drop in krg when using the pore networks for stage 1 to 4 resulted from the imaged real systems. These trends are compatible with the work done on different experiments simulator showing the same general trends but for theoretical cases (Boujelben, 2017; Boujelben et al., 2018)

Ganglia analysis: it is noted that during gas flow in unconsolidated media, the gas follows the path of the least capillary resistance (capillary fingering). When fines content is increased, the gas ability to percolate smaller throats decreases, this results in local gas pressure increase. Consequently when the pressure increases, the size of the paths that the gas penetrated increases, this dislocates the sand grains. The process results in bigger throats and pores inside the few gas flow paths, but also results in decreased perviousness for the reminder of the system, as size of the rest of pores and throats radii decreases by the dislocated sand. When further increasing the fines content this effect continues resulting in one large path (a fracture body) and there was no gas percolation for the reminder of the system. it is noted that when rapid movements and fracturing occurred, highest fines content were added to the systems. A difference between kaolinite and montmorillonite is observed, in kaolinite 6% a main fracture body represents the main flow path as it has low capillary pressure; while in 5%

montmorillonite, it is noted that gas ganglia disconnect and tend to form big divided ganglia rather than one connected body. This effect may be related to kaolinite being hydrophobic attaching to sand, whereas montmorillonite is hydrophilic attaching to the interface of gas and brine hence inducing snap off.

6.7. Conclusions

1- Synchrotron X-Ray micro-computed tomography, is an effective tool in uncovering the effects of fines migration in multi-phase flow. Workflows were developed to quickly (under one day) transform a raw data to segmented (binarized) image, and calculate a wide range of predictive flow properties, including but not limited to porosity and volume fraction, pore networks, single and multi-phase flow.

2- Pore Networks and Computer-Based Two-Phase Flow Simulations can effectively be used to characterize flow in porous media. For flow in unconsolidated media the pore space geometry will change due to sand grains movements (Jarrar et al., 2018; Jarrar et al., 2019), Pore Networks simplify fluid simulation in a changing void space, easing the effort to characterize the flow.

3- At high concentrations, different fine types produce altered gas flow regimes. Kaolinite resulted in fractures, while montmorillonite resulted in detached gas ganglia.

4- Two-phase flow experiments from pore networks, showed trends that can be used in predicting fines impact on gas flow in sand, increasing fines reduces gas percolation and further injection of gas reduced permeability.

Resources

Adler, P. M., Thovert, J.-F., Bekri, S., & Yousefian, F. (2002). Real Porous Media: Local Geometry and Transports. *Journal of Engineering Mechanics*, *128*(8), 829–839. https://doi.org/10.1061/(ASCE)0733-9399(2002)128:8(829)

Al-Kharusi, A., Engineering, M. B.-J. of P. S. and, & 2007, undefined. (n.d.). Network extraction from sandstone and carbonate pore space images. *Elsevier*. Retrieved from https://www.sciencedirect.com/science/article/pii/S092041050600204X

Al-Raoush, R. I., & Willson, C. S. (2005). A pore-scale investigation of a multiphase porous media system. *Journal of Contaminant Hydrology*, *77*(1–2), 67–89. https://doi.org/10.1016/J.JCONHYD.2004.12.001

Al-Raoush, R. I., & Willson, C. S. (2005). Extraction of physically realistic pore network properties from three-dimensional synchrotron X-ray microtomography images of unconsolidated porous media systems. *Journal of Hydrology*, *300*(1–4), 44–64. https://doi.org/10.1016/j.jhydrol.2004.05.005

Alshibli, K., Cil, M., Kenesei, P., & Lienert, U. (2016). Combined high-energy synchrotron X-Ray diffraction and computed tomography to characterize fracture behavior of sand. In *Frontiers in Particle Science and Technology 2016: Mitigation and Application of Particle Attrition*. Retrieved from https://www.sciencedirect.com/science/article/pii/S0168583X13009270

Ambrose, J. (1973). Computerized transverse axial scanning (tomography): Part 2. Clinical application*. *The British Journal of Radiology*, *46*(552), 1023–1047. https://doi.org/10.1259/0007-1285-46-552-1023

Andrew, M., Bijeljic, B., & Blunt, M. J. (2014). Pore-scale contact angle measurements at reservoir conditions using X-ray microtomography. *Advances in Water*

Resources, 68, 24-31. Retrieved from https://www.sciencedirect.com/science/article/pii/S0309170814000372

Bakke, S., & Øren, P.-E. (1997). 3-D Pore-Scale Modelling of Sandstones and Flow Simulations in the Pore Networks. *SPE Journal*, *2*(02), 136–149. https://doi.org/10.2118/35479-pa

Bakke, S., & ØRen, P.-E. (2002). Process Based Reconstruction of Sandstones and Prediction of Transport Properties. *Transport in Porous Media*, *46*(2–3), 311–343. https://doi.org/10.1023/a:1015031122338

Bennion, D. B., & Thomas, F. B. (1994). Underbalanced Drilling of Horizontal Wells: Does It Really Eliminate Formation Damage? In *SPE Formation Damage Control Symposium*. Society of Petroleum Engineers. https://doi.org/10.2118/27352-MS

Bennion, D. B., Thomas, F. B., Bietz, R. F., & Bennion, D. W. (1999). Remediation of Water And Hydrocarbon Phase Trapping Problems In Low Permeability Gas Reservoirs. *Journal of Canadian Petroleum Technology*, *38*(08). https://doi.org/10.2118/99-08-01

Bernard, D., Guillon, O., Combaret, N., & Plougonven, E. (2011). Constrained sintering of glass films: Microstructure evolution assessed through synchrotron computed microtomography. *Acta Materialia*, *59*(16), 6228–6238. https://doi.org/10.1016/j.actamat.2011.06.022

Bernstein, R. (1987). Adaptive nonlinear filters for simultaneous removal of different kinds of noise in images. *IEEE Transactions on Circuits and Systems*, *34*(11), 1275–1291. https://doi.org/10.1109/TCS.1987.1086066

Bigno, Y., Oyeneyin, M. B., & Peden, J. M. (1994). Investigation of Pore-Blocking Mechanism in Gravel Packs in the Management and Control of Fines Migration. In *SPE Formation Damage Control Symposium*. Society of Petroleum Engineers.

https://doi.org/10.2118/27342-MS

Blewett, J. P. (1998). Synchrotron Radiation – Early History. *Journal of Synchrotron Radiation*, *5*(3), 135–139. https://doi.org/10.1107/S0909049597043306

Bloomfield, J. P., & Williams, A. T. (1995). An empirical liquid permeability—gas permeability correlation for use in aquifer properties studies. *Quarterly Journal of Engineering Geology and Hydrogeology*, 28(Supplement 2), S143-S150. Retrieved from http://qjegh.lyellcollection.org/content/28/Supplement_2/S143.short

Boswell, R., Collett, T. S., Frye, M., Shedd, W., McConnell, D. R., & Shelander, D. (2012). Subsurface gas hydrates in the northern Gulf of Mexico. *Marine and Petroleum Geology*, *34*(1),4–30.https://doi.org/10.1016/j.marpetgeo.2011.10.003

Boujelben, A. (2017). A new pore-scale numerical simulator for investigating special core analysis data. Retrieved from http://www.ros.hw.ac.uk/handle/10399/3283

Boujelben, A., McDougall, S., Watson, M., Bondino, I., & Agenet, N. (2018). Pore network modelling of low salinity water injection under unsteady-state flow conditions. *Journal of Petroleum Science and Engineering*. https://doi.org/10.1016/j.petrol.2018.02.040

Brownrigg, D. R. K. (2002). The weighted median filter. *Communications of the ACM*, *27*(8), 807–818. https://doi.org/10.1145/358198.358222

Brunke, O., Brockdorf, K., Drews, S., Müller, B., Donath, T., Herzen, J., & Beckmann, F. (2008, September). Comparison between x-ray tube-based and synchrotron radiation-based μCT. *In Developments in X-ray tomography* VI (Vol. 7078, p. 70780U). International Society for Optics and Photonics. Retrieved from http://proceedings.spiedigitallibrary.org/proceeding.aspx?doi=10.1117/12.794789

Bryant, S., & Blunt, M. (1992). Prediction of relative permeability in simple porous media. *Physical Review A*, *46*(4), 2004–2011. https://doi.org/10.1103/PhysRevA.46.2004

Bryant, S. L., King, P. R., & Mellor, D. W. (1993). Network model evaluation of permeability and spatial correlation in a real random sphere packing. *Transport in Porous Media*, 11(1), 53-70. Retrieved from http://link.springer.com/10.1007/BF00614635

Bryant, S. L., Mellor, D. W., & Cade, C. A. (1993a). Physically representative network models of transport in porous media. *AIChE Journal*, *39*(3), 387–396. https://doi.org/10.1002/aic.690390303

Bryant, S. L., Mellor, D. W., & Cade, C. A. (1993b). Physically representative network models of transport in porous media. *AIChE Journal*, *39*(3), 387–396. https://doi.org/10.1002/aic.690390303

Buades, A., Coll, B., & Morel, J. M. (2005, June). A non-local algorithm for image denoising. In 2005 IEEE Computer Society Conference on Computer Vision and Pattern Recognition (CVPR'05) (Vol. 2, pp. 60-65). IEEE. Retrieved from https://ieeexplore.ieee.org/abstract/document/1467423/

Cao, S. C., Dai, S., & Jung, J. (2016). Supercritical CO2and brine displacement in geological carbon sequestration: Micromodel and pore network simulation studies. *International Journal of Greenhouse Gas Control*, *44*(December 2017), 104–114. https://doi.org/10.1016/j.ijggc.2015.11.026

Cook, A. E., & Malinverno, A. (2013). Short migration of methane into a gas hydrate-bearing sand layer at Walker Ridge, Gulf of Mexico. *Geochemistry, Geophysics, Geosystems*, *14*(2), 283–291. https://doi.org/10.1002/ggge.20040

Dai, J., Xu, H., Snyder, F., & Dutta, N. (2004). Detection and estimation of gas hydrates

using rock physics and seismic inversion: Examples from the northern deepwater Gulf of Mexico. *The Leading Edge*, *23*(1), 60–66. https://doi.org/10.1190/1.1645456

Oldendorf, W. H. (1961). Isolated flying spot detection of radiodensity dis-continuities-displaying the internal structural pattern of a complex object. IRE transactions on bio-medical electronics, 8(1), 68-72. Retrieved from https://ieeexplore.ieee.org/abstract/document/4322854/

Fatt, I. (1956). The Network Model of Porous Media. *Petroleum Transactions*, *207*, 144–181. Retrieved from https://www.onepetro.org/general/SPE-574-G

Fernandez-Carreiras, D., Buslaps, T., Svensson, O., Honkimäki, V., Merino, J. M., Martins, T., … Falus, P. (2005). Fast microtomography using high energy synchrotron radiation. *Review of Scientific Instruments*, *76*(4), 043702. https://doi.org/10.1063/1.1884194

G.N, H. (1973). Computerized transverse axial scanning(tomography):Part I description of system. *British Journal of Radiology*, *46*(552), 1016–1022. https://doi.org/10.1259/0007-1285-46-552-1016

Goldstein, J., Newbury, D., Michael, J., & Ritchie, N. (2017). *Scanning electron microscopy and X-ray microanalysis*. Retrieved from https://books.google.com/books?hl=en&lr=&id=D0I_DwAAQBAJ&oi=fnd&pg=PR5&dq=x-ray+emission+techniques+%22SEM%22&ots=35PF9qCmqi&sig=u57_g5MrLf_-mPFScCjiHZy1SmE

Gruesbeck, C., & Collins, R. E. (1982). Entrainment and Deposition of Fine Particles in Porous Media. *Society of Petroleum Engineers Journal*, *22*(06), 847–856. https://doi.org/10.2118/8430-PA

Han, G., Kwon, T.-H., Lee, J. Y., & Kneafsey, T. J. (2018). Depressurization-Induced Fines Migration in Sediments Containing Methane Hydrate: X-Ray Computed Tomography Imaging Experiments. *Journal of Geophysical Research: Solid Earth*, *123*(4), 2539–2558. https://doi.org/10.1002/2017JB014988

Han, G., Kwon, T. (2018). Depressurization-induced fines migration in sediments containing methane hydrate: X-ray computed tomography imaging experiments. *Wiley Online Library*. Retrieved from https://agupubs.onlinelibrary.wiley.com/doi/abs/10.1002/2017JB014988

Hilfer, R. (1991). Geometric and dielectric characterization of porous media. *Physical Review B*, *44*(1), 60–75. https://doi.org/10.1103/PhysRevB.44.60

Hyodo, M., Li, Y., Yoneda, J., Nakata, Y., Yoshimoto, N., & Nishimura, A. (2014). Effects of dissociation on the shear strength and deformation behavior of methane hydrate-bearing sediments. *Marine and Petroleum Geology*. https://doi.org/10.1016/j.marpetgeo.2013.11.015

Iglauer, S., Paluszny, A., & Blunt, M. J. (2013). Erratum: Simultaneous oil recovery and residual gas storage: A pore-level analysis using in situ X-ray micro-tomography (Fuel (2013) (905-914)). *Fuel*. https://doi.org/10.1016/j.fuel.2014.09.031

Imdakm, A. O., & Sahimi, M. (1991). Computer simulation of particle transport processes in flow through porous media. *Chemical Engineering Science*, *46*(8), 1977–1993. https://doi.org/10.1016/0009-2509(91)80158-U

Jarrar, Z. A., Al-Raoush, R. I., Hannun, J. A., Alshibli, K. A., & Jung, J. (2018). 3D synchrotron computed tomography study on the influence of fines on gas driven fractures in Sandy Sediments. *Geomechanics for Energy and the Environment*, (xxxx), 1–10. https://doi.org/10.1016/j.gete.2018.11.001

Jarrar, Z. A., Alshibli, K. A., Al-Raoush, R. I., & Jung, J. (2019a). Gas driven fracture during gas production using 3D synchrotron computed tomography. In *Springer Series in Geomechanics and Geoengineering*. https://doi.org/10.1007/978-3-319-99670-7_43

Jarrar, Z. A., Alshibli, K. A., Al-Raoush, R. I., & Jung, J. (2019b). Gas Driven Fracture During Gas Production Using 3D Synchrotron Computed Tomography (pp. 344–351). Springer, Cham. https://doi.org/10.1007/978-3-319-99670-7_43

Jerauld, G. R., Hatfield, J. C., Scriven, L. E., & Davis, H. T. (1984). Percolation and conduction on Voronoi and triangular networks: a case study in topological disorder. *Journal of Physics C: Solid State Physics*, *17*(9), 1519–1529. https://doi.org/10.1088/0022-3719/17/9/010

Jerauld, G. R., Scriven, L. E., & Davis, H. T. (1984). Percolation and conduction on the 3D Voronoi and regular networks: a second case study in topological disorder. *Journal of Physics C: Solid State Physics*, *17*(19), 3429–3439. https://doi.org/10.1088/0022-3719/17/19/017

Jung, J., Cao, S. C., Shin, Y.-H., Al-Raoush, R. I., Alshibli, K., & Choi, J.-W. (2018a). A microfluidic pore model to study the migration of fine particles in single-phase and multi-phase flows in porous media. *Microsystem Technologies*, *24*(2), 1071–1080. https://doi.org/10.1007/s00542-017-3462-1

Jung, J., Cao, S. C., Shin, Y.-H., Al-Raoush, R. I., Alshibli, K., & Choi, J.-W. (2018b). A microfluidic pore model to study the migration of fine particles in single-phase and multi-phase flows in porous media. *Microsystem Technologies*, *24*(2), 1071–1080. https://doi.org/10.1007/s00542-017-3462-1

Jung, J. W., Jang, J., Santamarina, J. C., Tsouris, C., Phelps, T. J., & Rawn, C. J. (2012). Gas Production from Hydrate-Bearing Sediments: The Role of Fine Particles.

Energy & Fuels, *26*(1), 480–487. https://doi.org/10.1021/ef101651b

Khan, H. J. (2016). *Improved permeability estimation of formation damage through imaged core flooding experiments*. University of Texas at Austin. Retrieved from https://repositories.lib.utexas.edu/handle/2152/47001

Khan, H. J., Mirabolghasemi, M. S., Yang, H., Dicarlo, D. A., & Balhoff, M. T. (2017). Journal of Petroleum Science and Engineering Study of formation damage caused by retention of bi-dispersed particles using combined pore-scale simulations and particle flooding experiments, *158*(February), 293–308. https://doi.org/10.1016/j.petrol.2017.08.061

Khan, H. J., Mirabolghasemi, M. S., Yang, H., Sa Prodanovi, M., Dicarlo, D. A., & Balhoff, M. T. (2017). Study of formation damage caused by retention of bi-dispersed particles using combined pore-scale simulations and particle flooding experiments. *Journal of Petroleum Science and Engineering*, *158*, 293–308. https://doi.org/10.1016/j.petrol.2017.08.061

Khilar, K. C., & Fogler, H. S. (1987). Colloidally Induced Fines Migration in Porous Media. *Reviews in Chemical Engineering*, *4*(1–2), 41–108. https://doi.org/10.1515/REVCE.1987.4.1-2.41

Khilar, K. C., & Fogler, H. S. (1998). *Migrations of Fines in Porous Media* (Vol. 12). Springer Science & Business Media. https://doi.org/10.1007/978-94-015-9074-7

Krane, K., & Halliday, D. (1987). *Introductory nuclear physics*. Retrieved from http://dspace.fue.edu.eg/xmlui/bitstream/handle/123456789/2949/11345.pdf?sequence=1

Kundu, A., Mitra, S., & Vaidyanathan, P. (2004). Application of two-dimensional generalized mean filtering for removal of impulse noises from images. *IEEE Transactions on Acoustics, Speech, and Signal Processing*, *32*(3), 600–609.

https://doi.org/10.1109/tassp.1984.1164364

Malik, J., & Perona, P. (1990). Scale-space and edge detection using anisotropic diffusion. *IEEE Transactions on Pattern Analysis and Machine Intelligence*, *12*(7), 629–639. https://doi.org/10.1109/34.56205

Malik, P. P. and J. (1987). *Proceedings of IEEE Computer Society Workshop on Computer Vision,*.

Maroudas, A., & Eisenklam, P. (1965a). Clarification of suspensions: a study of particle deposition in granular media: Part I—Some observations on particle deposition. *Chemical Engineering Science*, *20*(10), 867–873. https://doi.org/10.1016/0009-2509(65)80083-5

Maroudas, A., & Eisenklam, P. (1965b). Clarification of suspensions: a study of particle deposition in granular media: Part II—A theory of clarification. *Chemical Engineering Science*, *20*(10), 875–888. https://doi.org/10.1016/0009-2509(65)80084-7

Michael Byrne. (2012). *Formation Damage – Any Time, Any Place, Any Where*. https://doi.org/http://www.afes.org.uk/uploads/files/Formation%20Damage%20%E2%80%93%20Any%20Time.pdf

Mining, C. H.-T. of the A. A. of, & 1939, undefined. (n.d.). Interfacial tension between water and oil under reservoir conditions. *Onepetro.Org*. Retrieved from https://www.onepetro.org/download?id=journal-paper%2FSPE-939184-G

Mrozewski, S. A., Collett, T. S., Cook, A. E., Guerin, G., Zyrianova, M. V., Lee, M. W., & Goldberg, D. S. (2011). Gulf of Mexico Gas Hydrate Joint Industry Project Leg II logging-while-drilling data acquisition and analysis. *Marine and Petroleum Geology*, *34*(1), 41–61. https://doi.org/10.1016/j.marpetgeo.2011.08.003

Muecke, T. W. (1979). Formation Fines and Factors Controlling Their Movement in

Porous Media. *Journal of Petroleum Technology*, *31*(02), 144–150. https://doi.org/10.2118/7007-PA

Oyeneyin, M. B., Peden, J. M., Hosseini, A., & Ren, G. (1995). Factors to Consider in the Effective Management and Control of Fines Migration in High Permeability Sands. In *SPE European Formation Damage Conference*. Society of Petroleum Engineers. https://doi.org/10.2118/30112-MS

Park, J., & Santamarina, J. C. (2017). Revised Soil Classification System for Coarse-Fine Mixtures. *Journal of Geotechnical and Geoenvironmental Engineering*, *143*(8), 04017039. https://doi.org/10.1061/(ASCE)GT.1943-5606.0001705

Perry, B. J., & Bridges, C. (1973). Computerized transverse axial scanning (tomography): Part 3. Radiation dose considerations. *The British Journal of Radiology*, *46*(552), 1048–1051. https://doi.org/10.1259/0007-1285-46-552-1048

Pratt, W. K. (2013). *Introduction to Digital Image Processing*. *Introduction to Digital Image Processing*. CRC Press. https://doi.org/10.1201/b15731

Research, J. B.-N. I. and M. in P., & 1988, undefined. (n.d.). Synchrotron radiation—1873 to 1947. *Elsevier*. Retrieved from https://www.sciencedirect.com/science/article/pii/016890028890349X

Rodriguez-Pin, E. (2010). Grain-scale mechanisms of particle retention in saturated and unsaturated granular materials. Retrieved from https://repositories.lib.utexas.edu/handle/2152/ETD-UT-2010-12-2537

Ruspini, L. C., Farokhpoor, R., & Øren, P. E. (2017). Pore-scale modeling of capillary trapping in water-wet porous media: A new cooperative pore-body filling model. *Advances in Water Resources*, *108*, 1–14. https://doi.org/10.1016/j.advwatres.2017.07.008

Sahimi, M., Gavalas, G. R., & Tsotsis, T. T. (1990). Statistical and continuum models

of fluid-solid reactions in porous media. *Chemical Engineering Science*, *45*(6), 1443–1502. https://doi.org/10.1016/0009-2509(90)80001-U

Sakthivadivel, R. (1966). Theory and mechanism of filtration of non-particleal fines through a porous medium. *Hydraul. Eng. Lab., Univ. of Calif., Berkeley.*, *15*(5), 110.

Saraji, S., Goual, L., Piri, M., & Plancher, H. (2013). Wettability of Supercritical Carbon Dioxide/Water/Quartz Systems: Simultaneous Measurement of Contact Angle and Interfacial Tension at Reservoir Conditions. *Langmuir*, *29*(23), 6856–6866. https://doi.org/10.1021/la3050863

Sokolov, A., (1966). Synchrotron radiation. *Adsabs.Harvard.Edu*. Retrieved from http://adsabs.harvard.edu/abs/1966siiz.book.....S

Span, R., & Wagner, W. (1996). A New Equation of State for Carbon Dioxide Covering the Fluid Region from the Triple-Point Temperature to 1100 K at Pressures up to 800 MPa. *Journal of Physical and Chemical Reference Data*, *25*(6), 1509–1596. https://doi.org/10.1063/1.555991

Stampanoni, M., Borchert, G., Wyss, P., Abela, R., Patterson, B., Hunt, S., … Peter, R. (2002). High resolution X-ray detector for synchrotron-based microtomography. *Elsevier*, *491*, 291–301. Retrieved from https://www.sciencedirect.com/science/article/pii/S0168900202011671

Sun, T., & Neuvo, Y. (1994). Detail-preserving median based filters in image processing. *Pattern Recognition Letters*, *15*(4), 341–347. https://doi.org/10.1016/0167-8655(94)90082-5

Tonner, B. P., & Harp, G. R. (1988). Photoelectron microscopy with synchrotron radiation. *Review of Scientific Instruments*, *59*(6), 853–858. https://doi.org/10.1063/1.1139792

Van Gompel, G., Van Slambrouck, K., Defrise, M., Batenburg, K. J., de Mey, J., Sijbers, J., & Nuyts, J. (2011). Iterative correction of beam hardening artifacts in CT. *Medical Physics*, *38*(S1), S36–S49. https://doi.org/10.1118/1.3577758

WC Röntgen. (1896). On a new kind of rays. *Science*, *3*(56), 227–231. Retrieved from https://www.jstor.org/stable/1623595

Whrele, R. B., & Nielsen, R. W. (1988). Design for APS 7 GeV storage ring vacuum system at ANL. In *AIP Conference Proceedings* (Vol. 171, pp. 60–72). AIP. https://doi.org/10.1063/1.37290

Xiong, Q., Baychev, T. G., & Jivkov, A. P. (2016). Review of pore network modelling of porous media. *Journal of Contaminant Hydrology*, *192*, 101–117. https://doi.org/10.1016/j.jconhyd.2016.07.002 T4 - Experimental characterisations, network constructions and applications to reactive transport M4 - Citavi

Yamamoto, K., Terao, Y., Fujii, (2014). Operational overview of the first offshore production test of methane hydrates in the Eastern Nankai Trough. *Onepetro.Org*. Retrieved from https://www.onepetro.org/conference-paper/OTC-25243-MS

Yu, H., He, Y., Li, P., Li, S., Zhang, T., Rodriguez-Pin, E., Huh, C. (2015). Flow enhancement of water-based nanoparticle dispersion through microscale sedimentary rocks. *Scientific Reports*, *5*(March). https://doi.org/10.1038/srep08702